SIMULTANEOUS AND INSTANTANEOUS MEASUREMENT OF VELOCITY AND DENSITY IN RAYLEIGH-TAYLOR MIXING LAYERS

A Dissertation

by

WAYNE NEAL KRAFT

Submitted to the Office of Graduate Studies of
Texas A&M University
in partial fulfillment of the requirements for the degree of

DOCTOR OF PHILOSOPHY

May 2008

Major Subject: Mechanical Engineering

SIMULTANEOUS AND INSTANTANEOUS MEASUREMENT OF VELOCITY AND DENSITY IN RAYLEIGH-TAYLOR MIXING LAYERS

A Dissertation

by

WAYNE NEAL KRAFT

Submitted to the Office of Graduate Studies of
Texas A&M University
in partial fulfillment of the requirements for the degree of

DOCTOR OF PHILOSOPHY

Approved by:

Chair of Committee,	Malcolm Andrews
Committee Members,	Sharath Girimaji
	Obdulia Ley
	Ed Marotta
Head of Department,	Dennis O'Neal

May 2008

Major Subject: Mechanical Engineering

ABSTRACT

Simultaneous and Instantaneous Measurement of Velocity and Density in

Rayleigh-Taylor Mixing Layers.

(May 2008)

Wayne Neal Kraft, B.S., Texas A&M University;

M.S., Texas A&M University

Chair of Advisory Committee: Professor Malcolm J. Andrews

There are two coupled primary objectives for this study of buoyancy-driven turbulence. The first objective is to create a new diagnostic for collection of measurements to capture the physics of Rayleigh-Taylor (RT) mixing. The second objective is to use the new diagnostic to specifically elucidate the physics of large Atwood number, $A_t = (\rho_1 - \rho_2)/(\rho_1 + \rho_2)$, RT mixing. Both of these objectives have been satisfied through the development of a new hot-wire diagnostic to study buoyancy-driven turbulence in a statistically steady gas channel of helium and air ($0.03 \le A_t \le 0.6$). The capability of the diagnostic to simultaneously and instantaneously measure turbulent velocity and density fluctuations allows for a unique investigation into the dynamics of Rayleigh-Taylor mixing layers at large A_t, through measurements of turbulence and mixing statistics. The new hot-wire diagnostic uses temperature as a fluid marker for helium and air, which is possible due to the Lewis number ~ 1 *(Le* = ratio of thermal diffusivity to mass diffusivity) for helium and air, and the new diagnostic has been validated in an A_t = 0.03 mixing layer. The energy density spectrum of $\rho' v'$, measured experimentally for the first time in RT mixing, is found to closely follow the energy distribution of v', up to the Reynolds numbers

investigated ($\mathrm{Re}_h = (2h)^{3/2}\sqrt{gA_t/6}\,/\,\upsilon_{mix} \sim 1450$). Large A_t experiments, with A_t = 0.6, have also been achieved for the first time in a miscible RT mixing layer. An asymmetric penetration of the bubbles (rising fluid) and spikes (falling fluid) has been observed, resulting in measured self similar growth parameters $\alpha_b = 0.060$ and $\alpha_s = 0.088$ for the bubbles and spikes, respectively. The first experimental measurements of turbulent velocity and density fluctuations for the large A_t case, show a strong similarity to lower A_t behaviors when normalized. However conditional statistics, which separate the bubble (light fluid) and spike (heavy fluid) dynamics, has highlighted differences in $\overline{\rho' v'}$ and v'_{rms} in the bubbles and spikes. Larger values of $\overline{\rho' v'}$ and v'_{rms} were found in the downward falling spikes, which is consistent with the larger growth rates and momentum of the spikes compared to the bubbles. These conditional statistics are a first in RT driven turbulence.

ACKNOWLEDGEMENTS

I would like to thank my research advisor, Professor Malcolm J. Andrews, for his guidance in completing this work and also my committee. I would also like to thank my co-workers (current and past), especially Dr. Arindam Banerjee, Dr. Nader Berchane, Dr. Gopinath Subramaniam, Dr. Nicholas Mueschke, and Michael Peart for their help in performing experiments and completing this work. I also appreciate the help of Dr. Oleg Schilling in reviewing the written dissertation. Finally I would like to thank my friends and family, particularly my parents and wife, Laura, for their support. This research has been funded by the U.S. Department of Energy from DOE Grant # DE-FG03-02NA0060.

NOMENCLATURE

A_t	Atwood number [$\equiv(\rho_1-\rho_2)/(\rho_1+\rho_2)$]
a_0	BHR model parameter for the miscible turbulent mass flux
a_2	Two-fluid (immiscible) equivalent of the BHR model parameter for the turbulent mass flux
α_b, α_s	Rayleigh-Taylor growth parameter for bubble and spike sides of the mixing layer
α_{CL}	Rayleigh-Taylor growth parameter determined using centerline v'
B_0	Density self-correlation for the miscible mixing layer
B_2	Two-fluid (immiscible) equivalent of the density self correlation for a miscible mixing layer
β	Thermal diffusivity (m^2/s)
$c_{p,1}$, $c_{p,2}$, $c_{p,mix}$	Specific heat of inlet streams 1 and 2 and the mixing layer (J/ kg-ºC))
D_α	Empirical exponent for a power law fit Atwood number dependence on the ratio of mixing layer growth parameters
E	Hot-wire anemometer voltage (V)
E_{cw}	Cold-wire anemometer voltage (V)
ε	Extinction coefficient for the absorption of light in a dye medium
$f_{m,1}$, $f_{m,2}$	Mass fraction of streams 1 (top) and 2 (bottom) in the mixing layer
$f_{v,1}$, $f_{v,2}$	Volume fraction of streams 1 and 2 in the mixing layer
$f_{v,he}$	Volume fraction of helium
g	Gravitational acceleration (m/s^2)
h_b, h_s	Mixing layer width on bubble and spike sides of the mixing layer (m)

H	Height of the gas channel (m)
I	Current through the cold-wire anemometer bridge (A)
I_{corr}, I_o, I_m	Image light intensity of the corrected image, light source, and the raw measured light intensity
k	Wavenumber ($2\pi/\lambda$) (m^{-1})
K	Kinetic energy (m^2/s^2)
K_v, K_w	Kurtosis of the vertical and cross-stream velocity fluctuations
κ	Mixing parameter based on the vertical turbulent mass flux
Le	Lewis number (ratio of thermal diffusivity to mass diffusivity)
λ	Wavelength (m)
υ	Kinematic viscosity (m^2/s)
Pr	Prandtl number (ratio of kinematic viscosity to thermal diffusivity)
ρ_1, ρ_2,, ρ_{mix}	Fluid densities of inlet streams 1 and 2 and the mixing layer (kg/m^3)
ρ'	Density fluctuations inside the mixing layer (kg/m^3)
R	Density ratio of fluid 1 and 2 streams (ρ_1/ρ_2)
R_{ref}	Resistance of the cold-wire at the reference temperature (Ohm)
$R_{\rho'v'}$	Correlation coefficient for ρ' and v'
S_v, S_w	Skewness of the vertical and cross-stream velocity fluctuations
Sc	Schmidt number (ratio of kinematic viscosity to mass diffusivity)
τ	Non-dimensional time
θ	Molecular mixing parameter
t	Time (s)

T_{ref}, T_{wire}	Reference temperature for anemometers and the temperature of the hot-wire (°C)
T_1, T_2, T_{mix}	Temperature of inlet streams 1 and 2 and the mixing layer (°C)
U_{eff}	Hot-wire sensor effective (normal) velocity (m/s)
U_m	Mean advective velocity for the channel flow (m/s)
u', v', w'	Stream-wise, vertical, and cross-stream velocity fluctuations (m/s)
$\overline{U}$, $\overline{V}$, $\overline{W}$	Stream-wise, vertical, and cross-stream mean velocities (m/s)
X,Y,Z	Stream-wise, vertical, and cross-stream directions for lab coordinate system

TABLE OF CONTENTS

Page

Page

Page

LIST OF FIGURES

FIGURE Page

FIGURE Page

FIGURE Page

LIST OF TABLES

1. INTRODUCTION

1.1 Motivation

Buoyancy-driven mixing by the Rayleigh-Taylor (RT) instability occurs across broad classes of fluid flows such as effluent discharge into rivers and estuaries, heat exchangers, or sprays in internal combustors (Beale & Reitz 1999). These instabilities occur when a heavy fluid is oriented above a lighter fluid and accelerated by gravity. Rayleigh-Taylor fluid instabilities develop into turbulence by converting the potential energy of the heavy fluid into kinetic energy. The RT driven turbulence mixes the fluids, resulting in a turbulent mixing layer. The motivation for the current research is to provide insight into the development of turbulent mixing that occurs in inertial confinement fusion (ICF). Thermonuclear fusion is a naturally occurring process in young supernova (Gull 1975) and ICF is being developed as a method for artificially producing thermonuclear fusion. During ICF, a spherical capsule filled with light deuterium and tritium gas is accelerated or imploded (Betti *et al.* 2001). Hydrodynamic instabilities play an important role in the implosion phase of ICF, as buoyancy-driven mixing of the shell and fuel limits the energy yield of the overall process (Lindl 1998). A fundamental understanding of buoyancy-driven mixing and the Rayleigh-Taylor instability is therefore necessary to develop ICF applications.

In particular, an experimental description of buoyancy-driven turbulence is necessary to validate numerical simulations and turbulence models. This need was first highlighted by

---

This dissertation follows the style of *Journal of Fluid Mechanics*.

Sharp (1984) in his review of Rayleigh-Taylor instabilities over twenty years ago. Sharp describes the necessity to validate numerical simulations and develop late-time turbulence models by measuring the time histories of a developing turbulent interface of Rayleigh-Taylor instabilities, preferably through a statistical description. The chaotic and random nature of turbulence requires a statistical description of the developing fluid instabilities. Experimental facilities and measurements of buoyancy-driven turbulence are challenging, due to the transient nature of the experiments, complexity of the turbulent fluid flow, and the high-fidelity diagnostics needed to measure both velocity and density fluctuations simultaneously. As a result, the challenge set by Sharp in 1984 to researchers is still pertinent today.

The challenges addressed in this work are experimentally based, statistical measurements of miscible RT driven fluid turbulence and molecular mixing up to large Atwood numbers (large density differences) through simultaneous and instantaneous measurements of velocity and density fluctuations. The new diagnostic, developed as integral part of this study, has the unique capability to obtain measurements of $\overline{u'^2}$, $\overline{v'^2}$, $\overline{w'^2}$, $\overline{\rho'^2}$, $\overline{\rho' v'}$, their *p.d.f.*'s, and energy density spectra at Atwood numbers of 0.03 and 0.6, in a gas mixture with large density gradients. Of particular interest are instantaneous measurements of the vertical turbulent mass flux, $\overline{\rho' v'}$, for its role in transport and kinetic energy production in buoyancy-driven turbulence. These are the first instantaneous measurements of the turbulent mass flux obtained from experiments in a Rayleigh-Taylor mixing layer. In addition, experimental measurements of the fluid turbulence at $A_t = 0.6$ are the first of their kind at large A_t, and the largest A_t ever achieved for miscible RT mixing. Furthermore, the unique capabilities (simultaneous and instantaneous measurement of velocity and density fluctuations) of the new hot-wire diagnostic has led to the first conditional measurements of the bubble and spike dynamics. These measurements provide a

foundation for validation of turbulence simulations and modeling, in addition to providing insight into the dynamics of the turbulent mixing layer up to large Atwood numbers.

1.2 Buoyancy-driven turbulence

Buoyancy-driven turbulence resulting from Rayleigh-Taylor (RT) instabilities occurs in an unstably stratified flow when a heavy fluid rests above a light fluid, and when a pressure gradient (imposed by a gravitational field) opposes a density gradient along the interface of two fluids, such that $\nabla p \bullet \nabla \rho < 0$ (Chandrasekhar 1961). Small perturbations at the interface between the two fluids grow, developing into a turbulent mixing layer. The buoyancy-driven growth of perturbations proceed through growth regimes of linear instability (exponential growth), nonlinear instability, and finally form a self similar RT mixing layer (Youngs 1984). A computational illustration of developing Rayleigh-Taylor instabilities as it progresses through this growth is shown in Figure 1.1 using a collocated, two-dimensional, finite-volume code. The finger-like growth of initial interfacial perturbations is characteristic of Rayleigh-Taylor instabilities. In addition, the mushroom shaped plumes are prevalent in this type of flow.

The primary governing parameter of this buoyancy-driven instability is the Atwood number,

$$A_t = (\rho_1 - \rho_2)/(\rho_1 + \rho_2), \tag{1.1}$$

where ρ_1 and ρ_2 are the heavy and light fluid densities, respectively. When there is no density difference, $A_t = 0$, and when there is an infinite density difference, $A_t = 1$. At late-time, the self-similar turbulent mixing layer demonstrates a quadratic growth of the mixing layer half width, h. This is demonstrated by the dimensional analysis of Youngs (1984), where h is a function of the

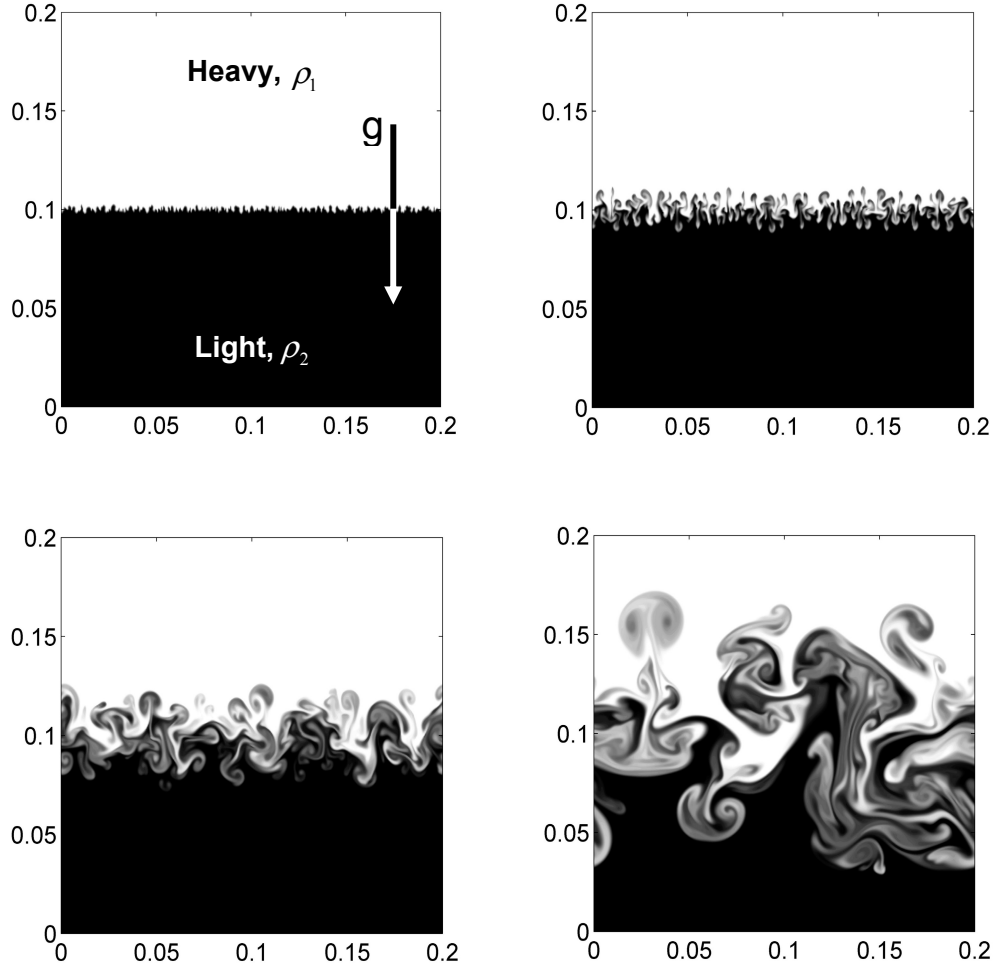

Figure 1.1. Illustration of multi-mode Rayleigh-Taylor instability growth at non-dimensional times of $\tau = t\sqrt{A_t g / H}$ = 0.32, 0.74, 1.5 and 3.1, where A_t is the Atwood number, t is time, g is gravity, and H is the height of the domain. This illustration is from a computational simulation of Rayleigh-Taylor instability at an A_t = 0.09 in a 20 cm x 20 cm domain with 384^2 grid cells. The simulation was performed using a collocated, two-dimensional, finite-volume code.

Atwood number (A_t), the gravitational acceleration (g), time (t), and the growth parameter α (with a measured range of 0.044 to 0.07),

$$h = \alpha A_t g t^2 . \tag{1.2}$$

Early work by Youngs (1984) suggested the growth parameter should be universal, and independent of initial conditions. Indeed, it was thought the quadratic growth of (1.2) could only be achieved once memory of the initial conditions was lost. The late-time growth would therefore be driven by the non-linear interactions of competing structures (mode-coupling) and not the initial disturbances. Although numerical simulations initially yielded consistent growth parameters of α = 0.04 (Youngs 1984) supporting this assertion, experimentally measured growth parameters were almost twice as large, with α = 0.07 (Read 1984; Snider & Andrews 1994). This inconsistency was not understood until recent investigations about the role of initial conditions on the development of the mixing layer growth were described (Ramaprabhu *et al*. 2004, Dimonte *et al.* 2004, Mueschke *et al*. 2006). It was found that the inclusion of long wavelength, large amplitude, perturbations in initial disturbances also resulted in a late-time quadratic growth with correspondingly larger growth parameters. This explained the observed larger growth parameters found in experiments (experimental initial conditions generally contain large wavelengths), and the contrasting smaller growth parameters found in simulations (where typically only small wavelengths were included in the initial disturbances to reduce computational expense). As a result, the growth parameter, α, is now believed to have some initial condition dependency (Ramaprabhu *et al*. 2004, Dimonte *et al.* 2004, Mueschke *et al*. 2006).

Quadratic growth of the RT driven mixing layer, described by (1.2), can be seen visually in the low Atwood number experiments using the water channel facility, shown in Figure 1.2. In the water channel, cold water is advected downstream parallel and above hot water, creating a

(a)

(b)

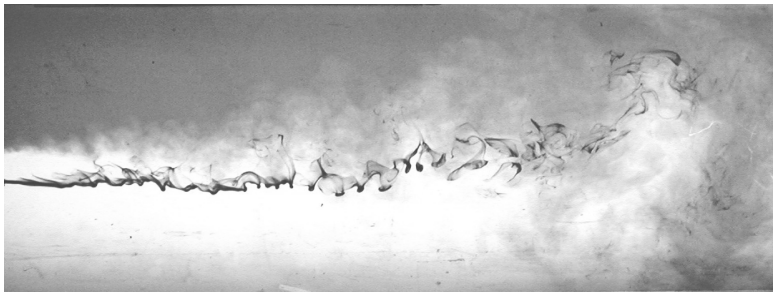

(c)

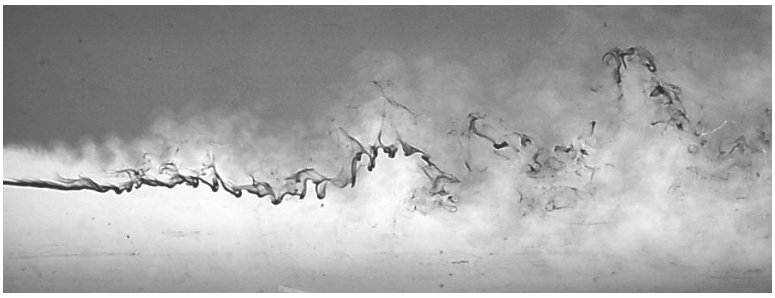

Figure 1.2. Buoyancy-driven mixing layer for A_t = 6.6 x 10^{-4} using hot and cold water to obtain an unstable density stratification. Flow is from left to right at 4 cm/s. (a) Bottom (light) fluid marked with Nigrosene dye. (b-c) Top (heavy fluid) marked with Nigrosene dye with entrainment of fluid into the mixing layer demonstrated using dye streaks (Kraft *et al.* 2005).

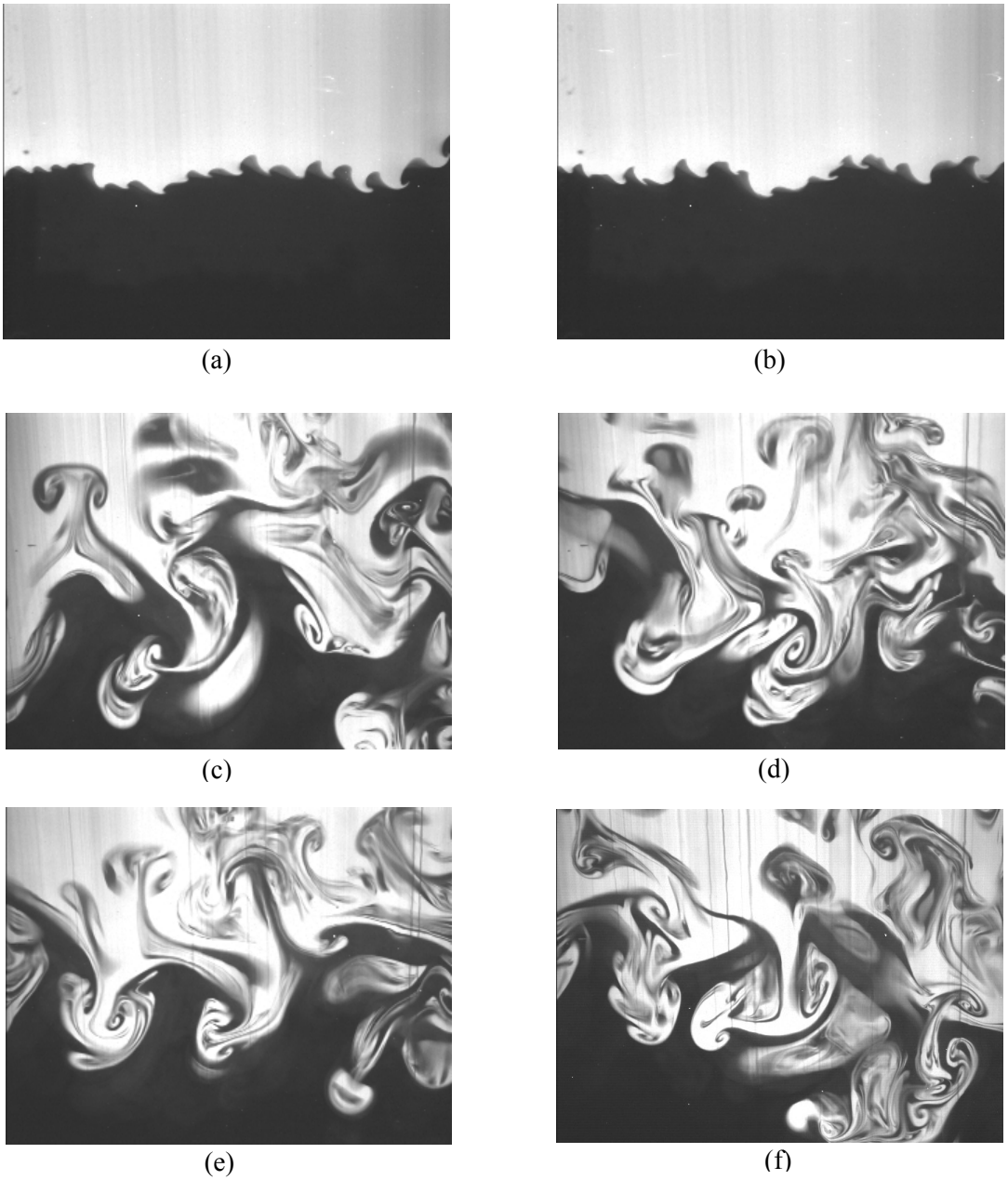

Figure 1.3. (a)-(b) PLIF images directly downstream of the splitter plate in the water channel facility, demonstrating the two-dimensional channel initial conditions. Flow from left to right. (c)-(f) PLIF images 35 cm downstream of the splitter plate illustrating the three-dimensional turbulent structure of the buoyancy-driven mixing layer at late-time (Kraft *et al.* 2005).

mixing layer evolving with downstream distance. Nigrosene dye marks the lighter fluid (bottom stream), and turbulent mixing can be visualized as light and dark fluid as seen in Figure 1.2 (a). Growth of the mixing layer is driven by the rising and falling plumes of hot and cold water (light and heavy fluid). As the plumes fall or rise, fluid mixes from shearing of neighboring structures. As the mixing layer width (bottom to top) grows, exterior fluid from the inlet streams is continually entrained into the mixing layer, providing a continuous source of both fluid and potential energy. This entrainment of the hot and cold water streams can be seen in Figure 1.2 (b)-(c), where dye streaks at the same velocity as the free stream fluid have been injected outside the mixing layer in the hot water stream (bottom) and are advected downstream. Interaction of the mixing layer with the dye streak occurs approximately halfway across the images when the dye streak begins to spread. As the dye streak (hot fluid) is entrained into the mixing layer, it is quickly transported to the top half of the mixing layer and along the way is turbulently mixed with the surrounding fluid. Interestingly, the dye streak appears to rise quadratically, similar to the overall growth of the mixing layer (Snider & Andrews 1994). From the images, significant stretching and deformation of the interface between the two fluids can also be observed. Further inspection of the photograph reveals that unstable density gradients cause initially small perturbations on the interface to grow, stretching and elongating the interface between the two fluids as they mix. Additional detail of the developing structure in fluid turbulence due to Rayleigh-Taylor instabilities can be observed using planar laser-induced fluorescence (PLIF). PLIF allows a two-dimensional view of the flow while also capturing significant detail of the structure. PLIF images of the buoyancy-driven mixing layer in the water channel facility are shown in Figure 1.3. The physical image size is 10.5 cm x 8 cm. Images in Figure 1.3 (a)-(b) are captured as the flow leaves the splitter plate that initially separates the two inlet streams. The initial perturbation leaving the splitter plate is two dimensional and is small in amplitude

(Mueschke *et al.* 2006). Leaning of the small finger-like structures is a result of the boundary layer that forms on the splitter plate causing a small wake. The wake is quickly overcome by the buoyancy-driven mixing (Ramaprabhu & Andrews 2004). Figure 1.3 (c)-(f) show PLIF images of the developed mixing layer approximately 35 cm downstream of the splitter plate. The complexity of the turbulent mixing layer is striking when compared with the initial perturbations of Figure 1.3 (a)-(b). The one-time two-dimensional structure has become three-dimensional as illustrated by the plumes moving in and out of the plane in Figures 1.3 (c) and 1.3 (e). All the images of Figure 1.3 (c)-(f) show a tight roll-up of fluid into vortex pairs, as evident in plumes of both hot (black) and cold (white) fluids. Also, non-linear interaction of neighboring plumes can be seen, in particular in Figures 1.3 (e) and 1.3 (f), as structures appear to combine and become more complex. A more complete visual description of Rayleigh-Taylor mixing layers using experimental facilities at Texas A&M is found in Kraft *et al.* (2005).

At small Atwood number ($A_t \leq 0.1$) the growth of the mixing layer is symmetric relative to the centerline of the mixing layer, as observed in Figure 1.2 (a). Therefore, the growth parameter, α, found using either the top or bottom of the mixing layer would yield the same value. However, at larger Atwood numbers ($A_t \geq 0.1$) non-Boussinesq asymmetries develop within the mixing layer, resulting in a faster growth of the falling spikes when compared with the rising bubbles (Dimonte & Schneider 2000; Banerjee, Kraft & Andrews 2008). As A_t is increased, the spikes in the mixing layer fall at a faster rate, narrowing in contrast to the round, larger diameter rising bubbles. This behavior is a result of mass conservation and the lower resistance of the lighter fluid. Therefore, when considering large Atwood number RT mixing layers it is necessary to describe the mixing layer growth described in (1.2) as

$$h_{b,s} = \alpha_{b,s} A_t g t^2 \qquad (b = bubble, s = spike) \tag{1.3}$$

where a separate growth parameter is defined for the bubble (rising) , α_b, and spike (falling), α_s, sides of the mixing layer. Large Atwood number experiments with multi-mode (containing many wavelengths) initial disturbances and immiscible fluids were performed by Read (1984), Jacobs *et al.* (1988), and Youngs (1989). The diagnostics of these large A_t experiments utilized image analysis, demonstrating the faster growth of h_s when compared to h_b. It was shown that as the density difference between the two fluids increased, so did the mixing layer asymmetry as indicated by the ratio h_s/h_b . More recently, the mixing layer asymmetry has been described by Dimonte and Schneider (2000) for an extensive range $0.13 \leq A_t \leq 0.96$ of immiscible fluids through the measured growth parameters, $\alpha_{b,s}$. In their immiscible experiments, Dimonte and Schneider found that α_b remained approximately constant for $A_t < 0.5$, where $\alpha_b = 0.053$. However at large A_t, α_b exhibited a slight decrease to $\alpha_b = 0.049$. In contrast, α_s increases slowly with A_t, where at $A_t \sim 0.5$, $\alpha_s/\alpha_b = 1.2$. Thereafter, the mixing layer asymmetry significantly increased at $A_t > 0.8$, where the ratio of the spike to bubble growth parameter was greater than 2. Dimonte and Schneider showed that this behavior could be described through an empirical fit,

$$\alpha_s/\alpha_b = R^{D_\alpha}, \tag{1.4}$$

where $R = \rho_1/\rho_2$ and $D_\alpha = 0.33$ is an experimentally determined exponent. However, there was no theoretical justification for this relationship given by Dimonte and Schneider. Interestingly, the previous research at large A_t did not use miscible fluids, perhaps because diffusion at the interface (mixing of the two fluids prior to the start of the experiment) caused sufficient delay for the development of the mixing layers that little could be observed in these time-dependent experiments. In addition, it is believed that surface tension between the immiscible fluids in previous experiments played a significant role in the mixing layer growth.

1.3 Previous experiments investigating Rayleigh-Taylor turbulence

A major difficulty when studying RT mixing processes experimentally is to create and control the initial interface between the two fluids in the presence of an unstable density gradient. As a result, many creative approaches have been used to study buoyancy-driven turbulence and the Rayleigh-Taylor instability. The experiments of Read (1984) utilized a tank containing light and heavy fluids that were stably stratified and initially at rest ($0.23 \leq A_t \leq 0.997$). The tank was then accelerated downward using rocket motors at accelerations up to 50 times greater than gravity, resulting in an unstable density interface. A similar method of examining the Rayleigh-Taylor instability was performed by Dimonte and Schneider (1996), where, instead of rocket motors, a linear electric motor (LEM) was used to accelerate the tank downward ($0.13 \leq A_t \leq 0.96$) at up to 200 times gravity. Measurements by both Read (1984) and Dimonte and Schneider (1996) demonstrated a quadratic growth of the mixing layer width, h_b. In addition, as already described, Dimonte and Schneider provided a description of the effect of Atwood number on the growth parameters, α_b and α_s. Another approach was adopted by Andrews and Spalding (1990), who inverted a narrow tank of initially stably stratified fluids to study the Rayleigh-Taylor instability ($A_t = 0.048$). Andrews and Spalding used a dye marker to obtain quantitative measurements of the density profiles of two-dimensional Rayleigh-Taylor instabilities and the growth rates of the mixing layers. Although these experiments have provided valuable measurements and an understanding of Rayleigh-Taylor instabilities, there is a need driven by validation of turbulent mixing models for additional statistical measurements of the fluid turbulence and mixing phenomena. Specifically, there is a need for statistical measurements of the velocity and density fluctuations inside the Rayleigh-Taylor mixing layer, as well as their corresponding energy density spectra.

As an alternative to the experiments described above, a facility at Texas A&M was developed in 1993 using a water channel to study buoyancy-driven turbulence ($A_t \sim 0.001$). The water channel facility has been used extensively to study turbulent RT mixing layers and the RT instability (Snider & Andrews 1994; Wilson & Andrews 2002; Ramaprabhu & Andrews 2004; Mueschke *et al.* 2006; Kraft & Andrews 2006). Unlike the tank experiments already described, this facility has an advective downstream velocity, U_m. Thus, a downstream location, x, is related to time of evolution through Taylor's Hypothesis, $t = x / U_m$. The main advantages of such an experimental configuration are long data collection times and the statistically steady nature of the experiment that, for the first time, made statistical measurements for RT driven mixing possible.

Initial development of this facility was performed by Snider and Andrews (1994). Using a fluid dye marker and imaging techniques, Snider and Andrews observed the development of the turbulent mixing layer from a statistical viewpoint. This allowed accurate measurements of the mixing layer growth parameter, $\alpha_b = 0.07$, and a demonstration of the onset of self-similarity as determined by the collapse of the mean density profiles across the mixing layer at $\mathrm{Re}_h = (2h)^{3/2}\sqrt{gA_t/6}\,/\,\upsilon_{mix} \sim 1200$. This definition of Re_h was introduced by Snider and Andrews through a balance of kinetic and potential energy across the mixing layer width. An additional benefit was the use of hot/cold water since it made diagnostics such as thermocouples, and particle image velocimetry (PIV), feasible for measuring turbulence statistics over long time periods (Wilson & Andrews 2002; Ramaprabhu & Andrews 2004). In particular, Wilson and Andrews (2002) experimentally measured the spectral behavior of density fluctuations inside the turbulent mixing layer for the first time. Wilson and Andrews found a greater amount of molecular mixing compared with the two-fluid assumption, which is apparent when comparing *p.d.f.*'s of the measured density fluctuations. In addition, they found the development of an

inertial and diffusive subrange within the density power spectrum for buoyancy-driven turbulence.

Additional measurements of velocity and density fluctuations in the Texas A&M water channel were obtained at low Atwood numbers by Ramaprabhu and Andrews (2004), Banerjee and Andrews (2006), and Banerjee (2006). In all cases, a significant anisotropy (the turbulent field is not statistically invariant to rotations or reflections of the coordinate system) of the fluid turbulence was found. Due to the buoyancy-driven nature of the turbulence, the vertical velocity fluctuations dominate the stream-wise velocity fluctuations, as indicated by the ratio $v'_{rms}/u'_{rms} \sim 1.6$ (Ramaprabhu & Andrews 2004). This anisotropy is found across the entirety of the mixing layer (top to bottom) as the dynamics are dominated by the rising and falling bubbles and spikes. Furthermore, Ramaprabhu and Andrews measured the energy density spectra of the turbulent velocity fluctuations inside the mixing layer, examining self-similarity from the additional perspective of the velocity and density fluctuations. However, experimental measures of RT fluid turbulence at large Atwood mixing layers have yet to be made and are of particular interest in the present investigation.

A new "gas channel" was constructed at Texas A&M (Banerjee & Andrews 2006), that is similar in concept and design to the Texas A&M water channel. In the gas channel, the heavy and light fluids are air and an air/helium mixture ($A_t \leq 0.75$), in contrast with the cold and hot water used in the water channel ($A_t \sim 0.001$). Banerjee (2006) used a new hot-wire measurement technique for fluid mixtures to obtain measurements of velocity variances and density-velocity cross correlations within the mixing layer at $A_t = 0.04$. Based on experimental measurements, Banerjee was able to experimentally describe the transition to self-similar behavior of the density-velocity cross correlations for the first time. Since a Rayleigh-Taylor mixing layer does not have a mean velocity gradient, there is no turbulent kinetic energy production by shearing of

the mean velocity field. This is in contrast with most other canonical turbulent flows (shear layers, jets, wakes). Measurement of the density-velocity correlation is therefore critical to understanding non-Boussinesq flows such as buoyancy-driven turbulence (Chassaing *et al*. 2002). Experimental measurements of $\overline{\rho' v'}$ serves to validate turbulence models and numerical simulations with the unique turbulence production mechanism of buoyancy-driven flows. In addition, Banerjee (2006) achieved A_t = 0.47 for the first time in an experiment of this configuration, measuring the growth parameters and average density profiles within the mixing layer in a statistically steady environment. Unfortunately, the multi-position, multi-overheat (MPMO) hot-wire diagnostic employed by Banerjee (2006) could only measure time-averaged statistics of the velocity and density fluctuations in the RT mixing layer, so that no instantaneous information for *p.d.f.*'s or spectra was available. Furthermore, the MPMO diagnostic was found to be limited to small A_t. As a result, measurements of the turbulent velocity and density fluctuations were only obtained for A_t = 0.04.

The present work extended the operating range of the facility to A_t = 0.6, the largest A_t ever achieved for miscible fluids. Thus, molecular diffusion effects in large A_t RT mixing have been observed for the first time. In addition, a new simultaneous three-wire hot-wire/cold-wire anemometer (S3WCA) diagnostic was developed, to obtain simultaneous and instantaneous measurements of velocity and density fluctuations within the RT mixing layer of air and helium. This diagnostic overcame the challenges of obtaining simultaneous measurements of velocity and density in the turbulent field of a helium/air gas mixture due to the large density and thermal property differences of helium and air. The new diagnostic provided instantaneous information to generate *p.d.f.*'s and spectra which the previous MPMO diagnostic of Banerjee (2006) could not. Furthermore, the S3WCA diagnostic obtained accurate measurements of the turbulent field at an Atwood number up to 0.6, a significant advantage over the MPMO diagnostic. A

particularly novel advantage of the present work with the S3WCA diagnostic, was the ability to measure conditional statistics of the turbulent mixing layer (separate the turbulence into bubble and spike dynamics) for the first time experimentally. The statistical measurements of the turbulent velocity and density fluctuations in the present work are the first of their kind at large Atwood number.

1.4 Hot-wire anemometry

1.4.1 Fundamentals of hot-wire anemometry

Hot-wire anemometry has been used extensively to perform velocity measurements in many fundamental shear flows (jets, wakes, shear layers). Numerous hot-wire techniques and applications are described by Bruun (1995). The principle of hot-wire anemometry relies on the convective cooling of thin wires which are resistively heated. The dynamics of a hot-wire can be described as a flow moving around a heated cylinder. The most common type of hot-wire anemometry is "constant temperature anemometry" (CTA). As the wire is convectively cooled by fluid moving around the wire, an electrical circuit adjusts the current through the wire in order to maintain a constant wire temperature. The circuit contains a Wheat-Stone bridge whose voltage, E, can be directly related to the heat transfer from the wire to the fluid. In addition, the rate at which heat is transferred from the wire to the fluid can be related to the fluid velocity (wire cooling velocity) normal to the wire, U_{eff}. In actual use, the Wheat-Stone bridge voltage is calibrated versus the wire cooling velocity. The most common expression for this relationship was proposed by King (1914) and is referred to as King's Law,

$$E^2 = A + BU^{0.5} \quad . \tag{1.5}$$

This relationship, in the simplest sense, can be used to measure a single velocity component in a given one-dimensional flow. However, this basic concept can be extended to measure multiple velocity components by using more than one hot-wire probe in orthogonal directions.

Instantaneous measurements of velocity are performed using multiple hot-wires in orthogonal orientations simultaneously. This includes the use of an X-wire (two hot-wires) and three-wire hot-wire probes. Each wire is located in orthogonal orientations and bridge voltages for each wire are sampled simultaneously, allowing for simultaneous measurement of two or three-dimensional velocity fluctuations. The hot-wire system for this investigation is a MiniCTA hot-wire anemometer system composed of three circuits and a 55P91 three-wire probe, purchased from *Dantec Dynamics*. The probe consists of three wire sensors of 5 micron diameter oriented to minimize interference effects. An analysis of the performance and behavior of three-wire probes in hot-wire anemometry has been performed by Frota and Moffat (1983) and Andreopoulos (1983).

1.4.2 Challenges of hot-wire methods in fluid mixtures

Measurements of turbulent statistics inside the helium/air RT mixing layer is challenging as the flow is primarily one-dimensional $(\overline{U}, 0, 0)$, with three-dimensional velocity fluctuations (u', v', w'). Moreover, fluid properties (υ, ρ, β, T) vary across the mixing layer, which necessitates a detailed calibration of the hot-wire with velocity and density/concentration as the independent variables. Changes in these flow properties affect the heat transfer from the hot-wire and, therefore, the performance of the hot-wire probe. In this study in particular, the large density differences of helium and air result in significantly different hot-wire responses to velocity. This can lead to significant inaccuracies in measured velocities. Progress in hot-wire

anemometry has led to applications of hot-wire techniques in flows accompanied by these previously undesired fluid property variations (multiple fluid species or temperature fluctuations). Various hot-wire techniques for concentration and velocity measurements with multiple-wire temperature (overheat) methods have been developed over the last thirty years (Banerjee 2006; Harion *et al.* 1996; Panchapakesan & Lumley 1993; LaRue & Libby 1977; McQuad & Wright 1973; and Rose 1973). Each of these techniques rely on the unique response of the hot-wire probes to velocity and fluid concentration at different wire temperatures. In principle, using hot-wires with different response characteristics in combination, allows velocity and fluid species concentrations to be determined simultaneously. However, these techniques are often performed on a time-averaged basis that yields no instantaneous information, and as such cannot satisfy the objectives of this study. In cases where instantaneous measurements are desired, specialized probes consisting of hot films and wires have been used (Harion *et al.* 1996; Panchapakesan & Lumley 1993). However, Harion *et al.* only measured one component of velocity in addition to fluid concentration, and the technique used by Panchapakesan and Lumley was demonstrated in flows with small density fluctuations.

The time-averaged multi-overheat multi-position (MPMO) diagnostic used by Banerjee (2006), was successful in validating the performance of the current gas channel facility and obtaining measurements of $\overline{\rho' v'}$, but was found to be limited to small concentrations of helium in air. This limitation was a result of assumed constant hot-wire sensitivities to helium concentrations. Unfortunately, hot-wires have a non-linear response to increasing quantities of helium (i.e. varying hot-wire sensitivities). If applied in turbulent flows with large concentrations of helium, the measurement technique would yield erroneous results. Thus, a new measurement technique has been developed in the present work that represents a significant improvement over the diagnostic used previously by Banerjee (2006). This new diagnostic,

which has been developed as a primary objective of this study, overcomes the limitations of previous hot-wire techniques by obtaining simultaneous and instantaneous measurements of velocity in density in a mixing layer with large concentrations of helium in air (i.e. large density and property differences).

1.4.3 Method for simultaneous measurements of velocity and density

Measurements of both fluid densities and velocities are required inside the Rayleigh-Taylor mixing layer that contains concentrations of both helium and air. To obtain accurate velocity measurements using a hot-wire anemometer in the gas mixture, information about the individual fluid passing the probe at any given time must be known or determinable. Although there were several methods described in the previous section, the method implemented here was developed as one of the primary objectives for this study, as no suitable diagnostic existed. What empowers this diagnostic, is the unique coupling of a temperature fluid marker for a helium/air mixture with hot-wire anemometry. Temperature fluid markers have been used in other hot-wire applications to mark turbulent fluid. However, this study uniquely incorporates a temperature marker to identify gas mixtures with large density and thermal property differences, a necessity to obtain accurate measurements of multiple velocity components and density simultaneously and instantaneously. A three-wire hot-wire anemometer is used to obtain the three-dimensional velocity fluctuations inside the mixing layer. To identify the fluid species passing the probe, a small temperature difference between the two inlet streams is used as a marker for fluid concentration. Using temperature accurately as a fluid marker is possible since the Lewis numbers for helium and air are approximately 1, so the rates of mass and thermal diffusion are similar as are the concentration and temperature. As the two streams are molecularly mixed within the mixing layer, the temperature marker transports and diffuses in the

same manner as the fluid it has marked. Thus, a constant current anemometer (cold-wire) is used to measure temperature fluctuations and identify concentration fluctuations. To ensure that the conversion from temperature to concentration (density) fluctuations is accurate, a demonstration experiment has been performed. Temperature data for fluid concentrations passing the probe is compared with helium/air velocity calibrations performed with the three-wire hot-wire probe. Velocity fluctuations are determined from the three-wire probe output voltages and the calibration. The fluid concentration information obtained from the constant current anemometer is converted to density fluctuations. Simultaneous and instantaneous measurements of temperature, density, and velocity are then made inside the Rayleigh-Taylor mixing layer. Further details of the new hot-wire diagnostic are included in Section 3.

1.5 Objectives

There are two coupled, principal objectives for this study which are necessary to advance diagnostics for complex turbulent flows and to improve the understanding of fluid physics in RT mixing. Specifically, the principal objectives of the present research are:

1. To create a new diagnostic for collection of measurements to capture the physics of RT mixing through the capability to simultaneously and instantaneously measure velocity and density fluctuations and their correlations ($\overline{v'^2}$, $\overline{w'^2}$, $\overline{\rho'^2}$ and $\overline{\rho' v'}$).
2. To use the new diagnostic to elucidate the physics of large Atwood number RT mixing.

These objectives were accomplished in a gas channel facility using air (heavy) above helium (light) to create the desired unstable fluid stratification. The tasks required to achieve these objectives are summarized as follows:

a) Demonstrate the use of temperature as a fluid marker for helium and air.

b) Develop a methodology to adapt conventional hot-wire anemometry for use in a mixture of helium and air with a temperature marker.

c) Validate the new hot-wire diagnostic at low Atwood numbers ($A_t \leq 0.1$) against existing results from the gas channel and water channel facilities.

d) Obtain the first instantaneous experimental measurements of $\rho' v'$ inside the buoyancy-driven mixing layer at low Atwood numbers ($A_t \leq 0.1$) for determination of the *p.d.f.* and energy density spectra.

e) Determine and perform the necessary modifications to the gas channel facility to achieve the largest Atwood number attempted in the facility, $A_t = 0.6$. This will require increasing the air and helium volumetric flow rates and modifying the exit flows to prevent gravity currents from adversely affecting the growth of the mixing layer.

f) Determine the mixing layer growth parameters, α_b and α_s, and verify the asymmetric growth of the bubbles and spikes of the $A_t = 0.6$ mixing layer.

g) Obtain the first statistical experimental measurements of velocity and density fluctuations at large $A_t = 0.6$.

h) Use conditional statistics to investigate the effects of large density gradients on buoyancy-driven turbulence.

2. EXPERIMENTAL FACILITY

Heavy and light fluids enter the gas channel separated by a splitter plate (refer to the schematic in Figure 2.1). The two streams enter parallel to one another, with the heavy fluid (air) above the light fluid (helium or a helium/air mixture). At the end of the splitter plate the two streams are allowed to mix. In the presence of a small perturbation and unstable stratification, a statistically steady buoyancy-driven mixing layer develops downstream of the splitter plate. An image of the mixing layer from an experiment is shown in Figure 2.2. The expected quadratic growth of the mixing layer width can be seen at late time on the left side of the image. Similar to the original water channel facility from which this experiment is derived (Snider & Andrews 1994), this facility allows for long data collection times and a statistically steady platform for studying buoyancy-driven turbulence. The primary advantage of this facility over previous water channel experiments is the ability to achieve larger Atwood numbers with the greater density differences of helium and air, and simultaneous measurements of instantaneous fluid velocities and densities.

2.1 Description and operation

The channel is constructed of clear Plexiglass to allow visualization of the developing buoyancy-driven mixing layer. The dimensions of the test section are 2.0 m long, 0.6 m wide, and 1.2 m in height. These dimensions have been scaled up from the earlier water channel facility. Three air blowers supply air to the channel, for a maximum flow velocity of 2 m/s

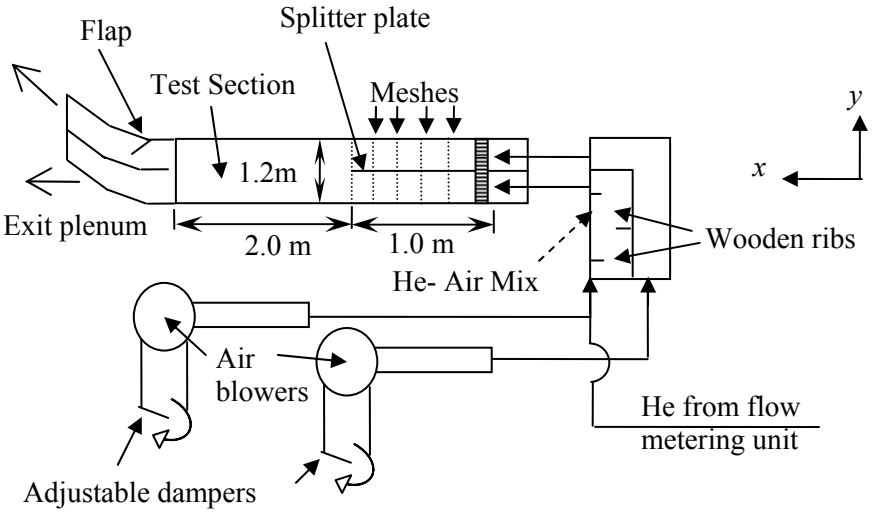

Side View

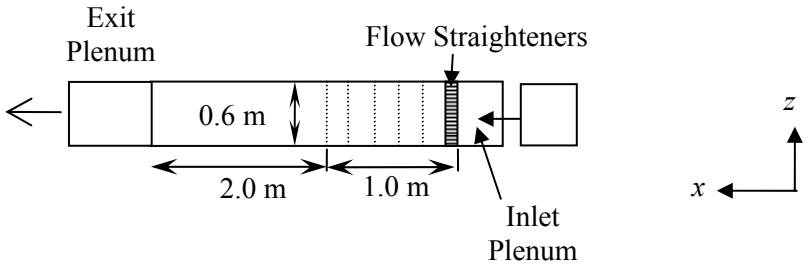

Top View

Figure 2.1. Schematic of the gas channel facility

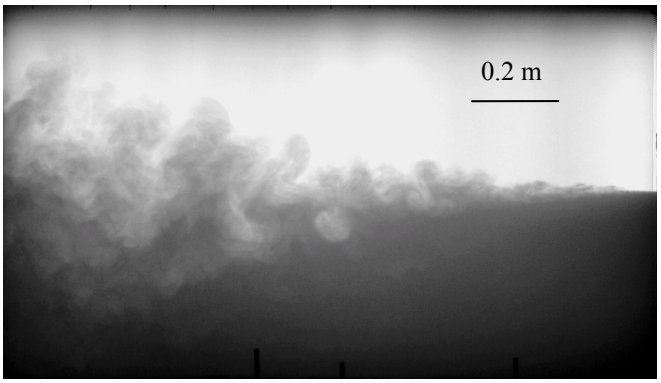

Figure 2.2. Buoyancy-driven mixing layer at A_t = 0.1 and a downstream velocity of U = 0.85 m/s. Flow is from right to left. The bottom stream (light fluid) composed of a helium/air mixture is marked by smoke. The top stream (heavy fluid) is air only.

inside the channel. To obtain a density stratification, helium is added to the bottom stream by means of a metering system. A constant helium mass flow rate is achieved by choking a helium flow supplied from compressed gas cylinders through an orifice with a constant inlet pressure. Details of the helium metering system can be found in Banerjee and Andrews (2006). The helium and air in the bottom stream are mixed prior to entering the channel, through a series of baffles in the entrance duct. Upon entering the inlet section of the channel, the top and bottom fluid streams pass through a series of honeycomb flow straighteners and a restrictive wire mesh to achieve uniformity in the downstream velocity across the expanse of the channel. The two streams remain separated by a thin stainless steel splitter plate which is 0.32 cm thick, 1.0 m long, and has a 1.8˚ knife edge at the end. After the flow straighteners, less restrictive wire meshes are used to laminarize the flow before the two streams are allowed to mix. A final wire mesh is placed at the end of the splitter plate to reduce the boundary layers forming along the splitter plate before the two streams mix (Koop 1976). The turbulence level in the free stream was experimentally measured 5 cm from the end mesh using the three-wire hot-wire anemometer, where u'_{rms}/U , v'_{rms}/U , and w'_{rms}/U were less than 2%.

Inside the Plexiglass test section the mixing layer grows in height with downstream distance and can be studied through image techniques and/or hot-wire diagnostics. At the exit of the channel, the exit plenum has been modified from the design of the earlier water channel experiments due to the formation of back-flowing gravity flows. Thus, as a result of the use of gases and the greater density differences, an alternative design for the exit plenum was needed. This new exit plenum allowed any heavy fluid to leave the channel without restriction to prevent gravity flows propagating back into the channel test section. In the new design, the exit plenum resembles two open ducts, one for the top half (containing air and mixed fluid) of the channel and another for the bottom half (containing helium and mixed fluid). The bottom exit duct opens

directly to the ambient to prevent a restriction or flow obstruction which would allow a gravity flow to return into the mixing layer. To provide some control over the mixing layer centerline, a vent fan was attached to the bottom of the exit duct and used when needed. However, the top exit duct is designed differently and contains a large flap that acts as a valve to provide control over the mixing layer centerline. In addition, since the fluid flow in the top stream may contain unmixed air (which will be neutrally buoyant to the ambient conditions) the top duct is angled vertically at the exit by 60° through two smaller turns of 30° each. This encourages all of the exit flow to move up and away from the experiment, where exhaust fans are located in the roof of the laboratory.

In instances when a temperature difference is desired between the two inlet streams (details of the necessity of this will be provided later), a 55,000 BTU kerosene forced air heater is used to heat the inlet stream. Although this large heat capacity is not always necessary, a heat source is desired that could even be used if the gas channel was used at high flow velocities for $A_t = 0.75$ (air/pure helium). In the case where not all of the heat output by the kerosene heater is required, a set of ducts resembling an upside down "T" with a small duct fan at the top exit is used to siphon off the unneeded heater output before it enters the blower inlet. Additional details of the experimental facility may be found in Banerjee and Andrews (2006).

2.2 Quantitative image analysis

Qualitative imaging and quantitative measurements of the mixing layer growth and mean density/volume fraction profiles are achieved by marking one of the fluid streams with dark green smoke (RC105, *Regin HVAC Products*). The use of a dye/smoke fluid marker is extensively used and was first implemented in the water channel facility by Snider and Andrews (1994). The dye marker and imaging technique were adapted to the gas channel facility by

Banerjee and Andrews (2006). The dye marker and image analysis was used to validate the gas channel at small Atwood number by Banerjee and Andrews (2006), and is used to provide new insight into large Atwood number Rayleigh-Taylor instabilities for the current work. The imaging technique uses a uniform backlight which allows absorption of light by the dye marker to be related to the mixture volume fraction, $f_{v,1}$ where $f_{v,1} + f_{v,2} = 1$, or density when the channel is imaged with a camera. The facility is backlit using a row of fluorescent lights evenly spaced behind the back wall of the channel. Sets of diffuser panels and a matte acetate paper between the lights and the channel wall are used to create a uniform lighted background. The experiment is photographed using a *Canon* Powershot A80 digital camera with a resolution of 1024 x 768 pixels. The camera captures images in a monochrome mode with a shutter speed of 1/160 s, aperture of F/7.1, and ISO 50. These settings yield a smoke intensity range between 110 and 220 that were found by Banerjee and Andrews (2006) to yield a desired linear response to light.

Measurement of the mixture volume fraction or density is obtained by determining the amount of light that has been absorbed by the smoke medium. Beer Lambert's Law is used to relate the extinction of light along a light ray such that the measured light intensity, I_m, is related to the intensity of the light source, I_0, through

$$I_m(x,y) = I_0(x,y)\exp\left(-\int_0^z \varepsilon\, dz\right) \approx I_0\left[1-\int_0^z \varepsilon\, dz\right] = I_0(x,y)\,(1-\omega), \qquad (2.1)$$

where ε is the extinction coefficient. A linear behavior for (2.1) is obtained up to a 60% extinction of light (Banerjee & Andrews 2006), and was verified in the present work by placing a wedge inside the channel (filled with the smoke marker) using the identical background and camera settings. A photograph of the wedge in the channel with the smoke marker is shown in

Figure 2.3. Smoke filled wedge placed in the channel in front of the backlit background. The wedge is used to calibrate the relationship between light intensity and fluid concentration through the absorption of light by the smoke marker.

Figure 2.3. The triangular geometry of the wedge calibrates a linear variation of the smoke marker concentration as viewed from outside the channel.

Care has been taken to achieve a uniform background / light source for image analysis; however, small non-uniformities do exist. A background correction relying on the principle of Equation (2.1) was first implemented by Snider and Andrews (1994) and subsequently used successfully in this facility by Banerjee and Andrews (2006). A background image without a smoke marker is recorded to determine the light source intensity, I_0, throughout the background. Ideally, the intensity of I_0 would be constant throughout the image background; however, this is not always the case. The corrected image intensity, I_{corr}, if the light source is uniform would be found similarly to (2.1) as

$$I_{corr}(x,y) = I_0^{uniform}\ (1-\omega). \tag{2.2}$$

Since ω is measured directly by comparing the measured light intensities from the background and smoke marker images, a correction was applied by Snider and Andrews by combining (2.1) and (2.2) to account for the non-uniform I_0

$$I_{corr}(x,y) = \frac{I_0^{uniform}}{I_0(x,y)} I_m(x,y)\ . \tag{2.3}$$

The corrected measured intensity, I_{corr}, can then be related to the mixture volume fraction/density. The maximum corrected intensity (where no extinction of light has occurred) corresponds to the fluid stream where no smoke marker was present. Similarly, the minimum corrected intensity (where a maximum extinction of light has occurred) corresponds to the fluid stream which was marked by smoke. The light extinction behavior is linear for the absorption regime utilized (Banerjee & Andrews 2006); therefore, the mixture volume fraction varies linearly between the minimum and maximum corrected light intensities. By averaging the captured images obtained with the digital camera, and applying the correction to the average

image of the mixing layer, average volume fraction and density measurements are obtained throughout the mixing layer.

3. SIMULTANEOUS THREE-WIRE / COLD-WIRE ANEMOMETRY

Studying Rayleigh-Taylor instabilities in the unique configuration of the current gas channel is an ideal platform for obtaining turbulent statistics within a developing mixing layer. Performing the experiment in a channel flow configuration allows for long sample times and, thus, extensive statistical measurements. Desirable diagnostics should be capable of instantaneous measurements of velocity and density statistics, velocity-density correlations, and desirably their spectra. The choice of hot-wire anemometry as a flow diagnostic in the present work is facilitated by the use of air and helium as the two fluids in the high Atwood number RT experiment (Banerjee & Andrews 2006). Point-wise hot-wire anemometry avoids possible light refraction problems of fluids with large density differences, can capture the miscible nature of the gases, and is appropriate for channel flow.

Simultaneous measurements using hot-wire and cold-wire anemometers have been used previously by Vukoslavcevic *et al.* (2005), Fabris (1979), and Hishida and Nagano (1978). However, the additional complexity of varying fluid concentration/density was not present in these instances. In the current experiment, temperature is used as a marker to distinguish helium and air. Using a temperature marker, the present S3WCA method provides instantaneous and simultaneous measurements of velocity and density fluctuations inside the RT mixing layer that comprises variable concentrations of helium and air. A three-wire probe, maintained at a $\Delta T = T_{\text{wire}} - T_{\text{amb}} = 200$ °C, coupled with three-CTA circuits is used to obtain the three-dimensional velocity fluctuations inside the mixing layer. To identify the fluid concentration passing the probe, a small temperature difference (~2 °C for $A_t = 0.03$) between the two inlet streams is used as a marker for fluid concentration; this is valid as the Lewis number (ratio of mass diffusion to thermal diffusion) is close to 1. This implies that as the two streams molecularly mix within the

mixing layer, the temperature marker will transport and diffuse in the same manner as the fluid it has marked. Use of the temperature marker was validated as follows in the next section. A cold-wire probe coupled to a constant current anemometer (CCA) circuit is used simultaneously to measure temperature fluctuations, and thereby identify concentration fluctuations of the mixture flowing over the probe. The cold-wire and three-wire probes are placed side by side with a total probe resolution of ~ 6 mm. Information about fluid concentrations passing the cold-wire probe is compared with three-wire probe output voltages, and a calibration is performed at different concentrations, resulting in accurate measurements of the velocity fluctuations. The fluid concentration information obtained from the cold-wire probe is then converted to density fluctuations. Thus, simultaneous and instantaneous measurements of temperature, density, and velocity are obtained inside the RT mixing layer.

3.1 CTA and CCA electronics and calibration

A constant temperature anemometry (CTA) based hot-wire system is used for velocity measurements in the present study. The measuring system consists of (a) three Mini-CTA anemometers (Model 54T30, *Dantec Dynamics*); (b) Single Normal (SN) Hot-wire probe (Model 55P16, *Dantec Dynamics*) and a three-wire hot-wire probe (Model 55P91, *Dantec Dynamics*); and (c) a SC 2040 Sample and Hold Board (*National Instruments*) connected to a PCI-MIO-16E-4 A/D board (*National Instruments*). The computer is connected to a *Tripp Lite* IS-1000 isolation transformer to eliminate electrical line noise from the acquired anemometer signals. The hot-wire sensors are 5 μm diameter Pt-T wire with a length of 1.25 mm. Hot-wire calibration is performed to establish the relationship between the CTA voltage output (E), fluid velocity (U_{eff}), and the helium concentration [$f_{v,he} = \rho_{he} / (\rho_{he} + \rho_{air})$] exposing the probe to a

set of known velocities and then recording the output anemometer voltages for varying concentrations of helium in air. Calibration is carried out in a dedicated probe calibrator that consisted of a proportioner meter (Model # P21A1-BA2, *Aalborg Corp*.) to control the amounts of air and helium. Gas flow rates up to 70 L/min through air and helium rotameters are used for hot wire calibration. A PVC pipe is connected to the outlet port of the proportioner meter, as a small calibration wind tunnel, consisting of plastic PVC tubing and restrictive wire meshes to keep the velocity profile uniform and reduce boundary layers. With this configuration, probes are calibrated over a range of downstream velocities of approximately 0.3 – 2.3 m/s, with mixture concentrations ranging from pure air to pure helium. Further details of the calibration facility and procedure are included in Appendix A.

Temperature measurements are obtained using a constant current anemometer (CCA, *AA Lab Systems*). The CCA was selected over conventional thermocouples for the improved time response (~ 1 kHz). Unlike the CTA, the CCA neglects the resistive heating of the wire probe by using small currents, so that the wire resistance was linearly related to the wire temperature. An output voltage, E_{cw}, from the CCA circuit is subsequently related to changes in wire resistance and fluid temperature by

$$E_{cw}(t) = R_{ref}\, I\,[T_{wire}(t) - T_{ref}]\,, \tag{3.1}$$

where I is the current through the wire, and R_{ref} is the cold resistance of the wire at temperature T_{ref}. Further details on CCA can be found in LaRue (1975). Calibration of a SN wire probe (55P16) for a voltage-temperature response is performed by heating an air flow in the channel, using a electrical resistance heater over the range of temperatures expected in the experiment. The anemometer voltage and the fluid temperature measured via a calibrated thermocouple are recorded simultaneously, thus giving a calibrated voltage response which can be used to measure

temperature via the cold-wire anemometer. Further details for the cold-wire anemometer can be found in Appendix B.

3.2 Fluid marking by temperature

The relationship between measured fluid temperature and volume fraction (or density) of the fluid passing the probe is obtained by assuming an ideal gas behavior for the gas mixture, and using an energy balance between the two streams as:

$$\dot{m}_{mix} c_{p,mix} T_{mix} = \dot{m}_1 c_{p,1} T_1 + \dot{m}_2 c_{p,2} T_2 \tag{3.2}$$

where, $c_{p,\mathrm{i}}$ is the specific heat at constant pressure of stream i (*1*: air on top; *2*: air-helium mixture on bottom), T_i is the temperature of each stream and $\dot{m}_\mathrm{i}$ is the mass flow rates for each stream. The mass fraction of stream 2 (lighter stream), where $f_{m,2} = \dot{m}_2 / (\dot{m}_1 + \dot{m}_2)$ and $f_{m,1} + f_{m,2} = 1$, can be directly solved as:

$$f_{m,2}(t) = \left[1 + \frac{c_{p,2}}{c_{p,1}} \frac{T_2(t) - T_{mix}(t)}{T_{mix}(t) - T_1(t)} \right]^{-1}, \tag{3.3}$$

where T_1, T_2, and T_{mix} (cold wire) are the instantaneously measured temperatures. Equation (3.3) yields a time trace of mass fraction, $f_{m,2}$. For the range of temperature difference used in the present study, (≤ 5 °C), the effect of temperature variation on specific heat is assumed to be negligible, and pure fluid specific heats are taken to be constants. Thus, the volume fraction of fluid 2, $f_{v,2}$, can be calculated using the inlet stream densities and from measured temperatures inserted into (3.3) to give $f_{v,2}$ as

$$f_{v,2}(t) = \frac{\rho_1}{\rho_1 - \rho_2 + \rho_2 / f_{m,2}(t)}. \tag{3.4}$$

Since $f_{v,1} + f_{v,2} = 1$ the density of the fluid passing the probe is

$$\rho_{mix}(t) = \rho_1 f_{v,1}(t) + \rho_2 f_{v,2}(t). \tag{3.5}$$

A simple demonstration experiment illustrates the concept of fluid marking by temperature. In the demonstration experiment (schematic shown in Figure 3.1(a)), the proportioner meter used previously for calibrating the hot-wire probes delivers known volumetric flow rates of helium. An air blower from the gas channel facility is diverted and used to provide the air supply. The two flows are combined at a PVC-T junction and directed downstream through a pipe containing a series of baffles to thoroughly mix the two pure fluid streams. The pipe is 1.25 cm diameter, and the bulk velocity of air through the pipe was approximately 4 m/s. The high air velocity and baffles in the pipe create a turbulent flow downstream in the pipe that results in an approximately flat, average velocity profile across the pipe. A small electric heater warms the air supply and creates the desired temperature difference, which in this case was ~ 5 °C. The entire pipe was heavily insulated to prevent significant heat losses through the pipe wall (heat loss reduced to ~ 1.7% of the 5 °C temperature difference measured via thermocouples and an energy balance). The inlet stream temperatures and the downstream mixture temperature are measured using a handheld J-type thermocouple. This experimental setup proportions a known mixture by design, and serves as a calibration for mixture concentration measurements that use temperature as a marker. The mixture concentration based on the theory of equations (3.2)-(3.5) and temperature, is compared with the experimentally calibrated values. Figure 3.1 (b) shows good agreement between the known and temperature marked mixture concentration values, indicating that temperature is effective as a fluid marker in the air and helium mixtures of our experiment.

For accurate measurement of the fluid concentration/density in the RT mixing layer, a temperature difference (ΔT) between the two inlet streams in the experiment must be selected. However, there are limitations with selecting an arbitrarily large temperature difference, as

(a)

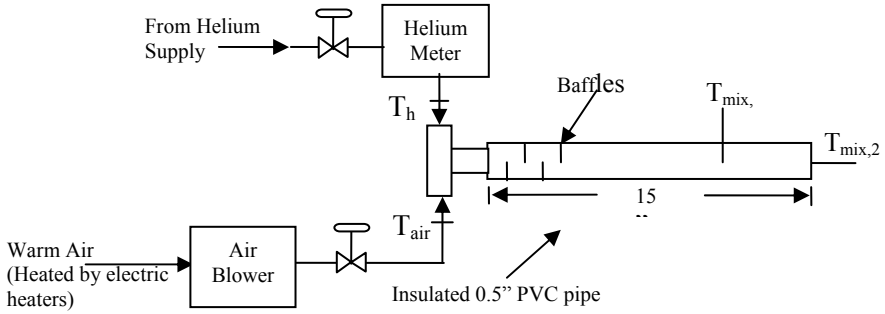

(b)

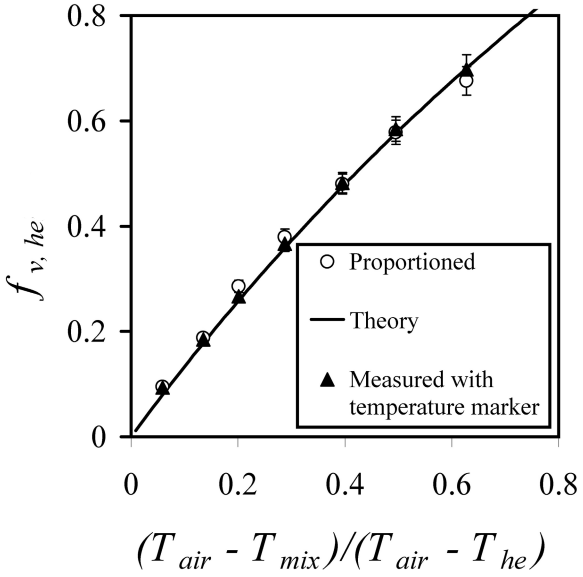

Figure 3.1. (a) Schematic of a calibration experiment used to verify the use of temperature as a fluid marker. (b) Comparison between the experimental results and theory, verifying the use of temperature as a fluid marker for identifying mixtures of air and helium.

increasing ΔT between the two inlet streams is detrimental to the hot-wire diagnostic, and fluid densities can be significantly altered by a large ΔT. Table 3.1 illustrates the uncertainty that can be created by a large temperature difference, through its influence on the Atwood number for the Rayleigh-Taylor mixing layer. For the experiments at A_t = 0.03, the temperature difference between the two inlet streams was maintained at approximately 2 °C which resulted in a 6% uncertainty in the Atwood number. For A_t = 0.6 a temperature difference between the inlet streams of approximately 5 °C was used which resulted in a 2% uncertainty in the Atwood number.

Another effect of varying fluid temperatures inside the gas channel is to increase the inaccuracies in the velocity measurement. By varying fluid temperature, the hot-wire response deviates from the calibrated response as the temperature conditions for convective heat transfer between the wires and fluid change. A temperature correction described by Kanevce and Oka (1973) is applied to the hot-wire voltages as

$$E^2_{corr}\left(T_{ref}\right) = E^2\left(T_{mix}\right)\frac{T_{wire} - T_{ref}}{T_{wire} - T_{mix}}, \tag{3.6}$$

where the fluid temperature, T_{mix}, exposed to the hot-wires is supplied via the cold-wire diagnostic, and the calibration reference temperature is T_{ref}. Equation (3.6) is effective for the present measurements, and adequately accounts for variation in temperature between calibration and experiments. An example and verification of the temperature correction procedure, in addition to further details and considerations for use of temperature as a fluid marker, is included in Appendix C.

A_t	ΔT (°C)	Percent Change of A_t
0.01	5	45
0.10		6
0.50		3
0.75		1

Table 3.1. Effect of ΔT on the Atwood number.

3.3 Helium and air hot-wire calibration and determination of velocities

To accurately determine velocity measurements inside the mixing layer, a calibration must be performed over the expected velocity and concentration range of helium and air. Thus, if the mixture of helium and air passing the three-wire probe is identified, the appropriate velocity response can be invoked. A typical calibration is shown in Figure 3.2 for wire 1 of the three-wire probe. A similar response behavior was found for wires 2 and 3. King's law scaling (E^2 *vs.* $U_{eff}^{0.5}$) was used to linearize the calibration data, where U_{eff} is the component of velocity normal to each sensor. The calibration is used with the anemometer output voltages to determine sensor effective velocities through a linear interpolation between the King's law fit for each calibrated concentration of helium.

The helium/air calibration of the hot-wire probes is then used with the measured hot-wire voltages and fluid concentration to accurately determine the hot-wire effective velocities, U_{eff}. Conversion of the three sensor effective (normal) velocities to measurements of global velocities is performed using the reduction procedure described by Bruun (1995). In particular, Bruun gives pitch/yaw equations (Jorgensen 1971; Gaulier 1977; Frota & Moffat 1983) for the effective velocity, that are coupled with the probe geometry to reduce the orthogonal hot-wire effective velocities ($U_{eff,1}$ $U_{eff,2}$ $U_{eff,3}$) to ones in the global coordinate system (U,V,W). This procedure has been commonly used for converting voltage outputs from the 55P91 three-wire probe to velocity measurements. For illustrative purposes, the order of steps in the conversion procedure and the interactions between the hot-wire and cold-wire anemometers during various steps of the analysis are shown in Figure 3.3. The final outputs of the SW3CA diagnostic are

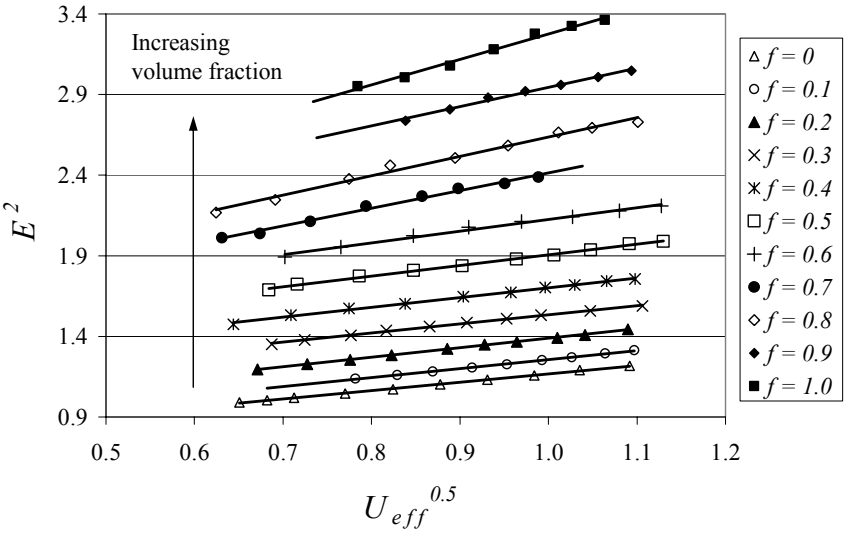

Figure 3.2. Sample calibration from Wire 1 of the three-wire hot-wire probe for concentrations of helium and air.

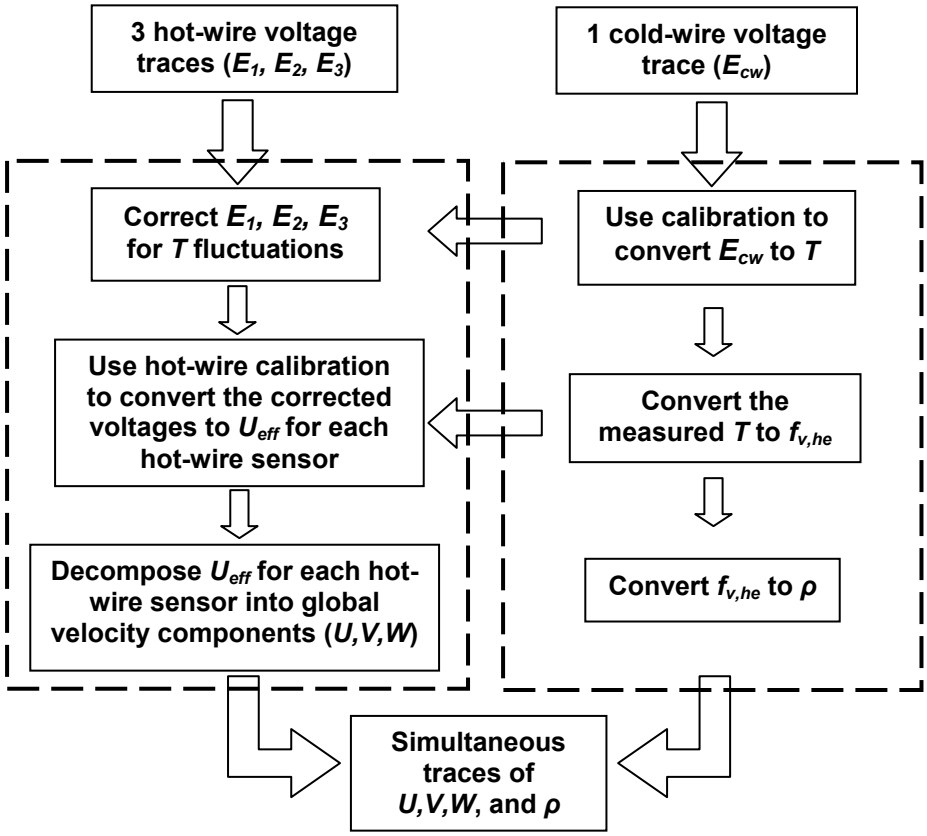

Figure 3.3. Flowchart for determination of velocity and density inside the helium/air mixing layer simultaneously using a three-wire hot-wire anemometer and a cold-wire anemometer.

simultaneous and instantaneous traces of the three-components of velocity and density. A complete description of the equations and data reduction procedures is provided in Appendix D. In addition, air only measurements in a shear layer were performed as an initial check of the data reduction procedure and are included in Appendix E.

3.4 Limitations and uncertainties of the S3WCA diagnostic

Care must be taken when using multiple hot-wires in highly turbulent flows, as hot-wire anemometry is restricted to low and moderate turbulent intensity flows, where u'_{rms}/U, v'_{rms}/U, and w'_{rms}/U are typically less than 25% (Bruun 1995). This limitation may be attributed to the insensitivity of hot-wires to the flow direction, ambiguity of the voltage signal when the velocity vector lies outside the approach cone, large probe volumes, and the limited pitch/yaw response of the probes (Frota & Moffat 1983, Andreopoulous 1983, Bruun 1995). In the current work, a conservative requirement limited the instantaneous velocity vectors to approach angles with the probe axis of ~ 20º, based on the earlier analysis for three-wire (55P91) hot-wire probes of Frota and Moffat (1983) and Andreopoulos (1983). A simple application of this 20º limit is given by approximating the instantaneous velocity vector in two dimensions using $2v'_{rms}$ as the vertical velocity component for the instantaneous velocity vector and the mean advective velocity, U_m, as the horizontal component of the instantaneous vector. Twice the v'_{rms} is used so that the vector satisfies all vertical velocity fluctuations within a 95% confidence interval. This approximation results in a turbulent intensity limit of 20% for the dominant vertical velocities in the buoyancy-driven flow, and can used as a guide to design future experiments.

Furthermore, the S3WCA diagnostic is also limited to Atwood numbers such that an applied temperature difference does not adversely affect the fluid densities, and subsequently the

Atwood number itself. As a result, this diagnostic cannot be applied to very small Atwood number flows, $A_t < 0.03$. In addition, the combined spatial resolution of the cold-wire and three-wire hot-wire probes limits the frequency response of the combined system. Using a spatial resolution of 6 mm and the advection velocity for the flow, the Nyquist limit implies a frequency response of approximately 50 Hz for $A_t = 0.03$. However, as the flow channel velocity for the experiment is increased to reach higher A_t, the frequency response increases. Limitations on the diagnostic performance due to high concentrations of helium at $A_t = 0.6$ has doubled the spatial resolution of the S3WCA diagnostic to 1.2 cm, resulting in only an increase in frequency response to ~ 80 Hz at $A_t = 0.6$. The effect of high concentrations of helium on the hot-wire diagnostic is discussed in more detail in Section 5.

The combined methodology of Kline and McClintock (1953) and Benedict and Gould (1996) was used to estimate uncertainties in statistical measurements using the SW3CA diagnostic. The propagation of error from measurements of anemometer voltages and experimental design parameters to instantaneous measurements of velocity and density have been determined using the analysis of Kline and McClintock and Benedict and Gould. The primary contributions to uncertainty in the measurements obtained are the metering processes for the inlet stream mixtures, the hot-wire sensitivities to concentrations of helium, identification of helium concentrations from the temperature marker, and the total number independent samples obtained. A summary of the individual uncertainties and an outline of the analysis is included in Appendix F. The direct output of the S3WCA diagnostic are instantaneous velocity components and density, with uncertainties estimated, as described in Appendix F, as 7% and 5%, respectively. Uncertainties in the statistical (multiple sample measurements) measurements of velocities and their variances (~ 16%) are larger than those reported for the MPMO diagnostic (~5%) used previously in the gas channel by Banerjee (2006). However uncertainties of 16%

for the variance of measured velocity fluctuations by the S3WCA diagnostic is reasonable for a hot-wire diagnostic (Bruun 1995), although not as accurate as the time-averaged MPMO diagnostic. However this is expected as the MPMO technique does not determine instantaneous measurements, but rather determines time-averaged statistics directly from time-averages of the hot-wire voltage fluctuations. In the MPMO diagnostic, time-averaging reduces the hot-wire response to a system of algebraic equations, which results in a more robust measurement and solution. The complexity and instantaneous nature of the S3WCA diagnostic results in larger measurement uncertainties, however, it is a more powerful measurement tool.

The use of temperature as a fluid marker for determining density has been previously used in the water channel facility (Mueschke *et al.* 2006). The subsequent measurement of density is used to quantify molecular mixing and determine the turbulent mass flux within the mixing layer. The estimated uncertainty of the density fluctuation variance is 12% which results in an 8% uncertainty for the calculated molecular mixing parameter, θ. This estimate is in agreement with estimates by Mueschke *et al.* (2006) for their similar diagnostic. Estimates of the uncertainties of the turbulent mass fluxes ($\overline{\rho' u'}$, $\overline{\rho' v'}$, and $\overline{\rho' w'}$) are 34%, 3%, and 20% respectively. The percent uncertainties of the turbulent mass flux in the horizontal directions are large since their magnitudes are small and ideally zero in RT flows due to the symmetrical nature of a plume. Inversely the percent uncertainty of $\overline{\rho' v'}$ is small since the vertical turbulent mass flux itself is large as it is responsible for the transport of mass and production of the turbulent kinetic energy within the mixing layer. A more complete listing of individual uncertainties and description of the analysis procedure is included in Appendix F.

4. SIMULTANEOUS MEASUREMENTS OF VELOCITY AND DENSITY AT SMALL ATWOOD NUMBER

The S3WCA hot-wire diagnostic was used to obtain detailed measurements of turbulent statistics in a RT mixing layer. The capabilities of the technique are discussed here with reference to measurements of u' , v', w', $\overline{\rho'^2}$, $\overline{\rho' v'}$ and the corresponding time-traces of these quantities inside the developing mixing layer of helium and air for A_t = 0.03. These results were used to validate the hot-wire technique at low A_t, and provide a description of the physics of the turbulent flow. Previous experimental measurements from Ramaprabhu and Andrews (2004) and Mueschke *et al.* (2006) at A_t = 7.5 x 10^{-4} obtained using a water channel facility with particle image velocimetry (PIV) and thermocouple diagnostics were used for comparison. In addition, experimental measurements in the gas channel using a multi-position, multi-overheat (MPMO) hot-wire technique from Banerjee (2006) were used for comparison. The first experimental, instantaneous measurements of $\overline{\rho' v'}$ at any A_t are shown, including its *p.d.f.* and energy density spectra. The behavior of $\overline{\rho' v'}$ is important for its role in driving the conversion of potential to kinetic energy in buoyancy-driven turbulence (Livescu & Ristorcelli 2007). A summary of the experiments and available diagnostics is shown in Table 4.1.

4.1 Measurement of velocity correlations and growth parameters

Due to the buoyancy-driven nature of the flow, the mixing layer is dominated by velocity fluctuations in the vertical direction (direction of gravity). Small perturbations at the

Facility	Technique	A_t	$\overline{U}$ (cm/s)
Water channel	PIV (Ramaprabhu & Andrews 2004)	7.5×10^{-4}	4.3
Gas channel	Multi-position hot-wire (MP) (Banerjee & Andrews 2006)	0.035	60
	Multi-position, multi-overheat hot-wire (MPMO) (Banerjee 2006)	0.04	50
	*Simultaneous three-wire hot-wire / cold-wire (S3WCA)	0.03	65

* Current experiment

Table 4.1 Summary of small Atwood number experiments used for calibration/verification purposes.

interface between the two fluids grow, developing into a turbulent mixing layer. The finger-like growth of the initial interfacial perturbations are characteristic of Rayleigh-Taylor instabilities. In addition, mushroom shaped plumes are prevalent in this type of flow. The growth of interpenetrating rising bubbles and falling spikes within the mixing layer is quadratic at late-time once the flow has become self-similar (Youngs 1984), with the bubble penetration distance from the initial interface

$$h_b = \alpha_b A_t g t^2 \tag{4.1}$$

for small A_t. A correlation between the vertical velocity fluctuations, v'_{rms}, at the centerline (y = 0) of the mixing layer and the growth rate of the mixing layer half width, h_b, was found by Ramaprabhu and Andrews (2004) as

$$v'_{rms} = \frac{dh_b}{dt} = 2\alpha_{CL} A_t g t = 2\alpha_{CL} A_t g \frac{x}{\overline{U}}. \tag{4.2}$$

Equation (4.2) is convenient for determining the growth parameter (α_{CL}) and provides validation for the measured vertical velocity fluctuations. Figure 4.1 compares the measured growth parameters for the water channel experiments of Ramaprabhu and Andrews (2004), a simple multi-position hot-wire diagnostic (MP) used by Banerjee and Andrews (2006) in the current facility, the multi-position, multi-overheat (MPMO) diagnostic of Banerjee (2006), and the measured growth parameter using the current S3WCA hot-wire method developed as a primary objective for this work. The measured α_{CL} are plotted versus non-dimensional time $\tau = \left(x / \overline{U}\right)\sqrt{A_t g / H}$,where H is the channel height. Once the flow is self similar α_{CL} reaches an asymptotic value. Inspection of Figure 4.1, reveals that the various experiments and measurement methods result in similar measurements of α_{CL}. In particular, a growth parameter

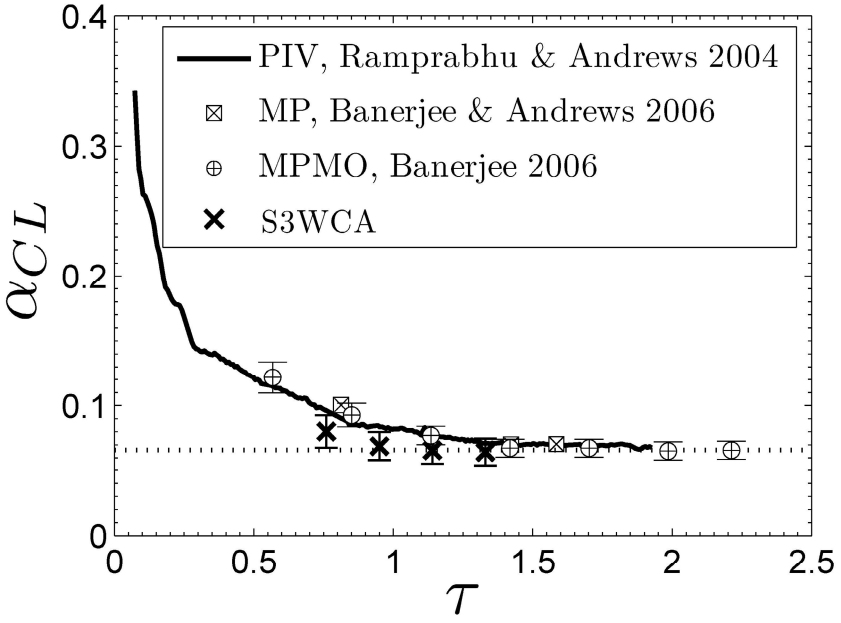

Figure 4.1. Comparison of the measured growth parameter, α_{CL}, determined from the vertical velocity fluctuations at the mixing layer centerline.

of 0.064 was found using the S3WCA diagnostic. This agrees well with the previous measurements α_{CL} = 0.066 using the MPMO diagnostic in the gas channel and 0.070 using PIV in the water channel. The new measurement of α_b is also comparable with the measured range α_b = 0.044 – 0.070 as reviewed from literature by Ramaprabhu and Andrews (2004).

Anisotropy and dominance of the vertical velocity fluctuations, v'_{rms}, has been experimentally shown by Ramaprabhu and Andrews (2004) and found across the entire mixing layer width. This strong anisotropy contrasts with shear-driven turbulence where the stream-wise velocity fluctuations, u'_{rms}, dominate the turbulence. Table 4.2 summarizes velocity fluctuation anisotropy for the previous water channel measurements and the new measurements obtained using hot-wire. In each case it can be seen that the vertical velocity fluctuations dominate the late-time turbulence. In the MPMO technique, the u' and w' fluctuations were assumed to be equal in the hot-wire response equations. However, the SW3CA diagnostic can measure velocity fluctuations in the cross-stream, *W*, direction as well. Velocity fluctuations in the horizontal directions (u' and w') are close in magnitude, but not necessarily equal. This may be due to the effects of helium or a remnant of the two-dimensional initial conditions. A similar result was found in the gas channel using the simplified MP hot-wire technique by Banerjee and Andrews (2006), where $u'/w' = 1.1$. The effect of the buoyancy-driven nature of the flow on vertical velocity fluctuations can also be seen in the *p.d.f*'s of the measured velocity fluctuations at the centerline of the mixing layer, which is shown in Figure 4.2. The vertical velocity fluctuations, v', exhibit a flat *p.d.f.* due to the broad spectrum of scales that develop from the rising and falling bubbles and spikes within the mixing layer. However, stream-wise and cross-stream velocity fluctuations, u' and w', both exhibited approximately Gaussian behavior, as small velocity fluctuations dominate and were more likely to be present.

	S3WCA	MPMO	PIV
τ	**1.33**	**1.42-2.21**	**1.2-1.7**
v'/u'	**1.5**	**1.7**	**1.6**
v'/w'	**1.7**	**-**	**-**
u'/w'	**1.2**	**-**	**-**

Table 4.2. Anisotropy of measured velocity fluctuations compared with previous small Atwood number measurements.

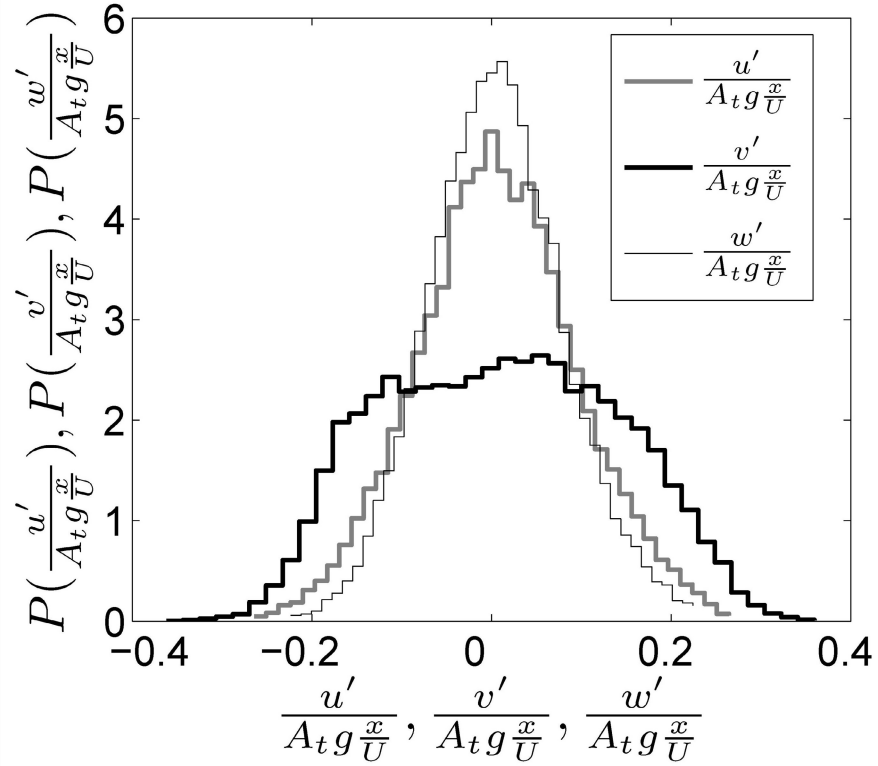

Figure 4.2. *P.d.f.* 's of the measured centerline velocity fluctuations using the S3WCA technique at the centerline of the mixing layer for $A_t = 0.03$ and $\tau = 1.33$.

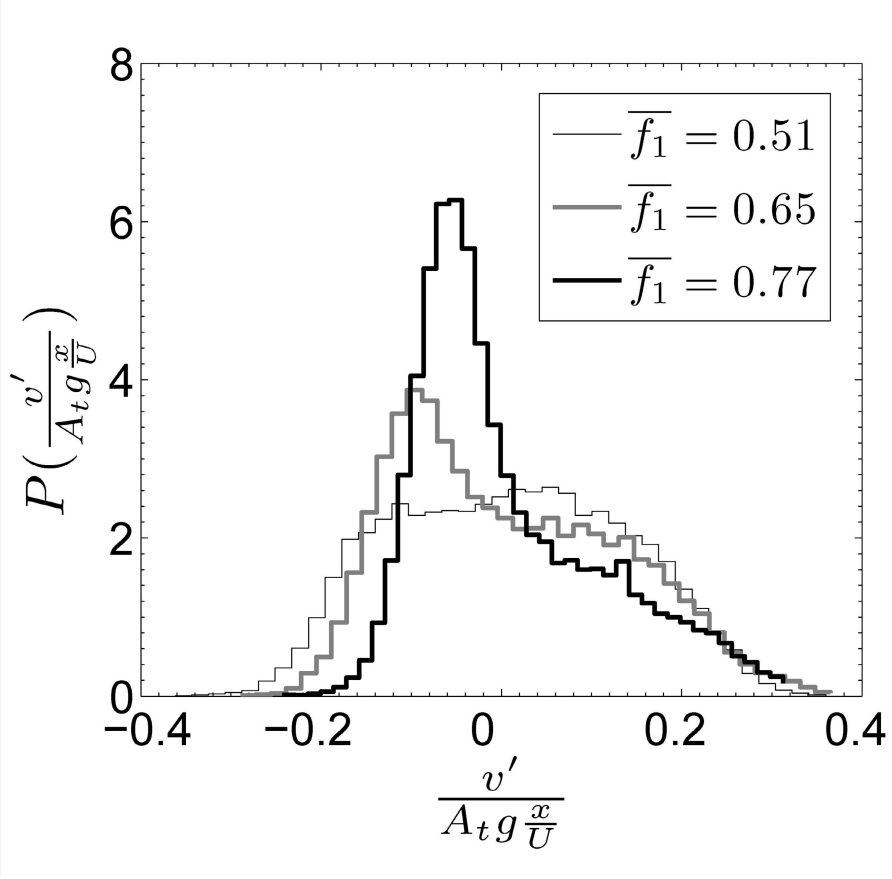

Figure 4.3. *P.d.f.* of the vertical velocity fluctuations using the S3WCA technique at $\tau = 1.33$ across the mixing layer with average volume fractions of fluid 1, $\overline{f}_{v,1}$ = 0.51, 0.65, and 0.77. The properties of the these distribution are determined for

$\overline{f}_{v,1}$ = 0.51 where $\overline{v'^2} = 0.010$, $K_{v'} = 2.2$, $S_{v'} = \overline{v'^3} \Big/ \left(\sqrt{\overline{v'^2}}\right)^3 = 0.05$;

$\overline{f}_{v,1}$ = 0.65 where $\overline{v'^2} = 0.0096$, $K_{v'} = 2.3$, $S_{v'} = 0.43$; and

$\overline{f}_{v,1}$ = 0.77 where $\overline{v'^2} = 0.0067$, $K_{v'} = 3.1$, $S_{v'} = 0.90$.

Quantitatively, the flatness of these *p.d.f*'s can be compared using their kurtosis,

$$K_u = \frac{\overline{u'^4}}{\left(\overline{u'^2}\right)^2}, \quad K_v = \frac{\overline{v'^4}}{\left(\overline{v'^2}\right)^2}, \quad K_w = \frac{\overline{w'^4}}{\left(\overline{w'^2}\right)^2} \tag{4.3}$$

for the velocity fluctuations. For a Gaussian distribution the kurtosis is 3; as the kurtosis decreases the distribution flattens. For the measured velocity fluctuations at $\tau = 1.33$, a kurtosis of 2.9, 3.0, and 2.2 was found for u', w', and v', respectively. This compares well with the measured kurtosis for the centerline vertical velocity fluctuations in the water channel facility, where $K_v = 2.3$ at $\tau = 1.21$. The low value of K_v (< 3.0) implies that rather than having short, intermittent bursts of *v'* and related turbulence, the vertical velocity fluctuations and turbulent structure of the rising bubbles and falling spikes generates a broad spectrum of scales. Dominance of vertical velocity fluctuations is consistent across the mixing layer (Banerjee 2006; Ramaprabhu & Andrews 2004). However, the distribution of the measured vertical velocity fluctuations does change the behavior away from the mixing layer centerline. Measured *p.d.f.*'s of the vertical velocity fluctuations at $\tau = 1.33$ are shown in Figure 4.3 at the mixing layer centerline ($\overline{f}_{v,1} = 0.51$), and in the top half of the mixing layer with average volume fractions of $\overline{f}_{v,1} = 0.65$ and $\overline{f}_{v,1} = 0.77$. As the volume fraction of $\overline{f}_{v,1}$ increases (moving into the top half of the mixing layer) more heavy fluid is present, and negative velocity fluctuations become more likely as heavy fluid entrained at the edge of the mixing layer is transported down through the mixing layer. This results in the observed asymmetry in the measured vertical velocity fluctuation *p.d.f.*. In addition, the intensity of the turbulence in the mixing layer decreases towards the edges of the mixing layer, resulting in a narrower range (smaller variance) of measured vertical velocity fluctuations.

4.2 Measurement of density correlations and molecular mixing parameters

Unlike small density gradient flows where density or concentration is passive to the flow dynamics, the effects of density fluctuations and local density gradients dominate in Rayleigh-Taylor mixing layers. More precisely, density fluctuations were found to couple with $\partial P/\partial y$ as a primary source for the turbulent mass flux, $\overline{\rho' v'}$ (Steinkamp *et al.* 1999). Therefore, buoyancy drives the turbulence and as fluid is molecularly mixed, density fluctuations decrease and the growth of the mixing layer and turbulence may be reduced. Turbulent mixing of the two fluids may be quantified by the molecular mixing parameter (Danckwerts 1952)

$$\theta = 1 - \frac{B_0}{B_2} \quad , \tag{4.4}$$

where

$$B_o = \lim_{T\to\infty} \frac{1}{T} \int_0^T \frac{(\rho - \bar{\rho})^2}{(\Delta\rho)^2} dt; \;\; B_2 = f_{v,1} f_{v,2} \tag{4.5}$$

with

$$f_{v,1} = \lim_{T\to\infty} \frac{1}{T} \int_0^T \frac{\rho - \rho_2}{\rho_1 - \rho_2} dt; \;\; f_{v,2} = 1 - f_{v,1}. \tag{4.6}$$

The volume fractions $f_{v,1}$ and $f_{v,2}$ are the volume fractions of fluid 1 and 2, B_o is the non-dimensional density auto-correlation ($\rho'^2/(\Delta\rho)^2$), and B_2 is the same correlation for a two fluid, immiscible case. Thus, θ = 1 if the two fluids are perfectly mixed and the density auto-correlation is 0. However, if the two fluids are immiscible and are stirred/folded by the turbulent flow field rather than molecularly mixed, then θ = 0. Figure 4.4 shows the measured molecular

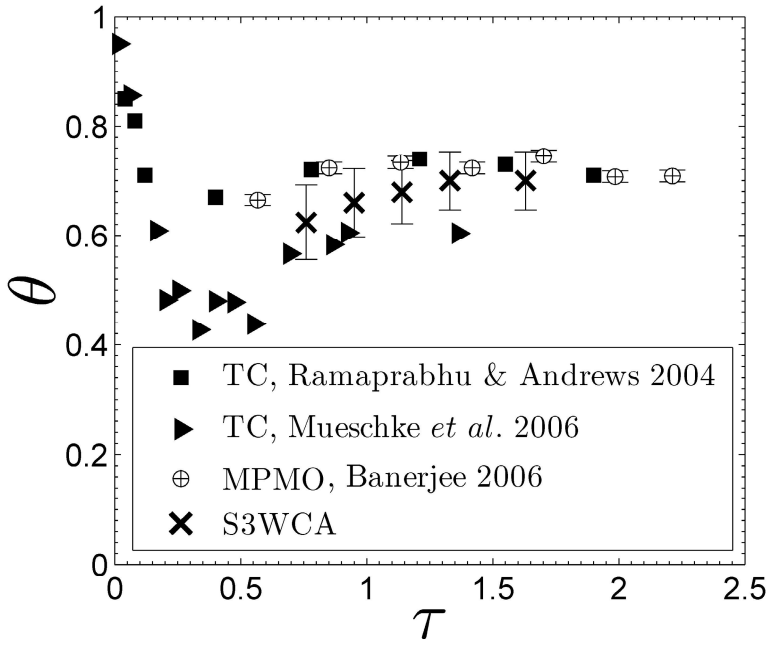

Figure 4.4. Measurements of molecular mixing, θ, at the centerline of a Rayleigh-Taylor mixing layer. A comparison is shown for measurements previously obtained in the water channel with the results from the gas channel using the new hot-wire methods.

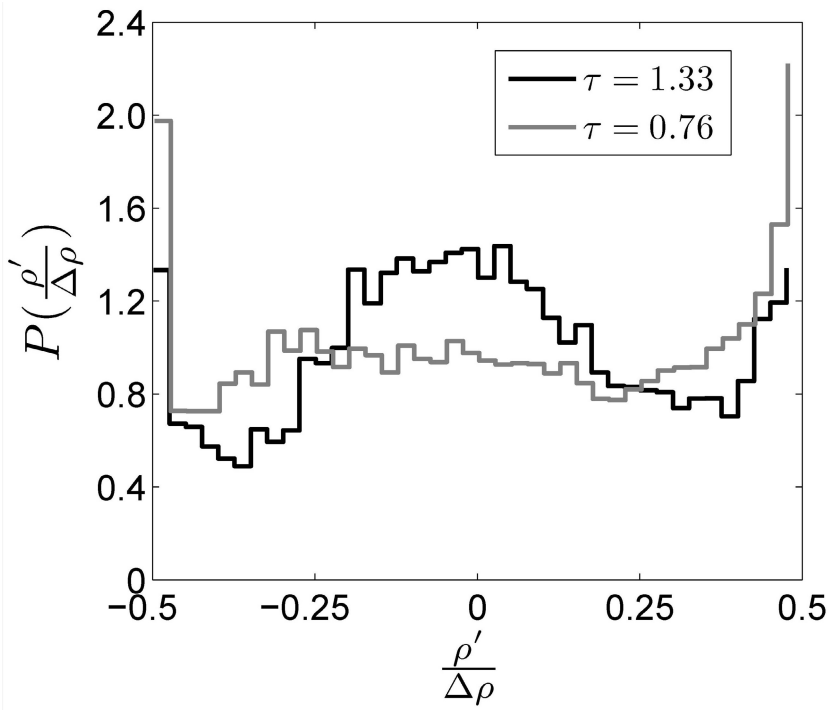

Figure 4.5. *P.d.f* of density fluctuations at the centerline of the mixing layer using the SW3CA technique.

mixing parameter at the centerline of the mixing layer using the SW3CA hot-wire diagnostic compared with previous thermocouple (TC) measurements from the water channel (Mueschke *et al.* 2006; Ramprabhu & Andrews 2004), and the gas channel (Banerjee 2006). The comparison in Figure 4.4 shows that the new hot-wire measurements in the gas channel are consistent with previous results from the water and gas channel, where a significant amount of molecular mixing was found at late-time, with $\theta = 0.70$. This can also be demonstrated by inspecting the *p.d.f.* of the density fluctuations obtained using the SW3CA technique and shown in Figure 4.5 for downstream locations of $\tau = 0.76$ and $\tau = 1.33$. At early time, $\tau = 0.76$, the *p.d.f.* exhibits a bi-modal distribution with peaks that correspond to two pure fluids. However, at late-time the probability of small density fluctuations (mixed fluid) increases, resulting in a broad peak in the center of the distribution. This broad peak confirms an increased level of molecular mixing shown in Figure 10 at late-time.

4.3 Measurement of the density-velocity correlation

As mentioned in the introduction, a primary goal of the measurement technique is to measure the density-velocity correlation $\overline{\rho' v'}$. Understanding the behavior of $\overline{\rho' v'}$ is necessary to validate turbulence models which rely on the vertical turbulent mass flux to describe the production of kinetic energy from potential energy within the fluid flow (Livescu & Ristorcelli 2007). The evolution of $\overline{\rho' v'}$ at the mixing layer centerline is shown in Figure 4.6 (a) using the SW3CA diagnostic and compared with the measurements of Banerjee (2006) using the MPMO diagnostic. The $\overline{\rho' v'}$ correlation is the turbulent mass flux in the vertical direction and is expected to be negative because rising bubbles result in positive vertical velocity fluctuations that correspond with negative density fluctuations of the lighter bubble, and vice versa for the

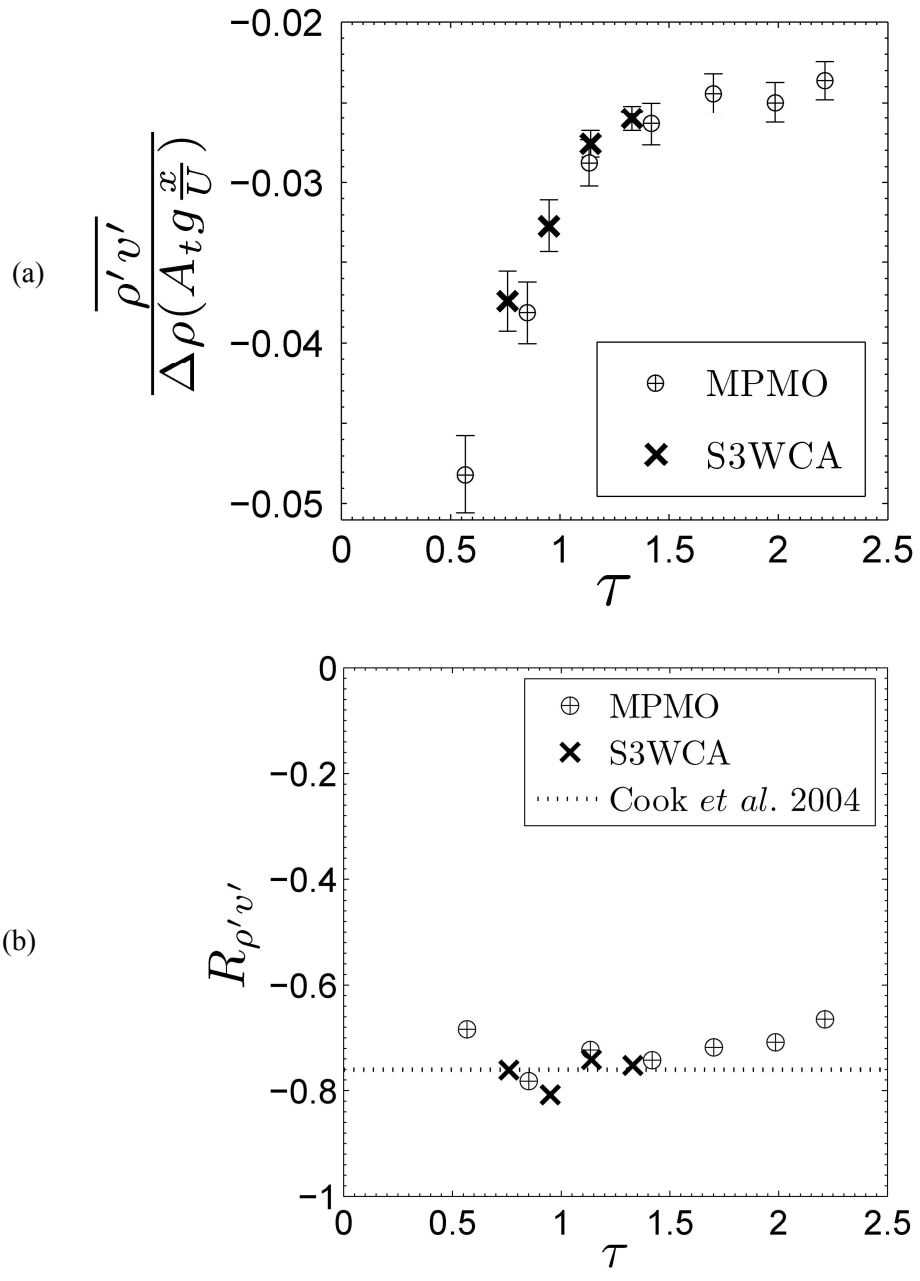

Figure 4.6. (a) The centerline evolution of the density-velocity correlation, $\overline{\rho' v'}$, inside the Rayleigh-Taylor mixing layer using data from Banerjee (2006) with the MPMO diagnostic and the current S3WCA diagnostic. (b) The non-dimensional correlation coefficient $R_{\rho' v'}$ at the centerline of the mixing layer.

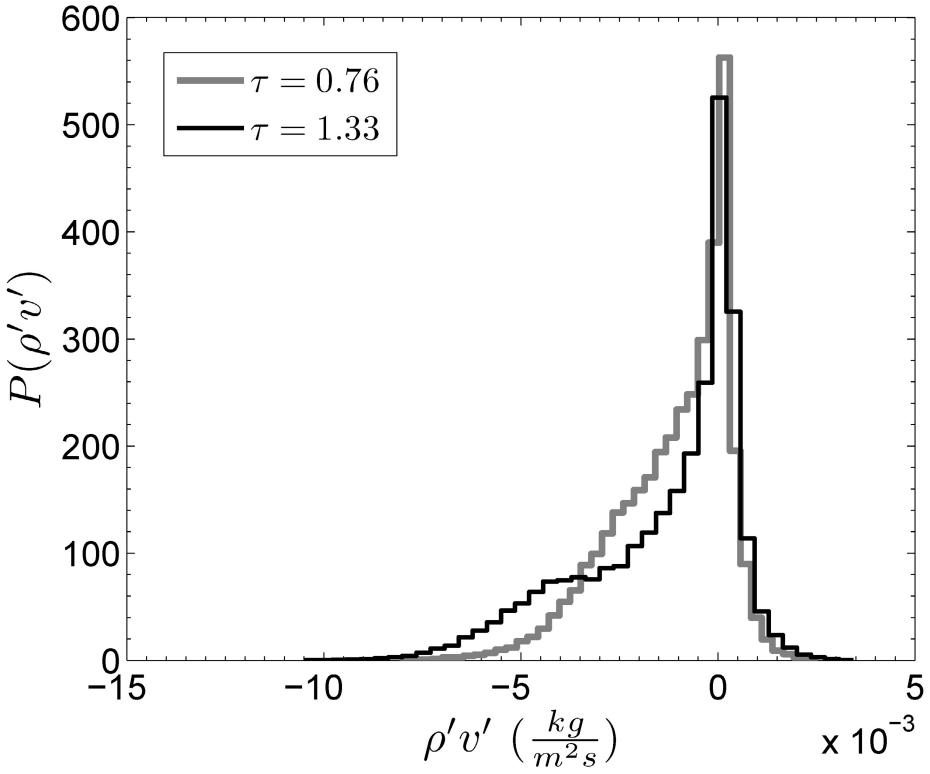

Figure 4.7. The *p.d.f.* of $\rho' v'$ at the centerline of the mixing layer for two non-dimensional times.

spikes. When scaled by an appropriate velocity scale, as shown in Figure 4.6 (a), the turbulent mass flux becomes approximately self-similar at late-time. This transition to self-similarity appears in conjunction with the self-similar behavior of the measured growth parameter and molecular mixing parameter at late-time, between $\tau = 1.2 - 1.5$. The cross-correlation $\overline{\rho' v'}$ can also be examined as a non-dimensional correlation coefficient as shown in Figure 4.6 (b). The $R_{\rho' v'} = \overline{\rho' v'} \Big/ \left(\sqrt{\overline{\rho'^2}} \sqrt{\overline{v'^2}} \right)$ coefficient shows an approximately constant negative correlation between the density and vertical velocity fluctuations as the bubbles and spikes dominate the growth of the mixing layer. The measured $R_{\rho' v'}$ coefficients (mean value of -0.74) compares well with the value of -0.76 obtained through large-eddy simulation by Cook *et al.* (2004). Ristorcelli and Clark (2004) have evaluated a velocity-scalar correlation coefficient and found a large negative correlation of -0.82 at late-time at the mixing layer centerline. For the first time we report an experimental measurement of the *p.d.f.* for $\rho' v'$ inside the Rayleigh-Taylor mixing layer as shown in Figure 4.7. In homogeneous turbulence, such as grid turbulence, Mydlarski (2003) observed an approximately joint-normal distribution, contrasting sharply with the non-Gaussian distribution found in Figure 4.7. Rather, similar to free shear flows, where a bell-shaped distribution (non-Gaussian) is expected (Pope 2000), a significant deviation from Gaussian behavior was found. The $\rho' v'$ *p.d.f.* at the mixing layer centerline for τ =1.33 has a large kurtosis, $K_{\rho' v'}$ = 10.6, and skewness, $S_{\rho' v'}$ = -3.8 (K = 3 , S = 0 for Gaussian). A large peak is found about 0 where small density fluctuations, corresponding to molecularly mixed fluid, result in weak correlations of the velocity and density fluctuations. However, when comparing early and late-time *p.d.f* 's larger negative magnitudes of the turbulent mass flux become more likely as the mixing layer continues to grow. Fluid is entrained into the mixing layer at a faster

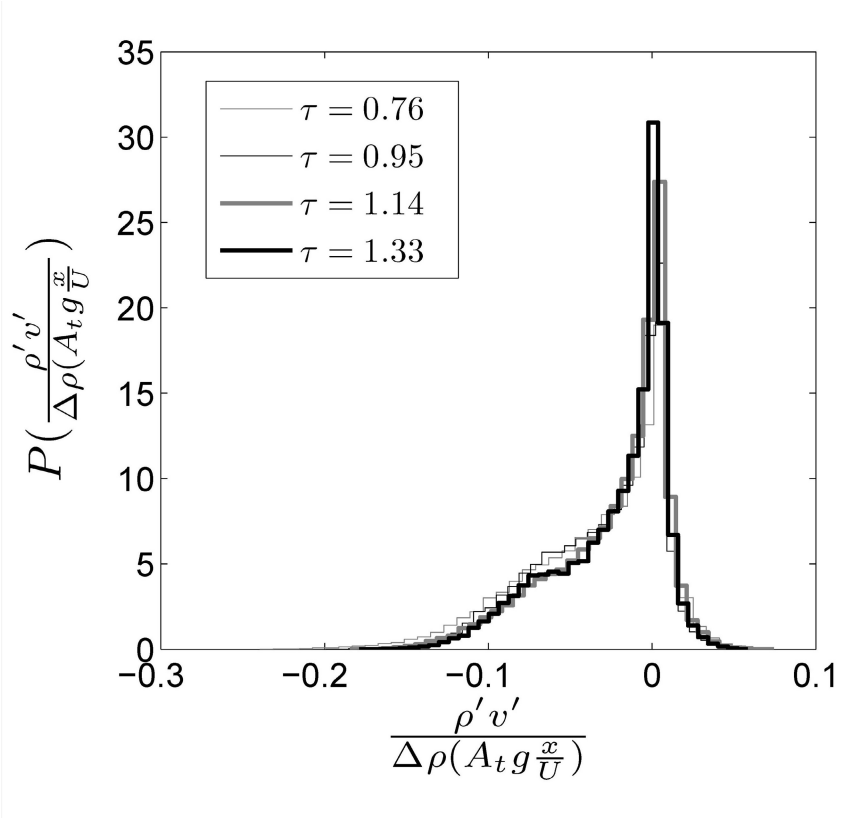

Figure 4.8. The collapse of the $\rho' v'$ *p.d.f.* when non-dimensionalized from intermediate to late time.

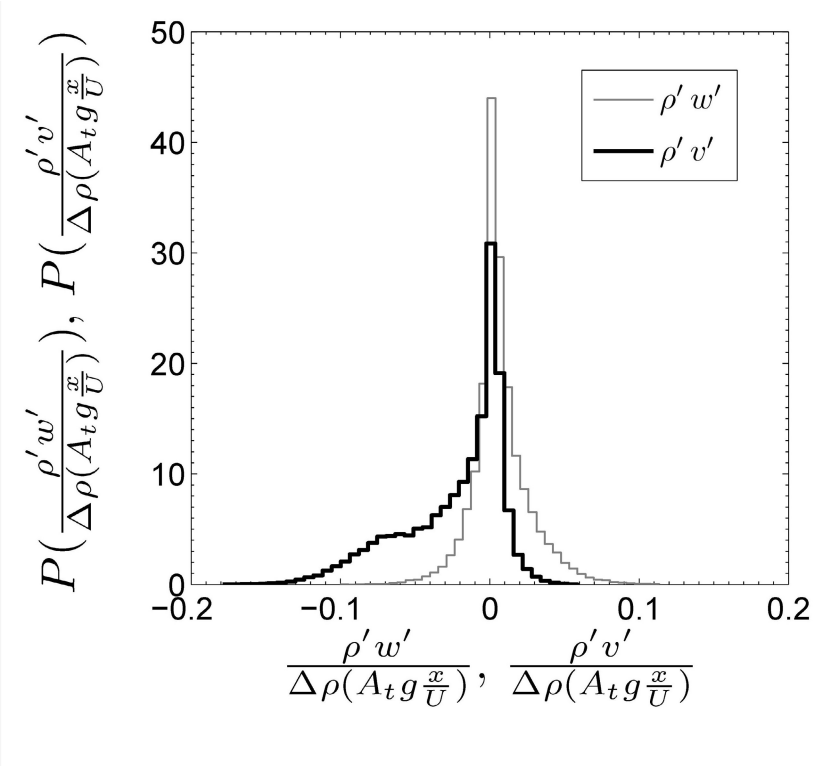

Figure 4.9. Comparison of the $\rho' v'$ and $\rho' w'$ *p.d.f.* at $\tau = 1.33$.

rate, and the mixing layer becomes more turbulent, resulting in large magnitudes of the turbulent mass flux as fluid is transported across the mixing layer. Figure 4.8 demonstrates a collapse of the vertical turbulent mass flux *p.d.f.* at different times of evolution at the mixing layer centerline using the non-dimensionalization of Figure 4.6.

Due to the vertical acceleration imposed by gravity, the primary turbulent mass flux for Rayleigh-Taylor mixing layers is $\overline{\rho' v'}$, and the horizontal turbulent mass fluxes $\overline{\rho' u'}$ and $\overline{\rho' w'}$ are close to zero due to symmetry of the plumes (Banerjee 2006; Ristorcelli & Clark 2004). Indeed, the differences in the vertical and horizontal turbulent mass fluxes can also be observed through the measured *p.d.f.* of $\rho' v'$ and $\rho' w'$ shown in Figure 4.9. The distribution of $\rho' w'$ is centered and approximately symmetric about zero, which contrasts sharply with the *p.d.f.* of $\rho' v'$. The symmetric behavior of $\rho' w'$ results in the negligible net contribution of the horizontal mass flux, due to symmetry of the mushroomed shaped plumes. This is in contrast with the vertical direction, where mass is transported across the mixing layer through the rising and falling bubbles and spikes. These differences highlight the uniqueness of buoyancy-driven turbulence and the importance of the vertical turbulent mass flux in RT mixing layers.

Production of turbulent kinetic energy peaks at the center of the mixing layer, resulting in large negative turbulent mass fluxes, $\overline{\rho' v'}$ (Ristorcelli & Clark 2004). However, the magnitude of $\overline{\rho' v'}$ decreases towards the edge of the mixing layer, corresponding to a decrease in the production of turbulent kinetic energy. The smaller vertical turbulent mass flux away from the mixing layer centerline is also evident in the measured *p.d.f.* of $\rho' v'$. The measured $\rho' v'$ *p.d.f.* at the mixing layer centerline ($\overline{f}_{v,1}$ = 0.51) and average volume fractions of fluid 1 of 0.65 and 0.77 are compared in Figure 4.10. Moving towards the top edge of the mixing layer, where the average volume fraction of fluid 1 increases, the large negative turbulent mass fluxes

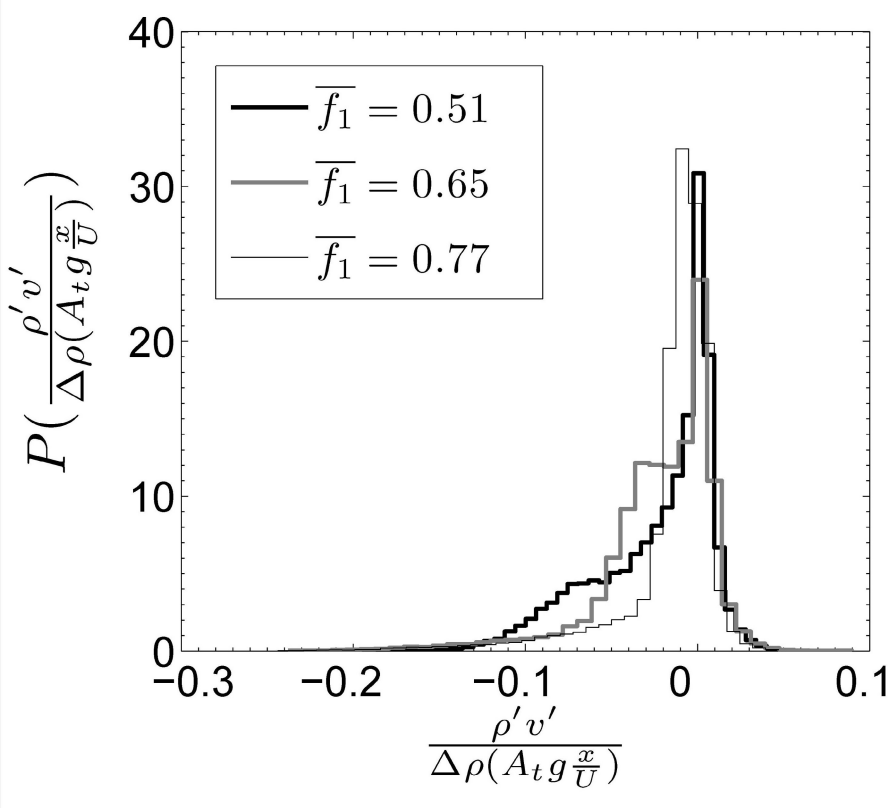

Figure 4.10. The *p.d.f* of $\rho'v'$ at τ = 1.33 at the mixing layer centerline ($\overline{f}_{v,1}$ = 0.51) and two locations above the mixing layer centerline. The properties of the these distributions are determined for $\overline{f}_{v,1}$ = 0.51 where $\overline{\rho'v'}/(\Delta\rho A_t gx/U) = -0.026$, $K_{v'}$ = 10.6, $S_{v'}$ = -3.8;
$\overline{f}_{v,1}$ = 0.65 where $\overline{\rho'v'}/(\Delta\rho A_t gx/U) = -0.025$, $K_{v'}$ = 18.2, $S_{v'}$ = -4.7; and for
$\overline{f}_{v,1}$ = 0.77 where $\overline{\rho'v'}/(\Delta\rho A_t gx/U) = -0.019$, $K_{v'}$ = 24.6, $S_{v'}$ = -5.2.

decrease in likelihood. However, large negative magnitudes of the vertical turbulent mass flux are present to a lesser extent due to the rising bubbles, which have transported fluid 2 across the entirety of the mixing layer. Above the mixing layer centerline, the developing spikes, not yet fully turbulent, are more prominent, thus resulting in a decrease in the vertical turbulent mass flux. The $\rho' v'$ distribution at the edge of the mixing layer more closely resembles the *p.d.f.* of the horizontal turbulent mass flux shown earlier, where there is negligible turbulent mass flux. Therefore, the observed asymmetric distribution of the vertical turbulent mass flux corresponds to large negative magnitudes of $\overline{\rho' v'}$ and the production of turbulent kinetic energy within the buoyancy-driven mixing layer.

4.4 Measurement of energy density spectra

Finally, the measured energy density spectra for v' , ρ' and $\rho' v'$ at the centerline of the mixing layer using the S3WCA technique is shown in Figure 4.11. The energy density spectra are shown for early and late-time corresponding to τ = 0.76 (Re_h = 750) and τ = 1.33 (Re_h = 1450), where $Re_h = \left(\sqrt{gA_t/6}\right)(2h)^{3/2}/\upsilon_{mix}$ (Snider & Andrews 1994). Fiducials corresponding to $k^{-5/3}$ and k^{-3} are also shown in Figure 4.11, which correspond to the spectral slopes of the two-dimensional Kolmogorov spectrum for the inertial and dissipation subranges of length scales for high *Re* turbulent flows, respectively. Single point hot-wire measurements result in a one-dimensional spectrum, however the Kolmogorov spectrum can still be used as reference. At early-time the mixing layer is transitioning to turbulence and an inertial subrange of scales, which transfers energy from the large energy containing length scales to the small viscosity dominated scales responsible for dissipation, is not found. However at τ = 1.33 the mixing layer becomes turbulent and loses its two-dimensional nature from the initial conditions

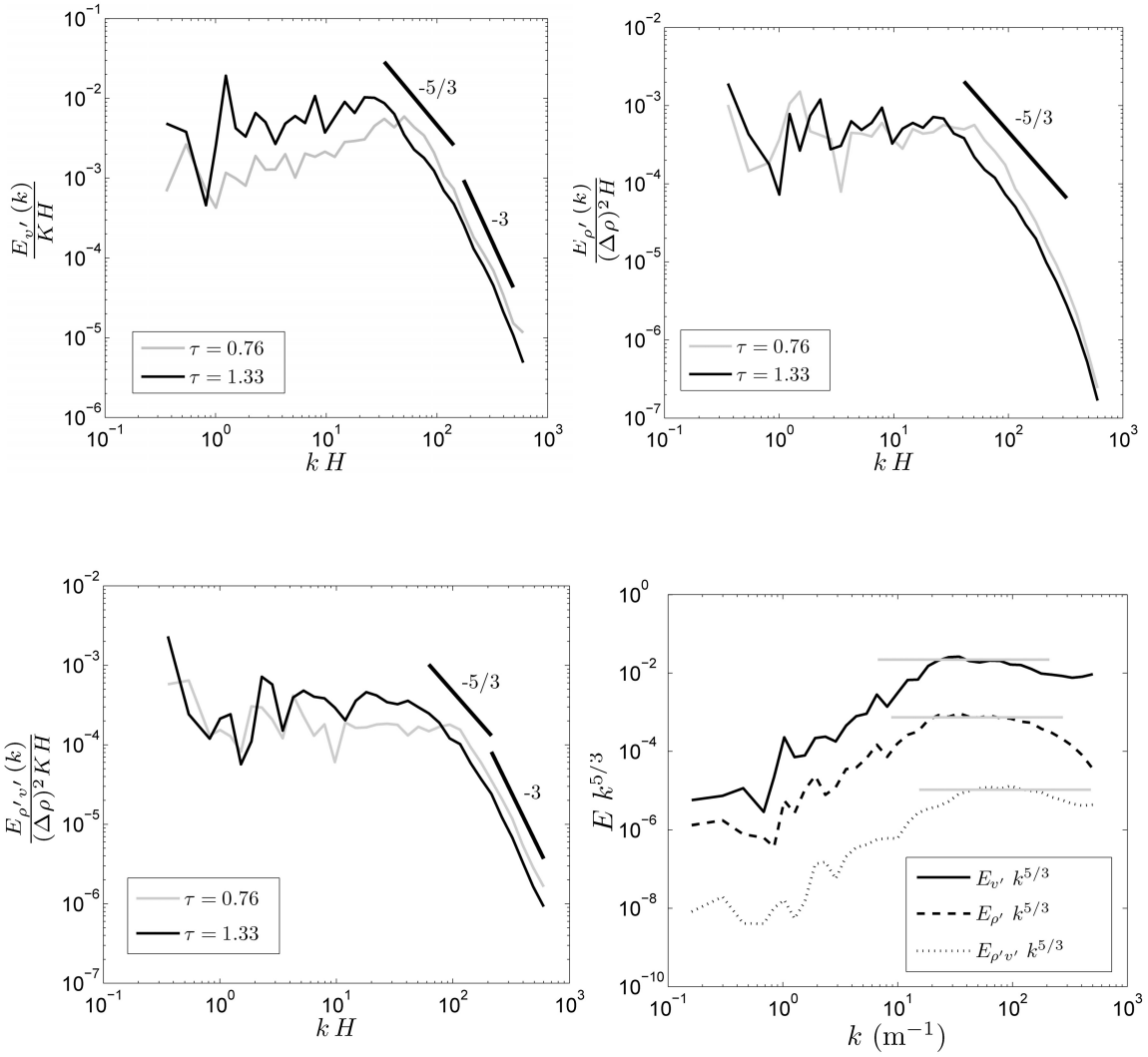

Figure 4.11. The measured energy density spectra for v' , ρ' and $\rho' v'$ at the centerline of the mixing layer using the S3WCA technique. Compensated spectra demonstrating the -5/3 slope as a flat line is also shown at $\tau = 1.33$ for each energy density spectra. The spectra are normalized by $\Delta\rho$, K, and H.

and develops three-dimensional structure as described previously in the PLIF images of Figure 1.3. The energy cascade from large to small length scales results in an observable inertial subrange of scales in the v' and ρ' fluctuations, as shown by the compensated energy density spectrum, $E\ k^{-5/3}$, in Figure 4.11. Compensated energy density spectra demonstrate the $k^{-5/3}$ behavior as a flat region in the spectra which allows the inertial subrange of scales to be identified. The observation of inertial scales at Re_h of 1400 and $\tau = 1.33$ is consistent with previous measurements in the water channel by Ramaprabhu and Andrews (2004) and Mueschke *et al*. (2006). From the $\rho'v'$ energy density spectra also shown in Figure 4.11, it is evident that fluctuations in the turbulent mass flux are contained mostly in the large scales of the developing turbulence. This corresponds to large scale bubbles and spikes of interpenetrating fluid that expand the mixing layer as it develops. As the mixing layer grows, the integral scales increase as larger quantities of fluid are entrained into the edges of the mixing layer, giving an increase in the fluctuations of the turbulent mass flux for large scales of the turbulence. It is unclear in the $\rho'v'$ energy density spectra, however, what power law decay is observed and no previous measurements have been found in the literature for RT driven turbulence. For low Reynolds number turbulent flows, such as decaying grid turbulence with passive scalars (Mydlarski 2003), the co-spectrum for velocity and passive scalars was found to closely follow the behavior of the velocity field (although this is not buoyancy-driven). There also appears to be a strong correlation between the $\rho'v'$ energy density spectra and the v' spectrum measured here. Therefore, the $k^{-5/3}$ and k^{-3} lines are added as a reference. However, the mixing layer does not have a sufficient range of scales to make a definitive assessment of the spectral behavior. To better determine the spectral distribution of energy in turbulent fluctuations, higher Reynolds number (larger range of scales) are required. Similarities between the distribution of energy

in v' and $\rho' v'$ are more clearly seen in the compensated energy density spectra of Figure 4.11, as both compensated spectra show similar distributions of energy throughout the range of length scales measured.

5. RAYLEIGH-TAYLOR MIXING AT LARGE ATWOOD NUMBER

The new S3WCA diagnostic has been developed to meet the specific need for simultaneous and instantaneous measurements of turbulent velocity and density fluctuations in Rayleigh-Taylor mixing layers. The diagnostic has been validated at a small Atwood number, $A_t = 0.03$, and new instantaneous measurements of $\overline{\rho' v'}$ obtained experimentally for the first time have been presented. However, another primary objective of this work was to use the new measurement capabilities to characterize the developing fluid turbulence and to improve the understanding of the turbulent physics at large Atwood number, specifically $A_t = 0.6$.

The existing experimental facility, validated for $A_t \leq 0.47$, has been modified to meet the demands of performing experiments at larger Atwood numbers. Requirements for performing larger A_t experiments include operating the facility at larger advection velocities, to counteract the faster growth of the mixing layer width. Larger advection velocities were necessary to maintain the parabolic nature of the flow (Snider & Andrews 1994). Additional modifications to the exit flows of the facility were made to provide improved control of the outflows and to prevent backflows of heavy fluid. This becomes more challenging with the larger density gradients in the current experiments. The specific modifications were as follows.

1) Fabricated a third helium metering line to be used in parallel with the existing two lines (22 K-type helium bottles total). This increased the available helium flow rates for large Atwood experiments up to 0.23 lb/s.
2) Added a second, identical *Dayton* 1 ½ HP industrial blower to the air-side of the inlet plenum, to be used in parallel with the existing industrial blower. This increased the available air flow rates for the air (top) stream of the facility, which allows a channel velocity of 2.0 m/s.

3) Extended the exit center-plate 55 cm into the test section of the facility to provide exit control closer to the region of the mixing layer of interest, and to stop the penetration of heavier air into the bottom half of the facility where backflows of heavier air are likely to occur. This ensured that the average densities of the fluids in the top and bottom exits are closer to their respective inlet streams.

Images of an A_t = 0.6 experiment performed at an advection velocity of 2 m/s are shown in Figure 5.1. The A_t = 0.6 experiment was designed so that the predicted growth would result in a local spread angle (the angle the downstream spike tips form at the edge the mixing layer) of ~ 20º at the location of the exit center-plate 1.45 m downstream. This ensured that the mixing layer preceding the exit plate satisfies the parabolic requirement of 15º (Snider & Andrews 1994) while attaining late-time behavior up to $\tau \sim 1.5$. Nine cartridges of S105 green smoke from *Regan HVAC Products* were used to mark the top (air) stream for visualization of the mixing layer. As expected from the previous experiments by Banerjee (2006) and the LEM experiments of Dimonte and Schneider, an asymmetry was observed between the bubble (top) and spike (bottom) halves of the mixing layer. As described by Dimonte and Schneider, the lower resistance of the bottom fluid (helium/air) results in narrower, faster growing spikes that form as the top fluid (heavier air) falls through the mixing layer. This was particularly evident in the immiscible LEM experiments of Dimonte and Schneider (2000) and also in the immiscible drop tank experiments of Read (1984) with an $A_t > 0.8$ where at late-time $h_s / h_b > 2$. The asymmetry can also be observed to a lesser extent in the image of Figure 5.1 (a) for A_t = 0.6. In the right half of the image, the spikes (falling dark plumes) are clearly narrower and penetrating faster than the rising bubbles (light colored plumes). Also, when viewing the extent of the

(a)

(b)

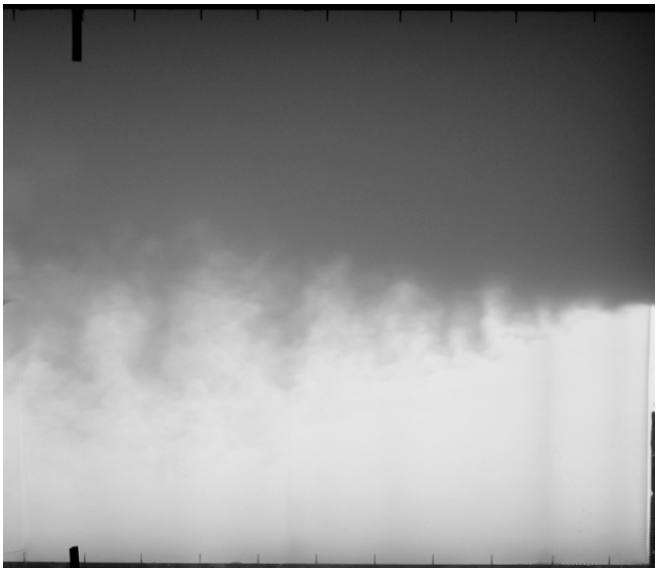

Figure 5.1. Digital image of a buoyancy-driven mixing layer for A_t = 0.6 with U_m = 2.0 m/s. The flow is from right to left with the top (heavier, air) stream marked with smoke. The distance from the right edge of the image to the black marks is 1.25 m.

mixing layer heights in both images of Figure 5.1 a clear asymmetry is observed between the larger penetration of the spikes into the bottom half of the mixing layer and the smaller penetration of the bubbles into the top half of the mixing layer.

Using an image analysis technique described by Snider and Andrews (1994) and Banerjee and Andrews (2006), the asymmetry of the mixing layer was quantitatively measured. Relying on a linear absorption of light by the smoke particles (behaving much like a dye with a linear absorption of light as described in Section 2.2), measured light intensities through digital photographs were related to fluid concentration or volume fractions of fluid 1 and 2 (top and bottom fluids). The mixing layer widths were determined in the same manner as Banerjee and Andrews (2006) and the A_t =0.47 experiment of Banerjee, Kraft and Andrews (2007). The bubble heights correspond to the mixing layer width, h_b, and the spike widths correspond to the mixing layer width, h_s. These were measured as the difference in widths between the $f_{v,1}$ = 0.95 and $f_{v,1}$ = 0.5 locations and the $f_{v,1}$ = 0.5 and $f_{v,1}$ = 0.05 locations, respectively. Figure 5.2 (a) shows these measured volume fractions overlaid onto the average of 100 images obtained during the ~ 100 second duration of the experiment. A median filter similar to those used by Snider and Andrews (1994) and Banerjee and Andrews (2006) was used to remove noise from the image and measured volume fractions. Asymmetry of the mixing layer was more apparent from the image of Figure 5.2 (a) and was additionally seen in the volume fraction profile across the height of the mixing layer, as shown in Figure 5.2 (b). The volume fraction profile is shown for two downstream locations of x = 0.5 m and x = 1.25 m. The original interface location corresponds to the position y = 0, which was centered vertically in the experimental facility. It was also evident from the volume fraction profiles and the plotted volume fraction contours of Figure 5.2 (a) that the location of $f_{v,1}$ = 0.5 shifted slightly from the original interface location

(a)

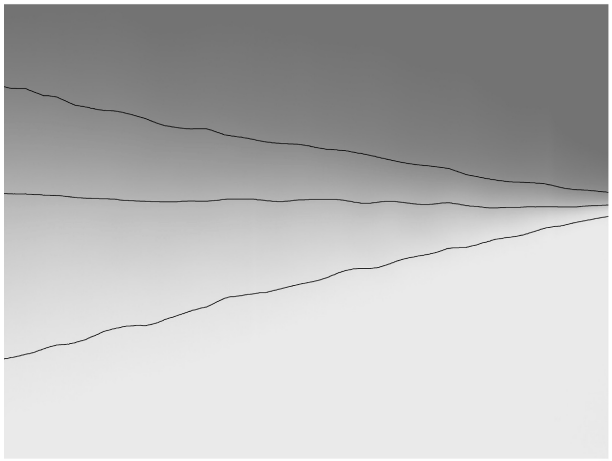

(b)

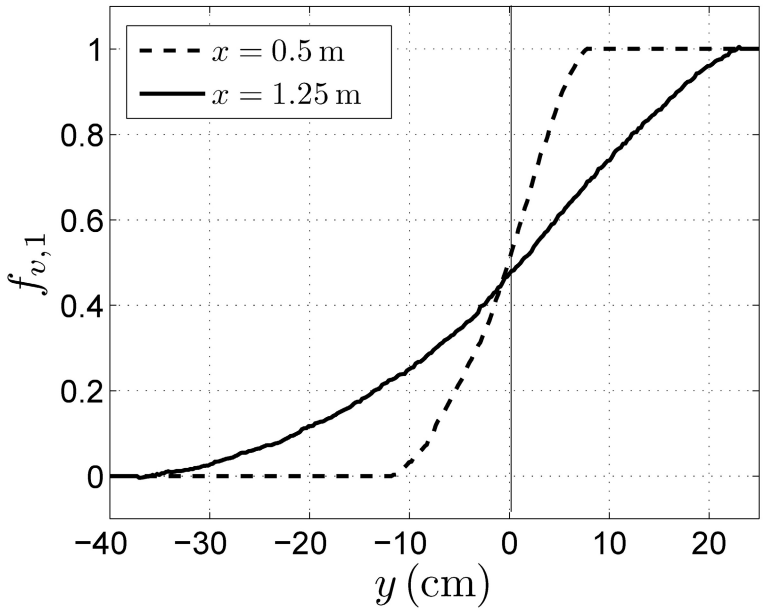

Figure 5.2. (a) An average image of a buoyancy-driven mixing layer for A_t = 0.6 with U_m = 2.0 m/s. The flow is from right to left with the top (heavier, air) stream marked with smoke. Volume fraction contours are shown corresponding to $f_{v,1}$ = 0.95, $f_{v,1}$ = 0.5, and $f_{v,1}$ = 0.05 from top to bottom. (b) Volume fraction profiles across the mixing layer at two downstream locations.

of $y = 0$, rising into the top half of the RT mixing layer. Far downstream at $x = 1.25$ m the deviation of $f_{v,1} = 0.5$ from the original interface location was ~ 1.5 cm or ~ 3% of the total mixing layer width. This behavior was also observed by Banerjee *et al.* (2008) for $A_t = 0.47$. Movement of the $f_{v,1} = 0.5$ location into the rising, bubble side of the mixing layer has also been shown through the large Atwood number simulations of Youngs (1989, 1991) for $A_t = 0.5$ and 0.9, where the displacement of the $f_{v,1} = 0.5$ location from the original interface location ($y = 0$) increases with A_t. In contrast with low Atwood number ($A_t < 0.1$), where an approximately linear volume fraction (density) profile is expected (Snider & Andrews 1994; Banerjee & Andrews 2006), at an $A_t = 0.6$ the volume fraction profile deviates from linearity at the bottom edge of the mixing layer. This deviation from linearity occurs primarily at $f_{v,1} < 0.2$ for the volume fraction profile shown and corresponds to the penetration of the falling spikes. The volume fraction approaches its lower bound of zero slowly when compared to the behavior at the upper bound of one. This indicates a larger mixing layer width, h_s, for the spike half of the mixing layer when compared with the bubble side. Interestingly, although numerical simulations of large Atwood number RT mixing layers show a similar movement of the $f_{v,1} = 0.5$ location from the original interface location, the asymmetrical behavior of the volume fractions at the bottom edge of the mixing layer described experimentally in the current work and also by Banerjee *et al.* (2008) are not as prominent in numerical simulations. This is particularly evident in the direct numerical simulations of Cook and Dimotakis (2001) for $A_t = 0.5$, where visualization of the RT mixing layer and determination of volume fraction profiles demonstrated a more symmetrical behavior, consistent with smaller A_t. These differences highlight the challenges in comparing and validating RT experiments and numerical simulations in these complex variable density flows.

(a)

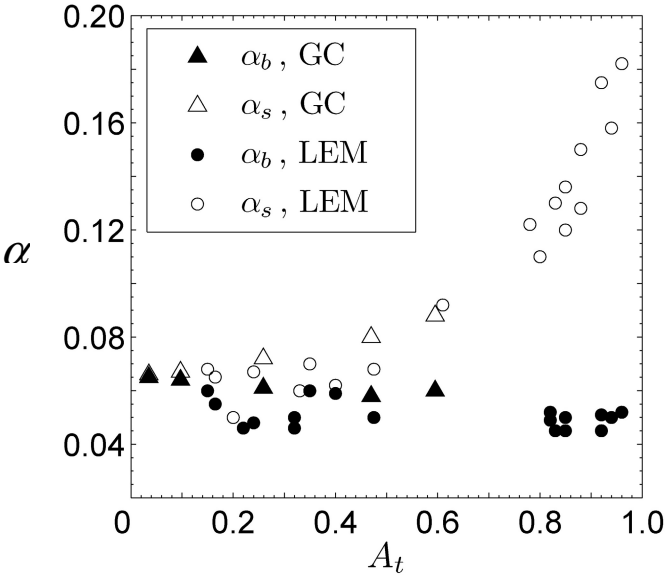

(b)

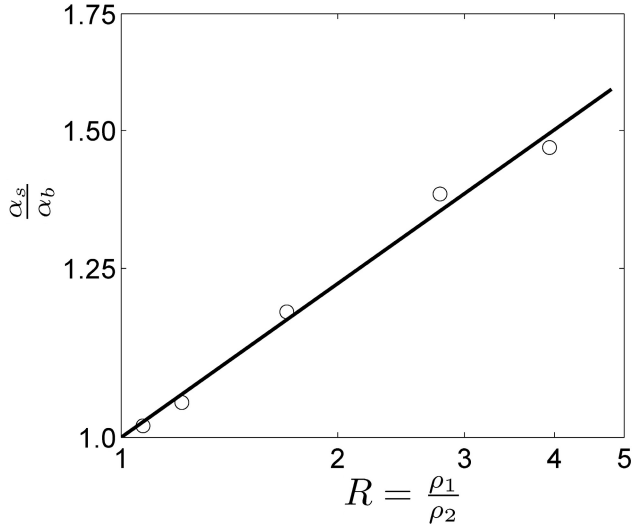

Figure 5.3. (a) Measured growth parameter from the gas channel (GC) for all measured A_t up to A_t = 0.6. This includes previous measurements by Banerjee (2006) and Banerjee *et al.* (2008) for $A_t \leq 0.47$. For comparison, the immiscible experimental measurements (LEM) of Dimonte and Schneider (2000) are also shown. (b) α_s is re-plotted to demonstrate the power law relationship of (1.4).

To eliminate the possibility that uneven exit flows could cause the entirety of the mixing layer to rise, resulting in an artificial rise of the $f_{v,1} = 0.5$ location, a simple check of the experiment was performed. The volume flux of each stream as it entered and exited the test section must be conserved for the incompressible RT mixing layer. Therefore, the volumetric flow rates (and subsequently the channel velocity for each stream) must be equal as the top and bottom streams separately enter and are again divided as they exit. This is a simple, although crude method for checking the exit flows for any inconsistencies which could affect the mixing layer growth. During the experiment, the mixing layer and the exit flows (which can be imaged because the exit center-plate was extended into the viewable test section) were recorded using a digital video camera at thirty fps. By timing the movement of smoke-marked structures through the top and bottom exits with the captured frames of the digital video, the velocity of the exit streams were checked throughout the experiment.

Using the measured mixing layer widths h_b and h_s, the growth parameters of the bubble and spike sides of the mixing layer were also determined through the quadratic relation in (1.3). The growth parameters were measured from a linear fit of the self-similar region for $h_{b,s}$ *vs.* $A_t g t^2$. The slope of the fitted line is the growth parameter, α_b or α_s. This method is robust since the linear fit is not affected by noise in the measured mixing layer widths. Another method which was demonstrated by Banerjee (2006) at $A_t = 0.035$ utilized the relation $dh/d(A_t g t^2)$ over a moving window. However, for larger Atwood numbers this method proved unreliable due to noise in the measured mixing widths. From a linear fit of the self-similar region for h *vs.* $A_t g t^2$, the measured growth parameters for $A_t = 0.6$ are $\alpha_b = 0.060 \pm 0.004$ and $\alpha_s = 0.088 \pm 0.006$ The ratio h_s / h_b at late-time reaches a value of 1.55. These measurements are consistent with those obtained by Banerjee (2006) for $A_t = 0.47$, where $\alpha_b = 0.059$, $\alpha_s = 0.081$, and $h_s / h_b = 1.5$.

The measured growth parameters from Banerjee (2006), Banerjee *et al.* (2008), and the current work are shown in Figure 5.3 (a). The plotted growth parameters were measured for $0.04 \leq A_t \leq 0.6$, and were all obtained in the gas channel facility using mixtures of helium and air. Additional immiscible measurements from Dimonte and Schneider (2000) using the linear electric motor (LEM) experiment are also shown for $0.15 \leq A_t \leq 0.96$. Although the measured bubble growth parameters from the gas channel are comparably larger (~18%), possibly due to the effect of the different initial conditions, both the gas channel and the LEM experiments show a similar A_t dependence for the measured growth parameters. As A_t increases, α_s increases as the asymmetry between the top and bottom sides of the mixing layer becomes significant at large Atwood numbers. At A_t = 0.6, α_s has increased by 30% over the lower Atwood number experiments. From the gas channel results summarized in Figure 5.3 (a), there may be a weak A_t dependence for α_b, as the measured growth parameters decrease for increasing A_t, resulting in a 10% decrease in the growth constant by an A_t = 0.6. However, it is difficult to know if this is an actual trend, as the uncertainty of determining the growth parameters is ~ 10 %. In the large Atwood number experiments of Read (1984), the asymmetric growth of the mixing layer was also observed, but only α_b was determined due to limitations in the diagnostics. Read (1984) found for the Atwood numbers investigated ($A_t \geq 0.5$) that α_b was consistent with an average value of 0.06. This agrees well with the current A_t = 0.6 measurement. As shown by Dimonte and Schneider, it is possible to describe the A_t dependence of α_s using a power law $\alpha_s / \alpha_b = R^{D_\alpha}$, where $R = \rho_1 / \rho_2$. The power law exponent was determined from the best fit of the measured growth parameters, and was found to be 0.29 for the range of A_t investigated in the gas channel to this point. However this is only an empirically defined relationship. A plot of the measured growth parameters and the power law fit are shown in Figure 5.3 (b). The measured exponent is similar to D_α = 0.33 measured by Dimonte and Schneider. Direct comparison

between the current helium/air experiments and those of Dimonte and Schneider are complicated by the use of immiscible liquid/gas combinations and the resulting surface tension effects present in the LEM experiments.

The current results obtained from the gas channel differ in definition from Dimonte and Schneider, who measured their bubble and spike widths relative to the original interface location rather than the location where $f_{v,1} = 0.5$. For the Atwood number range investigated in this study, the deviation of the original interface location was found to be small even at late-time, where a maximum deviation of ~ 3% of the total mixing layer width was found. However, this may be a more significant issue as experiments with $A_t > 0.8$ are performed, as the movement of the $f_{v,1} = 0.5$ location into the top (bubble) half of the mixing layer is pronounced (Youngs 1991; Dimonte & Schneider 2000).

For the first time, experimental measurements of velocity and density fluctuations have been obtained in a Rayleigh-Taylor mixing layer at large Atwood number. Unlike the MPMO hot-wire diagnostic used by Banerjee (2006), the new S3WCA diagnostic can be used at $A_t > 0.25$. The unique capability of the S3WCA diagnostic allows for measurements of v'_{rms}, w'_{rms}, $\overline{\rho'^2}$, $\overline{\rho' v'}$ at $A_t = 0.6$ using a temperature difference of $T_1 - T_2 \sim 5$ °C to mark the two inlet streams. Special considerations have been made to use the diagnostic in the large concentrations of helium, $f_{v,he} \leq 0.88$, found in the $A_t = 0.6$ mixing layers. In particular, to increase the likelihood that both the cold-wire and hot-wire sensors measure the same fluid structure, the raw data was filtered to four times the spatial resolution of the combined probes ($freq_{max} = 83$ Hz). Furthermore, solutions from the simplified Bruun (1995) analysis, which reduce the hot-wire voltages into components of velocity, was re-checked using a Newton-Raphson solver for the non-linear form of the response equations. Solutions which did not meet convergence for the non-linear form of the equations were removed when determining statistics.

The hot-wire analysis and discrimination procedure is described in Appendix D. This procedure was necessary to limit errors that can occur when the cold-wire and hot-wire probes did not sense the same fluid at large Atwood numbers.

Even with filtering of the raw data, it was found that measurements of $\overline{u'^2}$ (velocity fluctuations in the stream-wise direction) were larger than expected (comparable to $\overline{v'^2}$*)* due to the physical spatial resolution of the probes, combined with the large concentrations of helium present in the mixing layer (hot-wire voltage sensitivities to helium become significant in large concentration of helium). This was expected as the mixing layer is a channel flow dominated by the *U*-component of velocity; therefore, the *U*-component of velocity is most sensitive to errors introduced by the large range of helium concentrations in the flow. Measurements of $\overline{v'^2}$ and $\overline{w'^2}$ however are believed to be acceptable as they are also dependent on the orientation of the orthogonal sensors rather than only on the dynamics of the helium mixture passing the probes. However, as the average helium concentration sensed by the probes is increased above the current centerline concentration of $f_{v,he} = 0.44$, measurements of $\overline{v'^2}$ and $\overline{w'^2}$ will likely also be affected as the hot-wire voltage sensitivities to helium increase significantly above these concentrations (Banerjee & Andrews 2007). Therefore, $A_t = 0.6$ measurements of $\overline{v'^2}$, $\overline{w'^2}$, θ, $\overline{\rho' v'}$ will be reported at $x = 0.40$, 0.60, and 0.70 m ($\tau = 0.44$, 0.66, and 0.78) with $U_m = 2.0$ m/s at the mixing layer centerline (initial interface location $y = 0$). A table of the complete data set is included in Appendix H.

The present measurements were limited to $\tau = 0.78$ and $\mathrm{Re}_{v'} = (h_b + h_s) v'_{rms} / \upsilon_{mix} = 4500$ due to excessive turbulence levels ($v'/U > 25\%$) beyond this time of evolution. The obvious

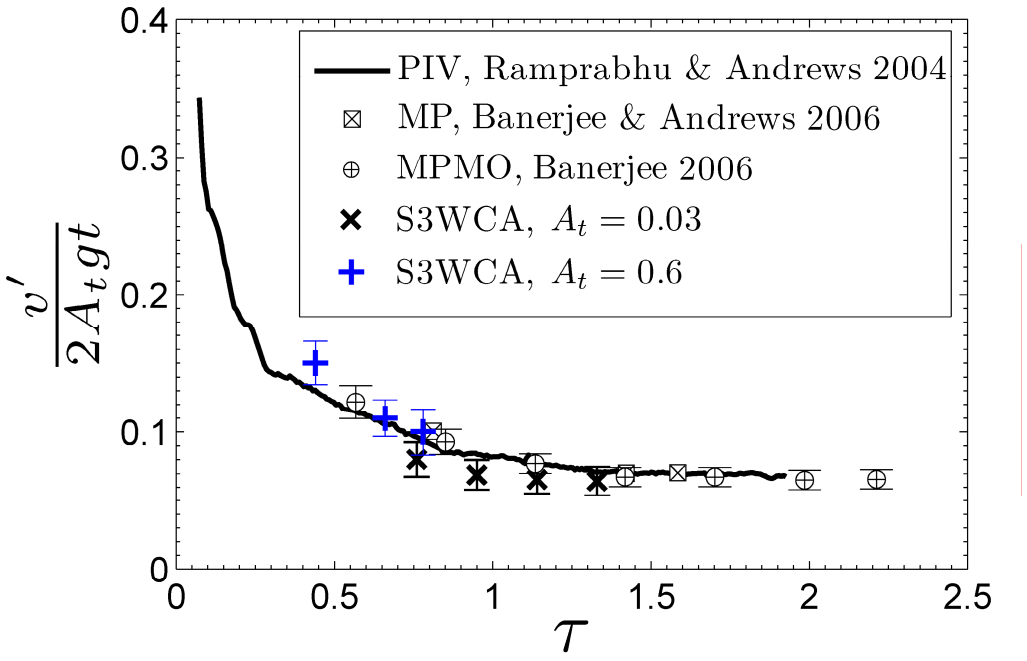

Figure 5.4. Non-dimensional *rms* vertical velocity fluctuations at the mixing layer centerline ($y = 0$) for $A_t = 0.6$ and $U_m = 2.0$ m/s compared with low A_t measurements from the water and gas channel facilities.

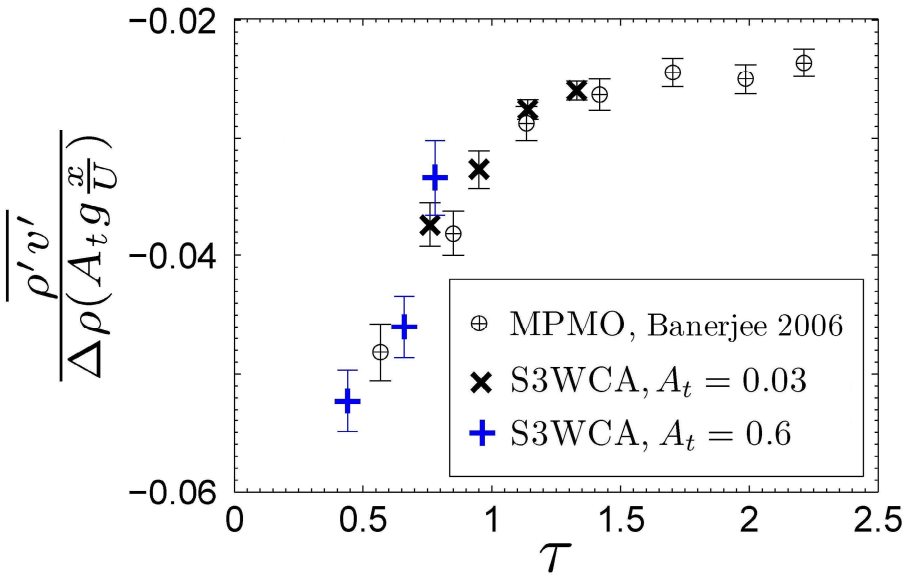

Figure 5.5. Non-dimensional vertical turbulent mass flux at the mixing layer centerline for A_t = 0.6 and U_m = 2.0 m/s compared with low A_t measurements in the water and gas channel facilities.

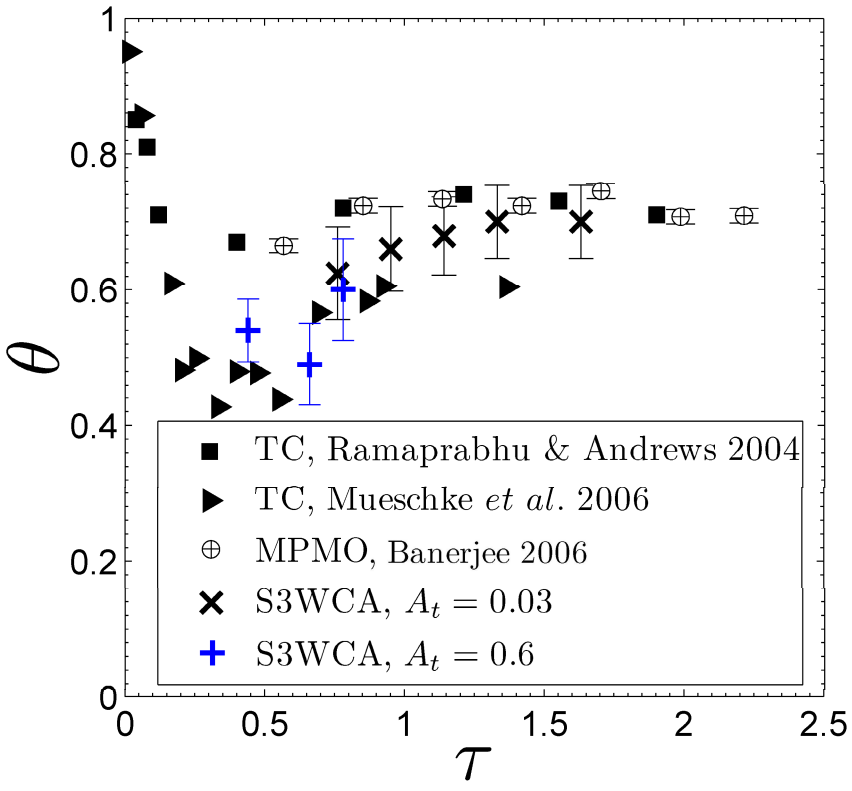

Figure 5.6. Molecular mixing parameter, θ, at the mixing layer centerline for A_t = 0.6 and U_m = 2.0 m/s compared with low A_t measurements in the water and gas channel facilities.

solution to obtain measurements further downstream is to increase the advection velocity of the channel, U_m. This would decrease the turbulence level to acceptable levels at larger times (downstream distance) of evolution. With the physical space constraints of the current experiment, and because the volumetric flow rates for the helium and air cannot be increased within the facility in its current configuration, these high velocity experiments are future research. In addition, larger advection velocities would require a longer experimental facility ($t = x/U$) than currently available. Proposed design parameters and modifications for a new experimental facility to attain late-time measurements at large Atwood numbers are described in further detail in Section 7.

Non-dimensionalized measurements of the *rms* vertical velocity fluctuations at the mixing layer centerline at $A_t = 0.6$ are compared with low Atwood measurements in the water and gas channel facilities in Figure 5.4. Up to a measured time of $\tau = 0.78$ the vertical velocity fluctuations show a striking similarity to those measured at much lower Atwood numbers, $A_t \leq 0.04$. A similar result is found in Figure 5.5 when comparing measurements of the primary turbulent mass flux, $\overline{\rho' v'}$, at $A_t = 0.6$ with those at lower A_t. Again, centerline measurements ($y = 0$) agree well with those obtained at much lower Atwood number. This trend continues when examining the molecular mixing parameter, θ, determined from $\overline{\rho'^2}$. Figure 5.6 shows a comparison of θ at $A_t = 0.6$ with lower Atwood results obtained in the water and gas channels. Since the cold-wire anemometer and subsequent measurements of density can be analyzed independently of the hot-wire diagnostic, the cold-wire data was re-analyzed at its Nyquist limit of 666 Hz at $U_m = 2.0$ m/s to include the maximum range of scales possible in the measurement of θ. Again the $A_t = 0.6$ measurement is consistent with those at much lower A_t, demonstrating a

significant decrease in the amount of molecular mixing at early time in the developing buoyancy-driven mixing layer.

In Figure 5.6 a decrease in θ can be observed at early time for the mixing layer of helium and air; however, the decrease was not as extensive as that shown by Mueschke *et al*. (2006) in the water channel. Using an improved thermocouple diagnostic with increased frequency response and reduced spatial resolution, Mueschke *et al.* (2006) obtained more accurate measurements of molecular mixing than previously obtained by Ramaprabhu and Andrews (2004) in the water channel. Mueschke *et al.* (2006) found a minimum amount of molecular mixing at an early time of θ = 0.36. Using a similar cold-wire diagnostic and temperature marker in the current work, a minimum of θ = 0.46 is found. In addition, when considering the combined data from the current work and Banerjee (2006) for mixing layers of helium and air ($Sc \sim 1$), larger magnitudes of molecular mixing are found overall when compared with the water channel results of Mueschke *et al*. (2006) with $Pr \sim 7$. Mixing layers associated with higher *Sc* (or *Pr* in the water channel experiments) show a reduced amount of molecular mixing due to lower rates of molecular diffusion (whether mass or temperature diffusion). The work by Mueschke *et al.* (2006) has been continued using a reacting RT flow to determine the effect of molecular diffusivities on the dynamics of turbulent mixing in RT mixing layers (Mueschke *et al.* 2008).

Since the S3WCA diagnostic also yields instantaneous information for the fluid turbulence, *p.d.f.*'s for density and velocity fluctuations at $\tau = 0.78$ are shown at the mixing layer centerline (y = 0). The velocity fluctuation *p.d.f*'s of the vertical (v') and cross-stream (w') velocity components are shown in Figure 5.7 and have more noise than those at low A_t due to the reduced spatial resolution and the effects of large concentrations of helium, but they do exhibit

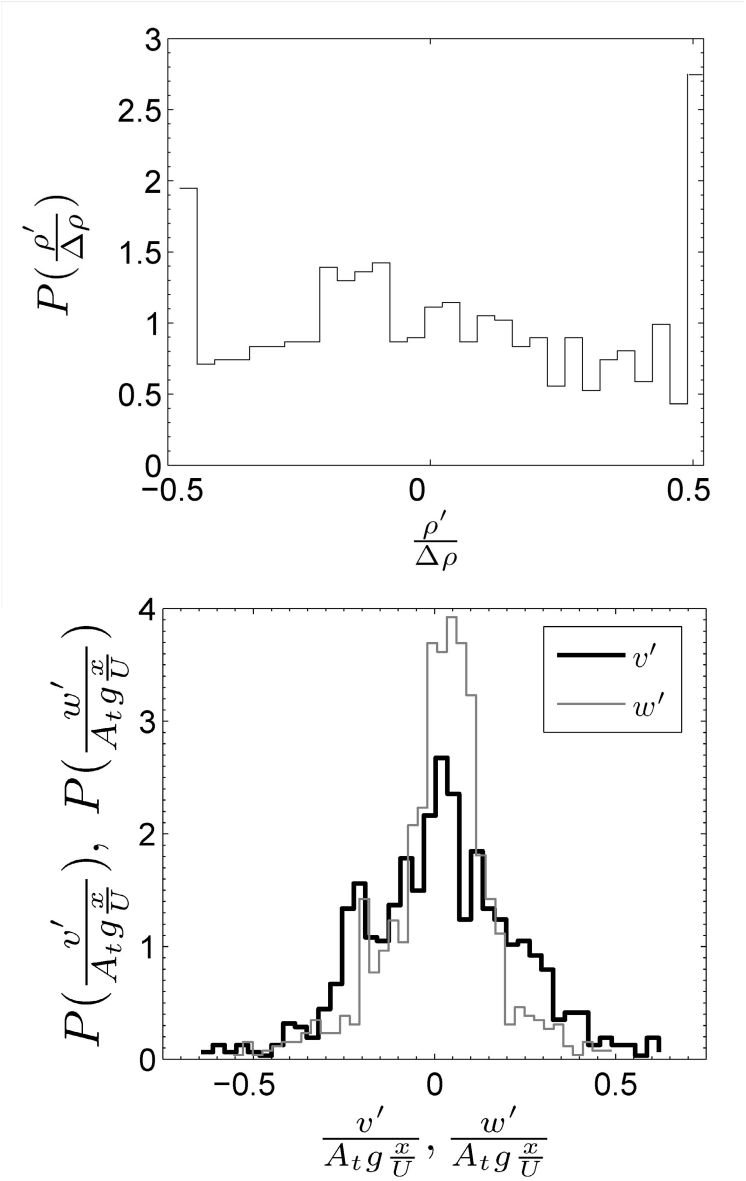

Figure 5.7. *P.d.f.* 's of the density and velocity fluctuations at $\tau = 0.78$ at the mixing layer centerline for $A_t = 0.6$.

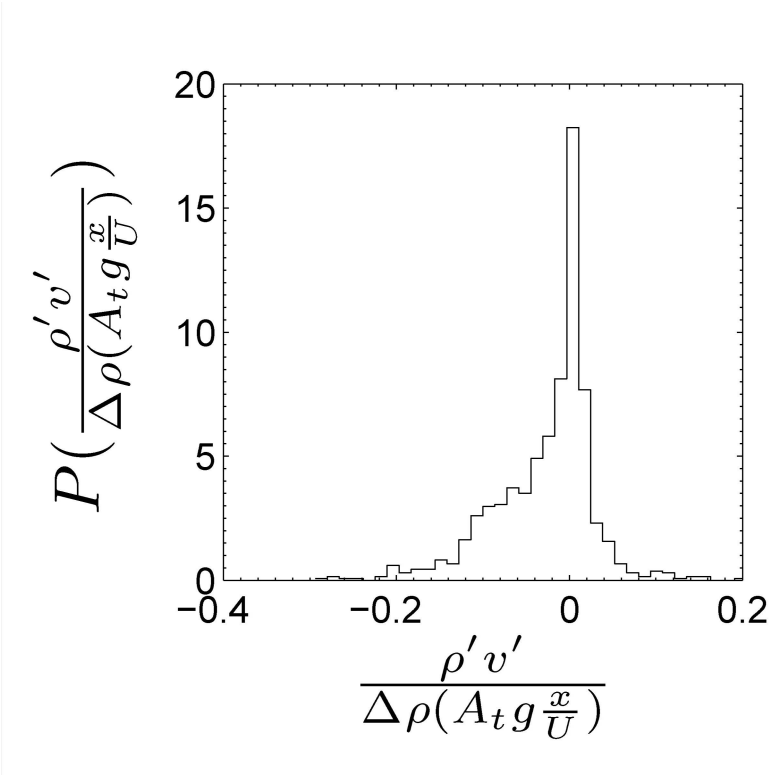

Figure 5.8. *P.d.f* of $\rho' v'$ at the mixing layer centerline for $\tau = 0.78$ and $A_t = 0.6$

many of the same features as those at lower Atwood numbers (Figures 4.1 and Figure 4.2 already described). The kurtosis of the velocity fluctuation distributions, a measure of the flatness of the distribution, is K_v = 3.3 and K_w = 4.6. These values are larger than reported earlier for A_t = 0.03 at τ = 1.33 of K_v = 2.17 and K_w = 2.97. The kurtosis of the cross-stream velocity fluctuations is 40% larger than the kurtosis of the vertical velocity fluctuations, demonstrating the anisotropy of buoyancy-driven turbulence. For τ = 0.78 and A_t = 0.6 the ratio of the *rms* of vertical to cross-stream velocity fluctuations is 1.5. The density fluctuation *p.d.f.,* also shown in Figure 5.7, shows a bi-modal distribution as seen at A_t = 0.03 for a similar time of evolution.

The *p.d.f.* of the vertical turbulent mass flux, $\rho' v'$ at τ = 0.78 is shown in Figure 5.8. Again, the measured *p.d.f.* was similar to that found at lower Atwood numbers (previously shown in Figure 4.7 for A_t = 0.03). Primarily negative turbulent mass fluxes in the vertical direction were expected, as bubbles of mostly light fluid rise and spikes of mostly heavy fluid fall through the mixing layer. This negative correlation of vertical velocity and density fluctuations results in a broad tail of the *p.d.f.* to negative values of the turbulent mass flux. In addition, the presence of mixed fluid in both the rising bubbles and falling spikes results in the large peak found about zero. The skewness (third moment of the distribution) and kurtosis (fourth moment of the distribution) of the *p.d.f.* can be used to quantitatively characterize the shape of the distribution. For the *p.d.f.* shown in Figure 5.8, $K_{\rho' v'}$ = 9.5 and $S_{\rho' v'}$ = -2.7. These are similar to those found at A_t = 0.03 and τ = 1.33 of $K_{\rho' v'}$ = 10.6 and $S_{\rho' v'}$ = -3.8. However, the negative tail of the *p.d.f.* does extend to larger non-dimensional values of the turbulent mass flux; this may be an indication of unique spike dynamics at larger A_t that results in larger growth rates of the heavier spikes. Figure 5.9 shows the measured energy density spectra of v' , ρ' and

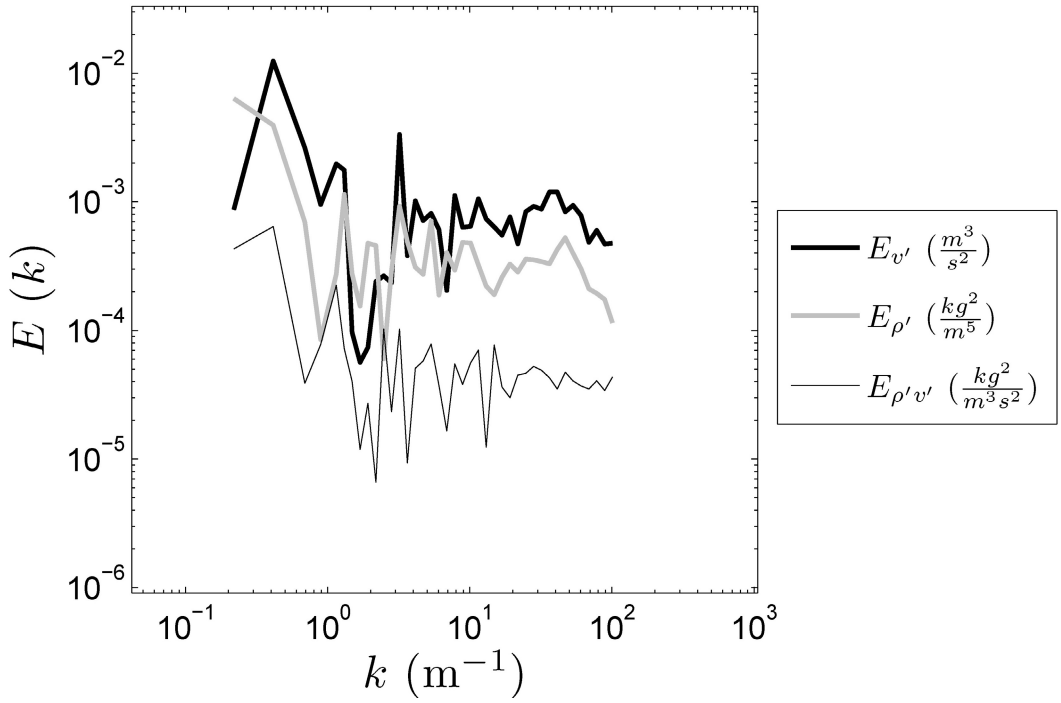

Figure 5.9. The measured energy density spectra for v' , ρ' and $\rho' v'$ at the centerline of the mixing layer for $A_t = 0.6$, $\tau = 0.78$, and $U_m = 2.0$ m/s. The reduced resolution to compensate for large concentrations of helium limits the frequency response to 83 Hz.

$\rho' v'$. The detrimental effect of large concentrations of helium and the eventuality that the cold-wire and hot-wire probes erroneously sense different fluid structures, required a reduction of the raw signals to four times the physical spatial resolution. This resulted in an actual sampling frequency of 83 Hz, or a final spatial resolution within the Nyquist limit of ~ 3.5 cm. When compared with the spectra of Figure 4.11 for A_t = 0.03, it is evident that only the large scale, energy containing region is captured by the diagnostic for A_t = 0.6. This limitation can be improved by obtaining a customized commercial probe with a smaller spatial resolution and integrated cold-wire. Further details of suggestions for a new probe configuration are described in Section 7.

Measurements at the mixing layer centerline (y = 0) for A_t = 0.6, maximum τ = 0.78, and maximum $\mathrm{Re}_{v'} = (h_b + h_s) v'_{rms} / \upsilon_{mix}$ = 4500 have been consistent with those obtained from the water and gas channel at much smaller $A_t \leq 0.04$. Although the penetration of the bubbles and spikes clearly grows asymmetrically, as indicated by the measurements of h_b and h_s, time-averaged statistics of velocity and density fluctuations and the velocity-density correlation at the mixing layer centerline (y = 0) show striking similarities to the more symmetric lower Atwood number mixing layers. Interestingly, the *p.d.f.* of $\rho' v'$ was shown to extend to larger normalized negative magnitudes of the turbulent mass flux than observed at low Atwood numbers, which warrants further investigation. However, these measurements were limited to intermediate times of evolution due to design and physical limitations of the current facility and the diagnostic probe, which will be addressed in Section 7.

6. CONDITIONAL STATISTICS IN RAYLEIGH-TAYLOR MIXING LAYERS

The instantaneous capability of the S3WCA diagnostic allowed conditional statistics to be determined for v', w', ρ', and $\rho'v'$ inside a mixing layer of air and helium, to separately investigate the bubble and spike dynamics. This is believed to have never been attempted experimentally in a Rayleigh-Taylor mixing layer, as the combined capabilities of the current experiment and diagnostic are the first of their kind for studies of Rayleigh-Taylor instabilities. Conditional statistics can be used to reveal interesting aspects of turbulent flows which cannot be observed through conventional measurements.

6.1 Bubble and spike dynamics using conditional statistics

A review by Antonia (1981) describes various methods and applications of conditional statistics for turbulent flows. Conditional averaging for examining turbulent flows has been performed extensively in shear-driven turbulence and also with hot-wire diagnostics. One example of conditional averaging using hot-wire diagnostics has been presented by Wygnanski and Fiedler (1970) for a shear mixing layer, conditionally averaging turbulent and non-turbulent flow using the signal $\left|\partial^2 u'/\partial t^2\right| + (\partial u'/\partial t)^2$ to attempt to detect turbulent flow. This was commonly used early in hot-wire anemometry, as this operation could be performed during data acquisition with analog devices of the time period. However, it is now more common to conditionally sample using scalar fluid markers; scalars can be more directly used to condition the flow measurements, as well as any other parameter of interest. Conditional statistics reported by Fabris (1983a, 1983b) used a temperature marker in a wake flow to distinguish between

turbulent and potential fluid in the wake. LaRue and Libby (1980) used a scalar marker to obtain conditional statistics, using helium concentration to condition measurements of an air turbulent boundary layer entraining laminar flowing helium. Measurements were conditionally averaged according to specific ranges of helium concentration to identify the contributions of each fluid to the originally air only turbulent boundary layer. The hot-wire interference probe used by LaRue and Libby was limited to conditional measurements of concentration, and only the streamwise velocity fluctuations, u'.

Conditional statistics are generally obtained using an intermittency function, *I(t)*, as presented by Pope (2000) as

$$I(t) = H_s\left[\omega(t) - \omega_{threshold}\right], \tag{6.1}$$

where H_s is the Heavie-side function, ω is vorticity, and $\omega_{\text{threshold}}$ is a threshold chosen to identify turbulent fluid. The intermittency function of (6.1) can be generalized to any conditional parameter, ϕ. For example the intermittency function can be modified to decompose a signal according to positive and negative values of a parameter through

$$I(t) = \frac{1 + \text{sgn}\left[\phi(t)\right]}{2}, \tag{6.2}$$

where conditional statistics are determined according to the sign of ϕ. The intermittency function of (6.2) is taken as a product with the unconditioned trace, and is used to decompose the current unconditioned data into contributions according to the sign of the parameters of interest.

As demonstrated in the visualizations of Section 1, buoyancy-driven turbulence is dominated by the penetration of bubbles and spikes as the two fluids interpenetrate and turbulently mix. Rather than separate the measured statistics according to turbulent and non-turbulent flow, as done in shear-dominated turbulent flows, the benefit of conditional statistics

for this investigation of buoyancy-driven turbulence is to separate the turbulent flow into bubble and spike dynamics.

One way the bubble and spike dynamics can be separately examined was by conditionally sampling the measured data traces according to the sign of the density fluctuations, ρ', as shown in the intermittency function of (6.2). The density fluctuation was determined as $\rho' = \rho - \overline{\rho}_{mix}$, where $\overline{\rho}_{mix} = (\rho_1 + \rho_2)/2$. At the mixing layer centerline, the average density of the mixing layer is approximately $\overline{\rho}_{mix}$, so that if $\rho' > 0$, the passing fluid is composed mostly of fluid 1 (heavy fluid spike) and if $\rho' < 0$ the inverse is true. A demonstration of this procedure for ρ', v', and $\rho' v'$ at A_t = 0.03 and τ = 1.33 is shown in the *p.d.f.*'s of Figure 6.1. The *p.d.f.* for the dominant velocity fluctuations, v', separated approximately into two fluids, are mirror opposites with equal v'_{rms}. The lighter fluid, $\rho' < 0$, associated with the rising bubbles corresponds to mostly positive vertical velocity fluctuations. The opposite is true of the heavy fluid, $\rho' > 0$. This is expected as RT mixing layers are dominated by the formation of bubbles and spikes, resulting in a strong negative correlation of density and vertical velocity fluctuations (which has been already demonstrated through the measurement of the cross-correlation coefficient, $R_{\rho' v'}$ = -0.74). However through the *p.d.f.*'s of Figure 6.1 is it is apparent that the heavy fluid ($\rho' > 0$) does not always correspond with negative vertical velocity fluctuations of the falling spikes composed mostly of heavy fluid, and light fluid ($\rho' < 0$) does not always correspond with positive vertical velocity fluctuations of rising bubbles. Some of the heavy fluid is entrained into the rising bubbles. This entrainment occurs through the vortical roll-up of the buoyant plumes and shearing of the bubbles and spikes as they move past each other. The inverse is also true as light fluid is entrained into the falling spikes. From the *p.d.f.*'s

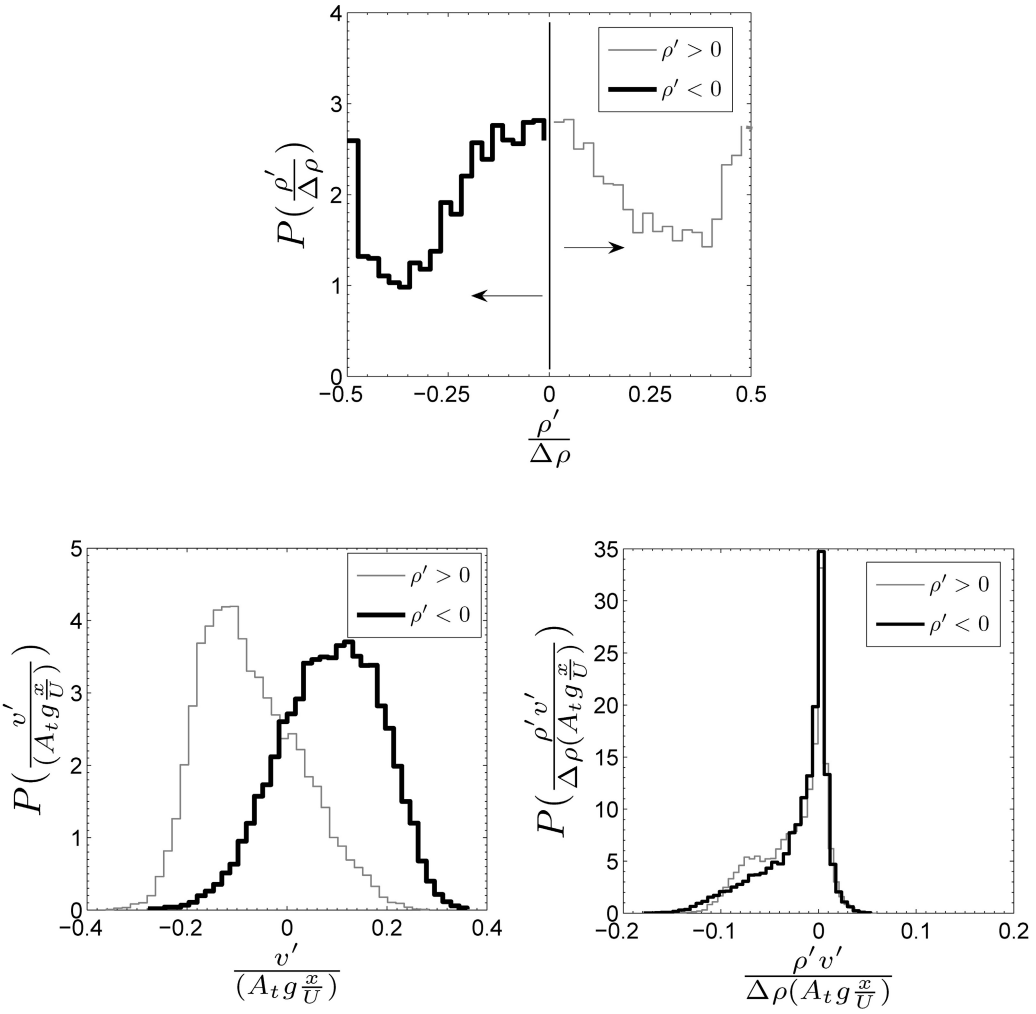

Figure 6.1. *P.d.f.*'s of ρ', v', and $\rho'v'$ at the mixing layer centerline for A_t = 0.03 and τ = 1.33, using the sampling condition of $\rho' > 0$ and $\rho' < 0$ to approximate the measured fluctuations as two fluids (heavy or light). The sampling condition used is illustrated in the *p.d.f.* of ρ' at the top.

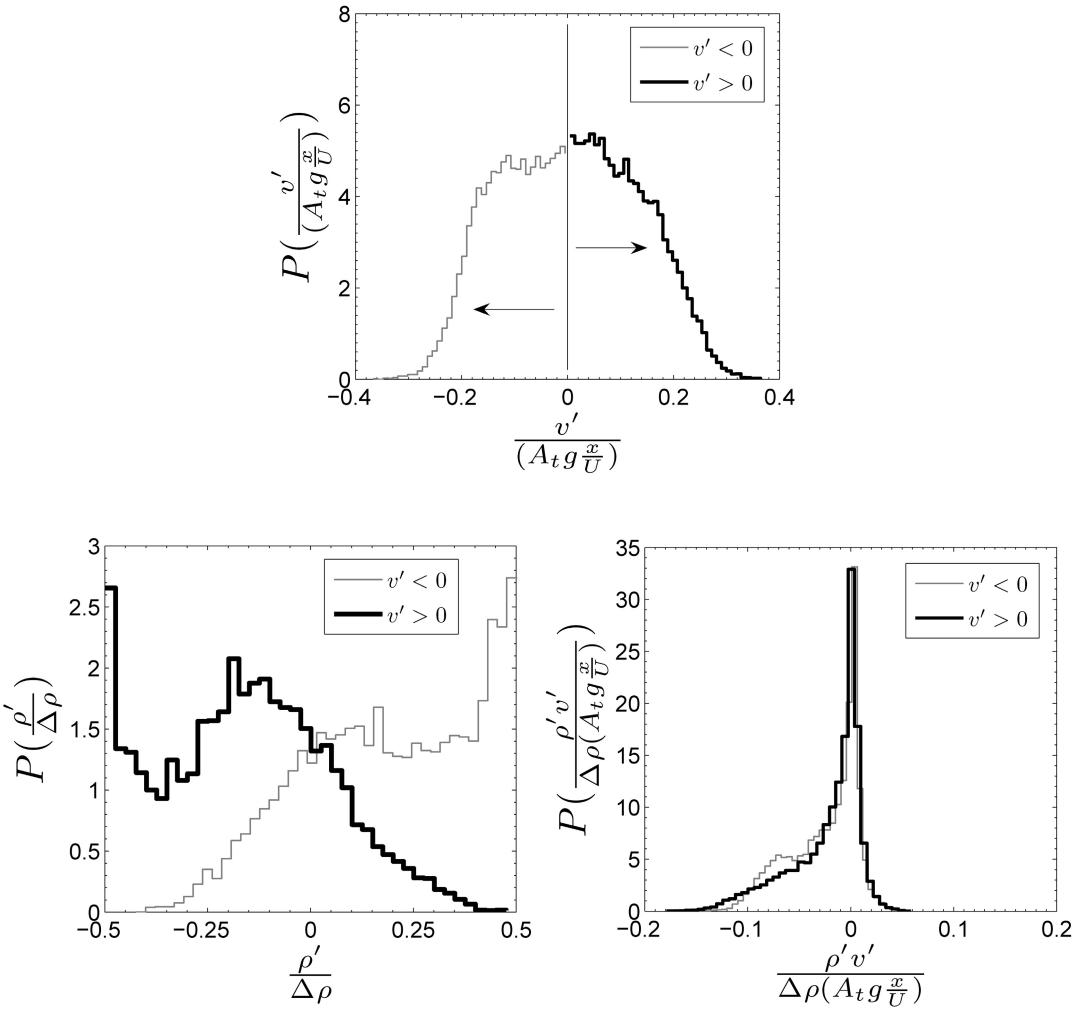

Figure 6.2. *P.d.f.*'s of ρ', v', and $\rho' v'$ at the mixing layer centerline for A_t = 0.03 and τ = 1.33, using the sampling condition of $v' < 0$ and $v' > 0$ to approximate the measured fluctuations as a bubble (rising fluid) or spike (falling fluid). The sampling condition used is illustrated in the *p.d.f.* of v' at the top.

	$\rho' > 0$	$\rho' < 0$	$v' < 0$	$v' > 0$	Conventional
A_t	0.03	0.03	0.03	0.03	0.03
x	1.75	1.75	1.75	1.75	1.75
τ	1.33	1.33	1.33	1.33	1.33
U_m	0.65	0.65	0.65	0.65	0.65
v'_{rms}	0.079	0.079	0.054	0.056	0.10
w'_{rms}	0.052	0.064	0.052	0.064	0.059
$\overline{v'}$	-0.065	0.063	-0.086	0.085	0
$\overline{w'}$	0.009	-0.0087	0.004	-0.004	0
$\Delta\rho$	0.074	0.074	0.074	0.074	0.074
ρ'_{rms}	0.011	0.011	0.016	0.015	0.020
$f_{v,1}$	0.72	0.27	0.67	0.31	0.51
$\overline{\rho'v'}/(\Delta\rho A_t gx/U)$	-0.027	-0.026	-0.027	-0.026	-0.026
$\overline{\rho'w'}/(\Delta\rho A_t gx/U)$	0.0026	0.0057	0.0018	0.0065	0.0042

Table 6.1. Summary of conditional averages for $A_t = 0.03$ and $\tau = 0.78$ at the mixing layer centerline ($y = 0$). (All units in m, kg, s)

of v', the symmetric nature of low Atwood number mixing layers about the centerline can be seen as the amount of heavy fluid entrained into rising bubbles and vice versa appears to be equal. This is indicated by the equal and opposite tails of the v' *p.d.f.*'s at $|v'/(A_t g\, x/U)| = 0.2$. The symmetric penetration and behavior of bubbles and spikes is also demonstrated in the conditional *p.d.f.* of the vertical turbulent mass flux, $\rho' v'$. Both conditions, $\rho' < 0$ and $\rho' > 0$, demonstrate identical *p.d.f.*'s with approximately equal mean vertical turbulent mass fluxes, $\overline{\rho' v'}$, which are listed in Table 6.1.

The $\rho' < 0$ and $\rho' > 0$ conditions are used to separate turbulence measurements into rising bubbles (mostly light fluid associated with $\rho' < 0$) and falling spikes (mostly heavy fluid associated with $\rho' > 0$). However in the *p.d.f*'s of Figure 6.1, it was shown that when using the $\rho' < 0$ and $\rho' > 0$ conditions to separate the bubble and spike behaviors of the buoyancy-driven flow, not all of the fluid in either condition was rising ($+v'$) or falling ($-v'$). Therefore it seems appropriate to also examine an additional conditional statistic by using the condition of $v' < 0$ (falling spike) and $v' > 0$ (rising bubble). A condition based on the sign of the vertical velocity fluctuations also decomposes the measurements approximately into bubble and spike dynamics. *P.d.f*'s using these conditions are shown in Figure 6.2. An illustration of the vertical velocity condition is shown in the *p.d.f.* of v'. In the *p.d.f.* of ρ', the entrainment of light fluid into the falling spikes and heavy fluid into the rising bubbles is seen clearer than shown in Figure 6.1, as both conditional ρ' *p.d.f*'s of Figure 6.2 contain heavy and light fluid. As shown in the *p.d.f.* of $\rho' v'$ in Figure 6.1, approximately identical *p.d.f.*'s are also observed using the sign of v' for conditional statistics.

A summary of conditional statistics using the described conditions is presented in Table 6.1. From Table 6.1, it can be seen with either conditional parameter, ρ' or v', that whether the mean or *rms* of the conditioned v' distributions is considered, the magnitudes are equal as expected at the centerline, with the symmetrical penetration of bubbles and spikes at A_t = 0.03. However, it is not clear which conditioning method or what velocity statistic is better suited to determine a characteristic velocity scale for the bubbles or spikes.

Further insight into the bubble and spike dynamics is found by examining the described conditional statistics at A_t = 0.6. As described in Section 5, measurements of the velocity fluctuations, molecular mixing parameter, and the vertical turbulent mass flux at A_t = 0.6 were consistent with previous lower A_t measurements at the mixing layer centerline. The uniqueness of the asymmetric growth of large Atwood number Rayleigh-Taylor (RT) mixing layers was not obvious in these conventional measurements and early times of the mixing layer development. However, the asymmetric behavior and differing dynamics of the bubbles and spikes were evident through image analysis of the developing A_t = 0.6 mixing layer. Since the S3WCA diagnostic simultaneously and instantaneously measures velocity and density within the mixing layer, characteristics of large Atwood number RT mixing layers were further investigated using the already described conditional statistics.

The same conditional sampling procedure is used as already performed for A_t = 0.03. Figure 6.3 shows *p.d.f.*'s of ρ', v', and $\rho'v'$ for A_t = 0.6 and τ = 0.78 at the mixing layer centerline (y = 0) using the $\rho' > 0$ and $\rho' < 0$ conditions. Unlike the *p.d.f.*'s of v' at A_t = 0.03, those found in Figure 6.3 are not mirrored. Instead more of the heavier fluid ($\rho' > 0$) was carried back up towards the top of the mixing layer after being entrained into the rising bubbles, than light fluid being carried down back down through the mixing layer by the falling spikes. As

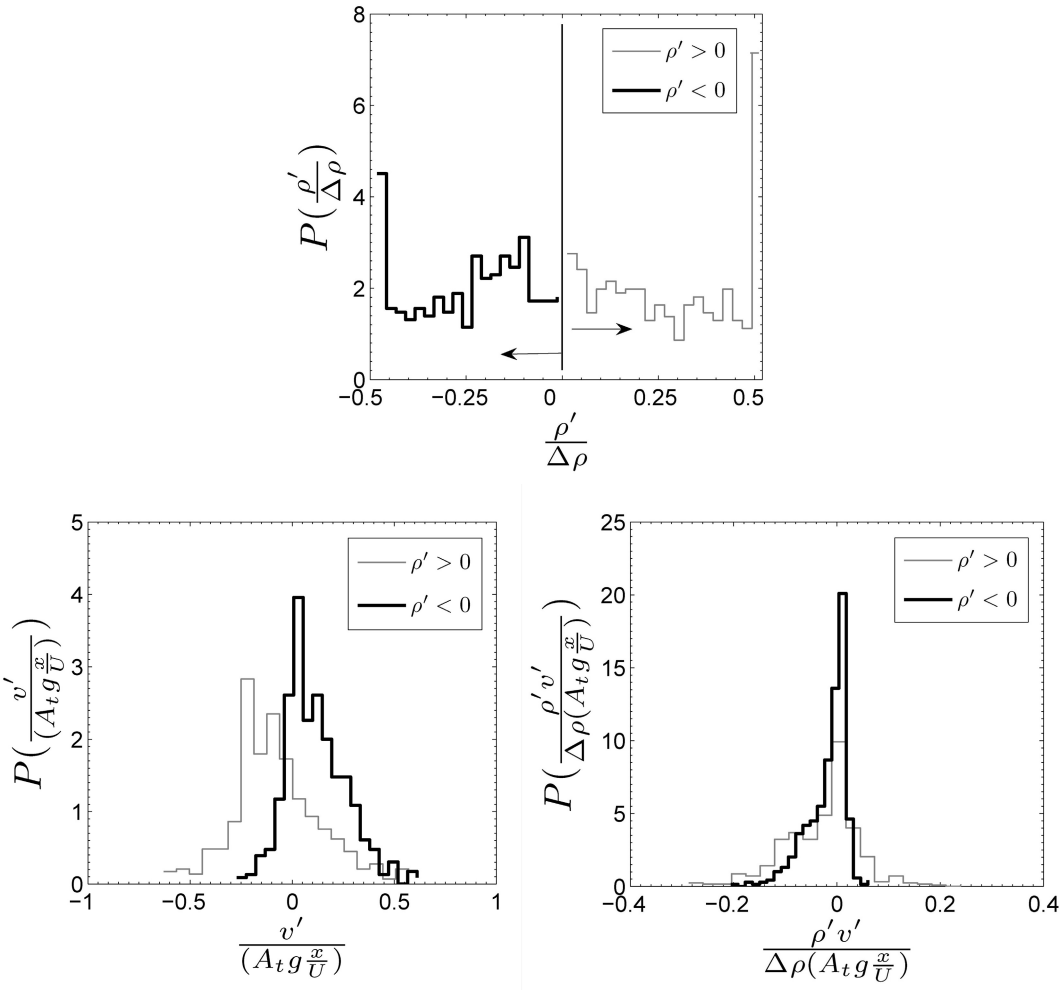

Figure 6.3. *P.d.f.*'s of ρ', v', and $\rho'v'$ at the mixing layer centerline for A_t = 0.6 and τ = 0.78, using the sampling condition of $\rho' > 0$ and $\rho' < 0$ to approximate the measured fluctuations as two fluids (heavy or light). The sampling condition used is illustrated in the *p.d.f.* of ρ' at the top.

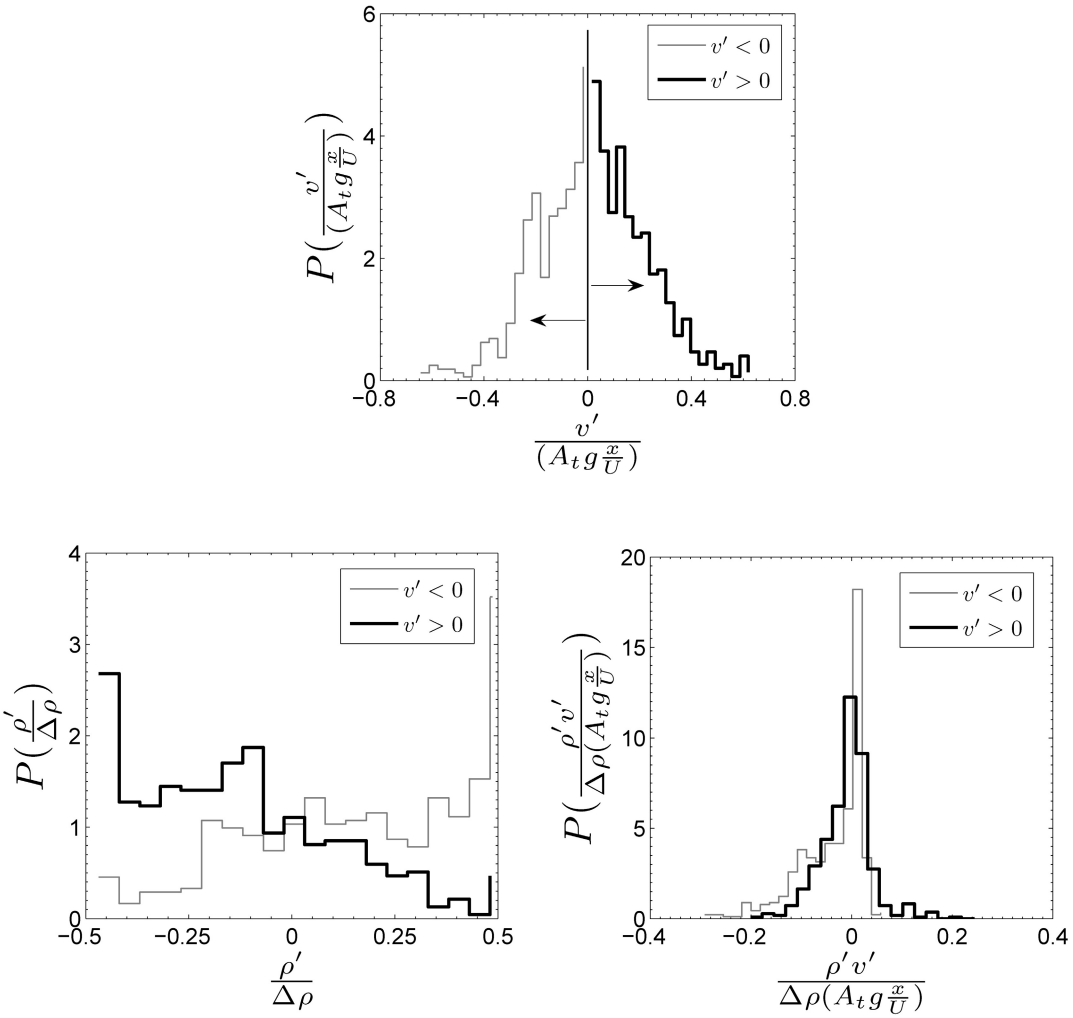

Figure 6.4. *P.d.f.*'s of ρ', v', and $\rho' v'$ at the mixing layer centerline for A_t = 0.6 and τ = 0.78, using the sampling condition of $v' < 0$ and $v' > 0$ to approximate the measured fluctuations as a bubble (rising fluid) or spike (falling fluid). The sampling condition used is illustrated in the *p.d.f.* of v' at the top.

	$\rho' > 0$	$\rho' < 0$	$v' < 0$	$v' > 0$	Conventional
A_t	0.6	0.6	0.6	0.6	0.6
x	0.7	0.7	0.7	0.7	0.7
τ	0.78	0.78	0.78	0.75	0.75
U_m	2.0	2.0	2.0	2.0	2.0
v'_{rms}	0.45	0.31	0.35	0.25	0.44
w'_{rms}	0.35	0.25	0.29	0.32	0.30
$\overline{v'}$	-0.21	0.19	-0.33	0.34	0
$\overline{w'}$	-0.02	0.02	-0.06	0.05	0
$\Delta\rho$	0.88	0.88	0.88	0.88	0.88
ρ'_{rms}	0.15	0.13	0.24	0.22	0.26
$f_{v,1}$	0.76	0.25	0.64	0.34	0.51
$\overline{\rho'v'}/(\Delta\rho A_t gx/U)$	-0.042	-0.025	-0.046	-0.021	-0.033
$\overline{\rho'w'}/(\Delta\rho A_t gx/U)$	-0.011	-0.0060	-0.0060	-0.011	-0.0060

Table 6.2. Summary of conditional averages for $A_t = 0.6$ and $\tau = 0.78$ at the mixing layer centerline ($y = 0$). (All units in m, kg, s)

a result, v'_{rms} for each condition is not equal; rather; v'_{rms} for the fluid associated with $\rho' > 0$ (heavier fluid) is approximately 1.5 times larger than that of the fluid determined from the condition $\rho' < 0$ (lighter fluid). It has already been shown in Section 5, that spikes (heavy fluid) penetrate into the light fluid farther than bubbles (light fluid) penetrate into the heavy fluid. Therefore, it can be inferred that negative vertical velocities associated with the spikes could be larger in magnitude. It was also observed that more heavy fluid was entrained into the bubbles than vice versa. As a result, it was expected that v'_{rms} from each of the ρ' conditions are not equal. Interestingly $\overline{v'}$ for the $\rho' > 0$ and $\rho' < 0$ conditions are approximately opposite, but equal at the mixing layer centerline. For this incompressible flow at the centerline, approximately equal quantities of fluid 1 and 2 (as indicated by the volume fractions) are present. Since the mean of the conditional v' measurements are approximately equal but opposite in sign, the net volume flux of the incompressible flow is approximately zero. This satisfies volume conservation at the mixing layer centerline for the incompressible mixing layer. In light of this fact, it is interesting to compare the $\rho'v'$ *p.d.f.* for the vertical turbulent mass flux for each ρ' condition as shown in Figure 6.3. Unlike the A_t = 0.03 results, the $\rho'v'$ *p.d.f.* is **not identical** for each condition. The heavy fluid is more likely to contain negative vertical turbulent mass flux of larger magnitude. This is also an indicator of the asymmetric penetration of the bubble and spikes, as Cook *et al.* (2004) demonstrated the growth rate for the mixing layer could be related to the vertical turbulent mass flux. Once these conditional distributions are averaged, it is evident that there is an imbalance in the turbulent vertical mass flux, where $\overline{\rho'v'}$ for the heavy fluid is 1.7 times larger than that for the lighter fluid. This is interesting because as seen earlier, conventional averages of the S3WCA measurements demonstrated greater consistency with the lower Atwood number measurements. This occurred despite an obvious

asymmetric growth of the bubbles and spikes, as observed through image analysis in Section 5 for A_t = 0.6. Therefore, conditional statistics provide a powerful tool to highlight differences in the A_t = 0.6 mixing layer from lower Atwood number behavior, which was not otherwise observable in the hot-wire measurements described in Section 5.

As with the A_t = 0.03 data, conditions of $v' < 0$ (falling spike) and $v' > 0$ (rising bubble) were also applied to the A_t = 0.6 data to develop conditional statistics. Conditional *p.d.f.*'s of ρ', v', and $\rho' v'$ are shown in Figure 6.4. Again, it can be seen that the $\rho' v'$ *p.d.f.* for each condition (approximately bubble or spike) are different, showing a larger negative vertical turbulent mass flux for the falling fluid (spike), where $v' < 0$. These results are summarized in Table 6.2. Using the $v' < 0$ and $v' > 0$ conditions allows the unconditioned data to be approximately decomposed again into its bubble and spike components. However, since it has been shown through the *p.d.f.*'s that bubbles and spikes are not completely composed of fluid 1 or fluid 2, it seems advantageous to also use density-weighted averages to determine characteristics associated with the bubbles and spikes. Specifically, the density-weighted averages for v' are determined as

$$v_1' = \left(\frac{\overline{\rho v'}}{\overline{\rho}} \right)_{v'<0} \text{ and } v_2' = \left(\frac{\overline{\rho v'}}{\overline{\rho}} \right)_{v'>0}, \tag{6.3}$$

where the subscripts 1 and 2 denote the heavy (spike) and light (bubble) conditions. Using these definitions, characteristic velocities for the spike and bubble dynamics for A_t = 0.6 at τ = 0.78 are v_1 = -0.39 m/s and v_2 = 0.37 m/s. These velocities also satisfy a volume conservation for the incompressible flow at the mixing layer centerline, where approximately equal amounts of fluid 1 and 2 are found, implying that the characteristic velocities for the turbulent bubbles and spikes should be of opposite sign but approximately equal in magnitude. The magnitudes of v_1' and v_2'

Conditional	A_t	τ	$\left(\frac{\overline{\rho v'}}{\overline{\rho}}\right)$	$\left(\frac{\overline{\rho w'}}{\overline{\rho}}\right)$	$\left(\frac{\overline{\rho v'^2}}{\overline{\rho}}\right)$	$\left(\frac{\overline{\rho w'^2}}{\overline{\rho}}\right)$	$\left(\frac{\overline{\rho v' w'}}{\overline{\rho}}\right)$	$\overline{\rho}$
$\rho' > 0$	0.03	1.33	-0.065	0.009	0.011	0.0028	4.0E-05	1.15
$\rho' < 0$	0.03	1.33	0.062	-0.009	0.010	0.0042	-1.1E-03	1.12
$v' < 0$	0.03	1.33	-0.086	0.004	0.010	0.0027	2.0E-04	1.15
$v' > 0$	0.03	1.33	0.085	-0.003	0.010	0.0042	-2.0E-04	1.12
Conventional	0.03	1.33	-0.001	0.002	0.010	0.0035	-5.2E-04	1.14
$\rho' > 0$	0.6	0.78	-0.24	-0.069	0.26	0.13	-0.004	0.97
$\rho' < 0$	0.6	0.78	0.19	0.061	0.14	0.10	0.026	0.51
$v' < 0$	0.6	0.78	-0.39	-0.029	0.22	0.09	0.007	0.86
$v' > 0$	0.6	0.78	0.37	-0.010	0.22	0.13	0.007	0.60
Conventional	0.6	0.78	-0.018	-0.020	0.21	0.11	0.007	0.76

Table 6.3. Conditional statistics using density-weighted averages.

are also similar to v'_{rms} = 0.44 m/s from the conventional measurement. The *rms* of the centerline vertical velocity fluctuations would have been typically considered a relevant velocity scale for the mixing layer at low Atwood numbers, where the bubble and spike dynamics are symmetric (Ramprabhu & Andrews 2004).

A summary of statistics determined using the described conditioning procedures and density-weighted averages are included in Table 6.3. From Table 6.3 the dominance of the Reynolds stress in the vertical direction (direction of gravity) over the horizontal direction is shown in both conventional and conditional measurements. In addition, the off-diagonal Reynolds stress component is small when compared with the diagonal components, due to symmetry of the mushroom shaped plumes.

Conditional statistics have successfully identified differences in the dynamics of buoyancy-driven turbulence at large Atwood number. Conventional time-averages of the turbulent flow exhibited a striking similarity to results at much smaller Atwood numbers, even though a clear asymmetry develops in the penetration of the heavy and light fluids on the opposite sides of the mixing layer. However, conditional statistics allow the dynamics of the RT mixing layer to be decomposed into separate bubble and spike (or heavy and light fluid) behaviors. At small Atwood numbers ($A_t \leq 0.1$, Banerjee 2006) the bubble and spike dynamics are approximately equivalent, however acting in opposing directions along the direction of gravity. At large Atwood number this is no longer true due to developing asymmetries in the mixing layer growth. Conditional statistics of the bubbles and spikes identified their unique behaviors which would otherwise be overlooked; the observation of a larger negative vertical turbulent mass flux and a larger vertical velocity *rms* of the spikes. In addition, density-weighted averages may be appropriate for analyzing the fluctuating quantities, as neither the bubbles or spikes were shown to be composed of only a single fluid.

6.2 Application of conditional statistics to two-fluid variable density turbulence models

A significant investment has been made in the Rayleigh-Taylor community to develop variable density turbulence models for Rayleigh-Taylor instabilities, and their application to predicting ICF processes. However validation of these turbulence models, particularly as they become more complex, becomes increasingly challenging. Experiments must progress and advance with the development of turbulence models to serve as a reference and validation tool. Developing experimental diagnostics and a methodology to compare the individual characteristics of heavy and light fluids within the mixing layer is necessary to further develop these variable density turbulence models.

In addition to providing unique insight into large Atwood number dynamics, there is great potential for using conditional statistics to compare with variable density turbulence models of Rayleigh-Taylor instabilities, such as the two-fluid model presented by Youngs (1989). Rayleigh-Taylor instabilities are driven by imbalances in the pressure gradient at the density interface separating the heavy and light fluids. Perturbations at the interface provide a catalyst for a release of potential energy stored by the heavy fluid located above the light fluid, opposing the gravitational acceleration. As potential energy stored in the form of the mean density field is released, heavy and light fluid interpenetrate in the form of bubbles (rising light fluid) and spikes (falling heavy fluid). A two-fluid model attempts to approximate the turbulent flow through the dynamics of bubbles and spikes in the RT mixing layer. This is accomplished by utilizing separate mass and momentum transport equations for the two fluids (heavy and light) that compose the mixing layer, similar to a two-phase flow description. This is done for example, by using a mass transport equation

$$\frac{\partial}{\partial t}\left(\rho_r f_{v,r}\right)+\frac{\partial}{\partial y}\left(\rho_r f_{v,r} v_r\right)=0 \tag{6.4}$$

or a volume fraction transport equation for incompressible RT flow

$$\frac{\partial}{\partial t}\left(f_{v,r}\right)+\frac{\partial}{\partial y}\left(f_{v,r}v_r\right)=0\,. \tag{6.5}$$

A formulation of this nature, where r denotes the fluid (1 for heavy, 2 for light), requires the mixing layer to be defined by the volume fractions, $f_{v,1}$ and $f_{v,2}$, of each fluid present and a characteristic velocity, v_1 and v_2, for each fluid. The characteristic velocity of the spike, v_1, is associated with fragments of heavy fluid which are falling, and is therefore negative. The opposite is true for the bubble. Other variable density turbulence models, such as the BHR model (Besnard *et al.* 1992), incorporate a single-fluid approach. In the case of the BHR model, continued development has been a primary focus in the Rayleigh-Taylor community at the Los Alamos National Laboratory (sponsors of the research). A spectral formulation of the BHR model was described by Steinkamp *et al.* (1999) and continued development of the BHR model is ongoing, with future plans to incorporate two-fluid concepts into the model formulation. Therefore, it is useful to develop a relationship between single-fluid and two-fluid variable density turbulence models. This will not be addressed in this investigation and is a future challenge for modeling buoyancy-driven turbulence. In this work, a framework was examined to compare experimental measurements with variable density models such as a two-fluid model. This had not been possible previously, as simultaneous and instantaneous measurements of velocity and density are necessary to examine experimental measurements through a two-fluid frame of reference (i.e. separate the turbulent flow into bubble and spike dynamics).

A consequence of a two-fluid formulation is that when $f_{v,1}$ = 0.5 the characteristic velocities should be equal and opposite, $-v_1 = v_2$, due to volume conservation. This generally occurs at the original interface location (y = 0) and is true with symmetric, small Atwood number flows. This was also approximately the case for the current measurements at A_t = 0.6 as

described in Section 5, even though the mixing layer is growing asymmetrically. The velocity requirement, $-v_1 = v_2$, of the two-fluid model at the original interface location for the mixing layer was used as a criteria for developing a framework to compare experimental measurements of buoyancy-driven turbulence with two-fluid models.

From the described conditional statistics, it appeared that the most appropriate method for creating a framework to compare measured experimental statistics with a two-fluid model of variable density turbulence, was to perform conditional statistics. This was accomplished by decomposing the mixing layer into dynamics of fluid 1 and 2 with the S3WCA diagnostic, according to the sign of the density fluctuations. Therefore, all fluid with densities $\rho' > 0$ were associated with spikes of fluid 1, and all fluid with $\rho' < 0$ were approximated as bubbles of fluid 2. The subsequent description of the turbulent RT mixing layer using density as a fluid marker to approximate two-fluid models follows communication with Andrews (2008). The following assumptions were used in the adaptation of the experimental results to a two-fluid approach:

a) Incompressible flow
b) Time trace can be treated as a plane spatial average through Taylor's hypothesis
c) Density can be used as a fluid marker to approximate the measurements as associated with either fluid 1 or fluid 2.

If the time trace of the measurements is considered as a spatial trace in the centerplane of the mixing layer, the number of occurrences of $\rho' > 0$, N_1, can be used to determine the fraction of fluid 1 observed by the probe in the measurement plane. The volume fraction can be determined such that

$$f_{v,1} = \frac{N_1}{N_1 + N_2} \text{ and } f_{v,2} = 1 - f_{v,1} \ . \tag{6.6}$$

The characteristic velocities for fluid 1 and 2 were determined through the conditional statistics $v_1 = \overline{v'}_1$ and $v_2 = \overline{v'}_2$ using the density conditions shown in Tables 6.1 and 6.2. Subsequently, the average vertical velocity should be related to the volume fractions and the characteristic velocities of each fluid through

$$\bar{v} = f_{v,1} v_1 + f_{v,2} v_2 = 0 , \tag{6.7}$$

which was found by combining the volume conservation for each fluid as shown in (6.5). The experimental approximation of a two-fluid flow (immiscible mixing layer) should therefore satisfy (6.7). Using the alternative "counting" method for determining the volume fractions for the conditioned statistic of Table 6.1 at A_t = 0.03 yielded $f_{v,1}$ = 0.49, which was very similar to the conventionally determined volume fraction of 0.51. Referring to Table 6.1 for the characteristic velocities of the two-fluid model, $v_1 = \overline{v'}_1$ and $v_2 = \overline{v'}_2$, (6.7) becomes

$$\bar{v} = f_{v,1} v_1 + f_{v,2} v_2 = 0.49 \times (-0.065) + (1 - 0.49) \times (0.063) = 3 \times 10^{-4} \text{ m/s.} \tag{6.8}$$

The normalized mean vertical velocity is then, $\bar{v}/v_1$ = -4 x 10^{-3}, which is very small as required by volume conservation. Another example of this method was determined by applying the same procedure to the conditional statistics shown in Table 6.2 for A_t = 0.6, where the alternatively defined volume fraction was $f_{v,1}$ = 0.48. The alternatively defined volume fraction was also very similar to the conventionally determined $f_{v,1}$ = 0.51. Referring to Table 6.2 for the characteristic velocities of the two-fluid model, $v_1 = \overline{v'}_1$ and $v_2 = \overline{v'}_2$, equation (6.7) for A_t = 0.6 becomes

$$\bar{v} = f_{v,1} v_1 + f_{v,2} v_2 = 0.48 \times (-0.21) + (1 - 0.48) \times (0.19) = -2 \times 10^{-3} \text{ m/s.} \tag{6.9}$$

The normalized mean vertical velocity is then, $\bar{v}/v_1$ = 1 x 10^{-2}. Again, the mean vertical velocity approximately satisfied volume conservation using conditional statistics. Thus, a methodology has been described to decompose the miscible measurements of the helium/air mixing layer with

the S3WCA diagnostic into a two-fluid (immiscible) framework for determining fluid volume fractions and characteristic velocities consistent with two-fluid modeling. This framework can be further extended to include the vertical turbulent mass flux, where the conventional miscible measurement is denoted by the subscript 0, such that

$$a_0 = \frac{\overline{\rho' v'}}{\overline{\rho}}. \tag{6.10}$$

The quantity a_0 is a fundamental parameter for variable density turbulence models such as the BHR model (Besnard *et al.* 1992). Steinkamp (1995) derived a two-fluid definition for the turbulent mass flux (immiscible case),

$$a_2 = \frac{f_{v,1} f_{v,2} (\rho_1 - \rho_2)(v_1 - v_2)}{\overline{\rho}}. \tag{6.11}$$

Differences in the vertical turbulent mass flux can now be illustrated between the miscible (experimental) and immiscible (two-fluid) approaches to buoyancy-driven turbulence. From the A_t = 0.03 case summarized in Table 6.1, the turbulent mass flux parameters are a_0 = -0.0014 and a_2 = -0.0021. The effect of molecular mixing present in the experiment reduces the magnitude of the turbulent mass flux when compared to an idealized immiscible two-fluid mixing layer. This is similarly seen in the A_t = 0.6 case summarized in Table 6.2, which gives a_0 = -0.070 and a_2 = -0.12. An interesting consequence of this analysis, is the ability to identify a new turbulent mixing parameter based on the vertical turbulent mass flux, which is similar to the molecular mixing parameter, θ, defined for the density variance. Andrews (2008) defined a mixing parameter for the turbulent mass flux ,

$$\kappa = 1 - \frac{a_0}{a_2}, \tag{6.12}$$

where $\kappa = 1$ when a_0 and the turbulent mass flux is zero (as the mixing layer is completely molecularly mixed) and $\kappa = 0$ when $a_0 = a_2$ and there is only interpenetration of the heavy and light fluids but no molecular mixing (immiscible, two-fluid case). For the measurements summarized in Tables 6.1 and 6.2 for $A_t = 0.03$ and $A_t = 0.6$, the values of the mixing parameter for the turbulent mass flux are 0.33 and 0.42, respectively. This conditioning procedure has been extended to the remaining experimental measurements at the mixing layer centerline to determine the values of the turbulent mass flux mixing parameter, κ. Figure 6.5 includes these results for both the $A_t = 0.03$ and $A_t = 0.6$ data sets plotted versus τ and Reynolds number [$Re_{v'} = (h_b + h_s)v'_{rms} / \upsilon_{mix}$]. The molecular mixing parameter, θ, is also shown for comparison. The average turbulent mass flux mixing parameter for all experiments at the mixing layer centerline is $\kappa = 0.32$, which is smaller than the measurements of $\theta = 0.70$ at late-time. The differing magnitudes of the two measures of mixing, κ and θ, is an interesting result. This may imply that the two mixing parameters capture different physical effects within the mixing process. The molecular mixing parameter, θ, directly relates the intensity of the density fluctuations ($\overline{\rho'^2}$) to the segregation of the two fluids within the mixing layer (this includes the effects of molecular and turbulent diffusion). The turbulent mass flux parameter however uses the turbulent transport of mass to quantify mixing, which may more directly capture diffusion effects of the turbulent field. From Figure 6.5 it is apparent that the value of κ is more consistent for the $A_t = 0.03$ measurements, varying from 0.27 to 0.33. The $A_t = 0.6$ results are less consistent, perhaps as a result of the lower quality of the large Atwood number measurements when compared to the $A_t = 0.03$ results. The consistency of the $A_t = 0.03$ results seems to imply that there may be a self-similar value of κ, similar to the asymptotic behavior which has also been observed in the conventional molecular mixing parameter, θ. The true

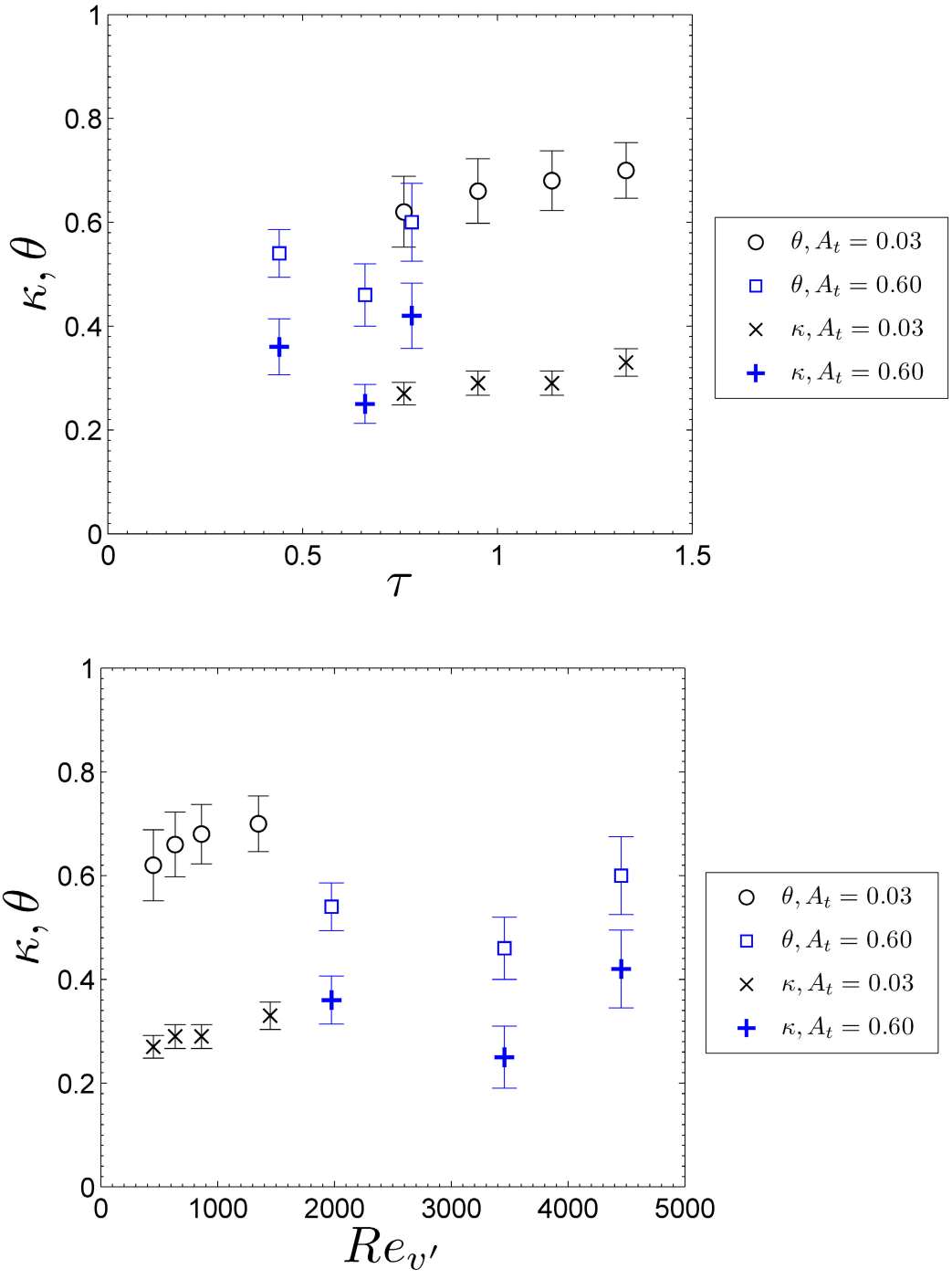

Figure 6.5. Evolution of the turbulent mass flux mixing parameter, κ, at the mixing layer centerline for A_t = 0.03 and A_t = 0.6 plotted versus τ and Reynolds number. The molecular mixing parameter, θ, is also shown for comparison.

asymptotic behavior of the molecular mixing parameter, θ (which is based on measurements of the density variance) is difficult to determine. In the large-eddy simulation of Cook *et al.* (2004), a mixing transition which occurs at high Reynolds number was found, which resulted in increasing amounts of molecularly mixed fluid (increasing θ). Therefore, θ may not reach self-similar or asymptotic values until high Reynolds number, which has been difficult to obtain in experiments. The turbulent mass flux mixing parameter, κ, relies on measurement of $\overline{\rho' v'}$, which is directly related to the growth of the mixing layer and production of turbulent kinetic energy. Therefore, the turbulent mass flux mixing parameter, κ, may provide an alternative method for examining turbulent mixing in Rayleigh-Taylor mixing layers, which has more direct physical connections to the self-similar and buoyancy-driven growth of the mixing layer.

7. SUGGESTIONS FOR FUTURE WORK

This work has applied the hot-wire diagnostic and gas channel to the limit of their capabilities. This includes simultaneous measurements of velocity and density at the mixing layer centerline up to A_t = 0.6 and non-dimensional times of $\tau \approx 0.8$. It was shown that the hot-wire diagnostic can obtain accurate measurements at the mixing layer centerline where the vertical velocity fluctuations are limited to $v'/\overline{U} \sim$ 20% and the average volume fraction of helium sensed by the hot-wire diagnostic is only 44%. However, special considerations in analyzing the data are required, resulting in the current measurement limitation of $\tau \sim 0.8$ at A_t = 0.6. The gas channel facility will need modification to obtain measurements at larger times. In addition, the configuration of the cold-wire and hot-wire probes will need to be improved to obtain measurements in higher concentrations of helium, and improve the spatial resolution.

These capabilities have been accomplished using a standard 55P91 three-wire hot-wire probe in combination with a standard 55P16 single-wire probe used as a cold-wire anemometer. Using standard hot-wire equipment has been an economical and timely approach to validating the S3WCA diagnostic and obtaining the current measurements inside the mixing layer for A_t = 0.6. The limitation with two separate probes (one for velocity and the other for temperature) gives a combined spatial resolution of 6 mm as the two probes had to be placed side by side to prevent probe interference from the cold-wire probe. This leads to difficulties in obtaining accurate velocity measurements in large concentrations of helium, when the two probes do not sense the same fluid and the hot-wire voltage sensitivities to helium are significant. Above $f_{v,he}$ = 40%, the hot-wire voltage sensitivities increase non-linearly to several times larger than at smaller concentrations (Banerjee 2006). This has precluded its use in the current research below the mixing layer centerline at A_t = 0.6, where larger concentrations of helium are more likely, and

the errors introduced by the helium are too large to overcome. However, through modifications to the gas channel facility and a customized hot-wire probe for this application, these limitations can be addressed as described next.

7.1 Suggested improvements to the S3WCA diagnostic

Improvements in the configuration of the hot-wire and cold-wire probes will allow for more accurate measurements, and extend the capability of the diagnostic to higher concentrations of helium. As already indicated, the diagnostic relies on the ability to identify fluid passing the set of probes with the cold-wire. To obtain accurate measurements, the cold-wire must sense the same fluid as the hot-wire probes. Currently the cold-wire and hot-wire probes are separate, and must be placed side by side to place them close together without obstructing the flow and interfering with the velocity or temperature measurements.

An attractive alternative would be to obtain a customized probe with the cold-wire integrated as a fourth wire into a three-wire hot-wire probe. To increase the likelihood of the cold-wire and hot-wires sensing the same fluid, both sensors should be placed in-line on the probe axis (stream-wise direction). The dominant U-velocity component will ensure that all probes will likely sense the same fluid. This is the concept behind the design of the three-wire hot-wire probe. However, there are two concerns when designing an integrated cold-wire / hot-wire probe. The cold-wire sensor is sensitive to temperature and must be placed relative to the hot-wires so that the temperature wake from the hot-wires does not interfere with the temperature measurement of the cold-wire. This can be accomplished by placing the cold-wire in front of the three hot-wire sensors. Then the cold-wire must be staggered in front of the hot-wire sensors so as not to completely obstruct the fluid and create an unwanted wake which would adversely affect the velocity measurement.

If possible it would also be advantageous to reduce the sensor and probe size of the measurement system. This could be done by utilizing a smaller diameter wire (< 5 micron) allowing each sensor to be reduced in size. It would be valuable however to reduce the overall size of the probes while retaining the existing geometry of the three-wire probe. This would allow the existing literature on three-wire anemometry and the current analysis to be used in the future.

7.2 Suggested modifications to the gas channel facility

To obtain measurements at the centerline of the mixing layer beyond $\tau = 0.8$ at $A_t = 0.6$, the channel velocity, U_m, for the channel must be increased. Increasing the advection velocity will maintain the ratio $v'/\overline{U}$ within necessary levels for accurate measurement. The consequences of increasing the advection velocity on the design of the current facility are as follows:

- Larger helium flow rate capacities
- Larger air flow rate capacities
- Re-design of the air and helium delivery and inlets to handle larger volumetric flow rates
- Integrate a heat exchanger into the helium delivery system to raise the temperature of the rapidly expanding helium to a temperature closer to the ambient environment
- Lengthening of the test section of the facility where measurements are obtained to accommodate the larger channel velocities as a result of Taylor's Hypothesis $t = x/U$

Currently, three helium lines consisting of 22 helium bottles that delivers helium at a flow rate of 0.23 lb/s for ~ 2 minutes for experiments at $A_t = 0.6$ and $U_m = 2$ m/s. An increase in the channel velocity will require additional helium lines and bottles. This will require additional space significantly above what is currently available, necessitating a rearranging of the current laboratory or a larger laboratory space. In addition, the current ducts which deliver air and helium was only designed to handle volumetric flow rates consistent with the current channel velocity of 2 m/s. The duct has proven to be too restrictive to handle larger volumetric flow rates than currently used. It is therefore necessary to enlarge the delivery system and re-design the inlet section of the gas channel to more closely resemble less-restrictive contractions associated with wind tunnels. The final consequence of increasing the advection velocities for the channel is that the measurements of interest will lie further downstream. This requires that the test section be increased in length beyond the current 2 m.

Using the previously described limitations of the hot-wire diagnostic and estimates for the magnitude of the vertical velocity fluctuations, predictions are made for design parameters for future experiments at $A_t = 0.6$. The magnitude of the vertical velocity fluctuations can be estimated when the mixing layer approaches self-similarity by taking the time derivative of the expression for the self-similar growth of the half-mix width and substituting $t = x/U$.

$$h_s = \alpha_s A_t g t^2 \tag{7.1}$$

$$v'_{rms} = 2\alpha_s A_t g \frac{x}{U_m} \tag{7.2}$$

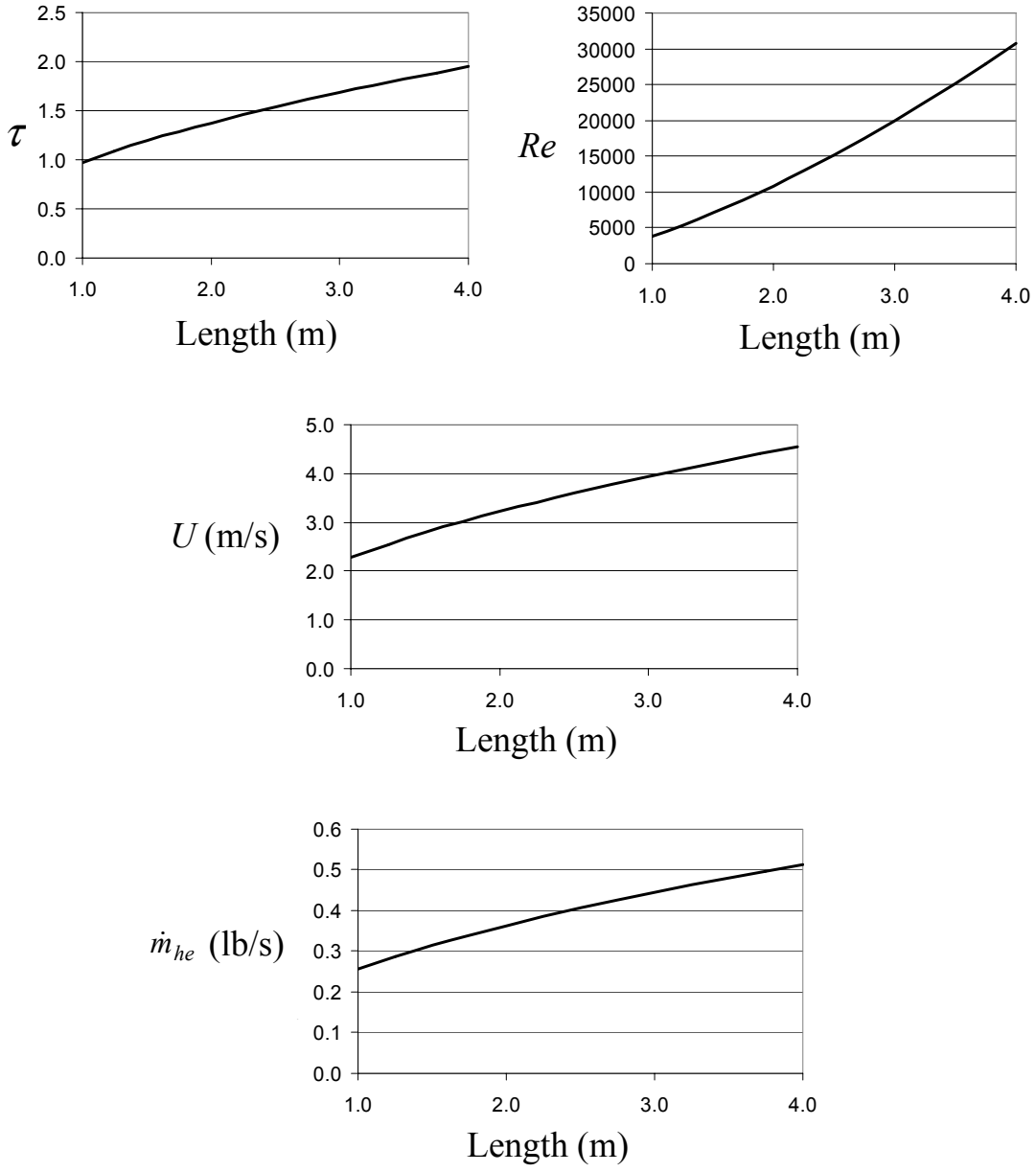

Figure 7.1. Design calculations for A_t = 0.6 taking into consideration the limitations of the magnitude of the vertical velocity fluctuations which can be accurately measured.

Re-arranging (7.2) to yield the ratio v'_{rms}/U_m and substituting in the condition previously established for accurate hot-wire measurements yield

$$\frac{v'_{rms}}{U_m} = 2\alpha_s A_t g \frac{x}{U_m^{\,2}} \quad \text{with} \quad \frac{v'_{rms}}{U_m} \approx 0.2 \tag{7.3}$$

$$U_m = \left(\frac{2\alpha_s A_t g x}{0.20} \right)^{\frac{1}{2}}, \tag{7.4}$$

a relationship which can be used to determine channel velocities necessary to obtain accurate velocity measurements at a particular A_t and x-location. Using (7.4), design predictions are made for A_t = 0.6 in Figure 7.1 based upon varying test section length. The helium mass flow rate is based upon the cross-sectional area of the current facility of 0.36 m^2 for each inlet stream. Rather than using the low Atwood number Reynolds number of Snider and Andrews (1994), a more universal definition is used for these estimates, where $\mathrm{Re} = h_{tot} v'_{rms}/\upsilon$. To obtain late-time measurements at τ = 1.5 for A_t = 0.6, the test section would need to be at least 2.5 m in length (additional length may be required past the measurement location of 2.5 m to prevent interference from the exit flows) with an advection velocity of U_m = 3.5 m/s. This would allow $Re \approx$ 15,000 to be reached.

7.3 Future experiments

With the suggested improvements and modifications to both the S3WCA diagnostic and gas channel, additional experimental measurements necessary to further validate numerical simulations and turbulence models can be performed. These experiments are prioritized in the following list:

- Late-time (up to $\tau = 1.5$) centerline measurements of velocity and density statistics for $A_t = 0.6$.
- Profile of velocity and density statistics across the mixing layer at $\tau = 1.5$ for $A_t = 0.6$ to determine an energy budget.
- Late-time and high *Re* measurements of velocity and density statistics at $A_t = 0.25$, where more complete studies can be performed at an economical cost. At $A_t = 0.25$ a $Re = 11{,}000$ can be achieved at $U_m = 2.0$ m/s at $x = 2.5$ m (test section total length ~ 3 m) and $\tau = 1.8$.

Atwood number 0.25 experiments would initially only require modifications to the length of the facility. This would allow further re-design of the delivery and inlet systems for future $A_t = 0.6$ experiments to be performed in parallel. Through modification of the facility and diagnostics, the laboratory will be able to achieve higher *Re* and late-time measurements of RT mixing layers up to $A_t = 0.6$, and beyond.

8. CONCLUSIONS

An experimental investigation focusing on the simultaneous measurement of velocity and density in buoyancy-driven turbulence was performed in a gas channel facility using helium and air. The gas channel provides a unique platform for fundamental investigations of Rayleigh-Taylor instabilities. The facility has parallel streams of air (heavy) above a helium/air mixture (light), that develop into a buoyancy-driven turbulent mixing layer. The statistically steady nature of the experiment is unique, giving statistical measurements of $\overline{u'^2}$, $\overline{v'^2}$, $\overline{w'^2}$, $\overline{\rho'^2}$ and $\overline{\rho' v'}$ to characterize the turbulent physics and validate numerical simulations and turbulence models. Measurement of the primary vertical turbulent mass flux, $\overline{\rho' v'}$, is particularly important for its role in the production of turbulent kinetic energy (Chassaing *et al.* 2002).

A new hot-wire diagnostic (S3WCA) was developed to obtain simultaneous and instantaneous measurements of velocity and density fluctuations within the Rayleigh-Taylor mixing layer of helium and air. This is particularly challenging for hot-wire diagnostics due to the varying thermal properties of the binary mixture. Previous hot-wire diagnostics including the MPMO technique, used in this facility by Banerjee (2006), employ multiple hot-wire overheat ratios to measure time-averaged velocities and fluid concentration. The S3WCA diagnostic, as a part of the present work, uses a three-wire hot-wire probe and temperature as a fluid marker to operate in a mixture of air and helium, where $Le \sim 1$ (ratio of thermal to mass diffusion). Temperature has been shown as an accurate fluid marker through a calibration experiment as a result of the helium and air properties. The new S3WCA diagnostic has led to new measurements of $\overline{\rho' v'}$ in the Rayleigh-Taylor mixing layer at $A_t = 0.03$ and $A_t = 0.6$. Of particular interest is the investigation of turbulence at large Atwood numbers ($A_t = 0.6$), where

the mixing layer no longer grows symmetrically about the mixing layer centerline. Further insight into the dynamics of this asymmetry are of particular interest. A summary of the conclusions/results drawn from this investigation follows and is subdivided according to each objective for this study.

Objective 1) To create a new diagnostic for collection of measurements to capture the physics of RT mixing through the capability to simultaneously and instantaneously measure velocity and density fluctuations and their correlations ($\overline{v'^2}$, $\overline{w'^2}$, $\overline{\rho'^2}$ and $\overline{\rho' v'}$).

- Temperature can be accurately used as a fluid marker in a mixture of helium and air. This has been proven through a calibration experiment.
- When comparing A_t = 0.03 results obtained using the S3WCA diagnostic with previous low A_t measurements in the water and gas channel facilities, good agreement was found for the measured mixing layer growth parameters, velocity fluctuation anisotropy and *p.d.f.* behavior, and measurements of molecular mixing.
- The S3WCA diagnostic can successfully used at large Atwood number (A_t = 0.6) in large concentrations of helium in air where there are large density and thermal property differences between the two inlet streams.
- The S3WCA diagnostic can successfully obtain measurements of $\overline{u'^2}$, $\overline{v'^2}$, $\overline{w'^2}$, $\overline{\rho'^2}$ and $\overline{\rho' v'}$ up to a turbulent intensity of $v'/U \sim 20\%$.
- The performance of the S3WCA diagnostic can be improved and extended to use in larger concentrations of helium by developing a customized probe with a cold-wire integrated into the hot-wire probe. Ideally, all wire sensors

should be placed inline along the probe axis. This will increase the likelihood all probes sense the same fluid structures and reduce the probe's overall dimensions.

- Reported for the first time experimentally are instantaneous measurements of the vertical turbulent mass flux for a Rayleigh-Taylor mixing layer, $\overline{\rho' v'}$. At the centerline of the mixing layer for A_t = 0.03, where production of turbulent kinetic energy is at its maximum, the *p.d.f.* of the primary turbulent mass flux is significantly skewed. Rather than being symmetric about a flux of zero as found with the horizontal turbulent mass fluxes, the vertical turbulent mass flux is likely to be negative, with a narrow peak at zero associated with mixed fluid. The likelihood of large negative turbulent mass fluxes decreases away from the mixing layer centerline as the production of turbulent kinetic energy decreases and smaller average turbulent mass fluxes are found.
- When non-dimensionalizing the *p.d.f.* of $\rho' v'$ at the mixing layer centerline using the velocity and density scales, $A_t gx/U$ and $\Delta\rho$, the *p.d.f.* demonstrates a collapse of the measured distributions for non-dimensional times τ = 0.76 – 1.33, thus demonstrating a universal $\rho' v'$ *p.d.f.* at the mixing layer centerline at low Atwood number.
- The energy density spectra for $\rho' v'$ was measured experimentally for the first time in a Rayeigh-Taylor mixing layer. For the non-dimensional times measured, the distribution of energy for fluctuations of the primary turbulent mass flux closely follows the behavior of the turbulent fluctuations of the

vertical velocity component. This illustrates the importance of the velocity spectrum for its influence on $\rho'v'$ and the role of the vertical turbulent mass flux on the growth of the mixing layer.

Objective 2) To use the new diagnostic to elucidate the physics of large Atwood number RT mixing.

- Experiments up to A_t = 0.6 have been successfully performed in a gas channel facility of this design using helium and air.
- Large density differences for A_t = 0.6 result in an asymmetric growth of the bubble and spike sides of the buoyancy-driven mixing layer. At late-time, $\tau \geq 1.2$, the mixing layer demonstrates a quadratic growth with $h_s / h_b = 1.55$ and self-similar growth parameters $\alpha_b = 0.060 \pm 0.004$ and $\alpha_s = 0.088 \pm 0.006$.
- The S3WCA diagnostic was successfully used at A_t = 0.6 to obtain the first statistical, experimental measurements of $\overline{v'^2}$, $\overline{w'^2}$, $\overline{\rho'^2}$ and $\overline{\rho'v'}$ at large Atwood number. However, special considerations had to be made that limit the performance of the diagnostic. Measured time-averaged statistics of the velocity and density fluctuations at the mixing layer centerline from $0.44 \leq \tau \leq 0.78$ agree well with small Atwood number ($A_t \leq 0.04$) results when non-dimensionalized with self-similar velocity and density scales.
- Although conventional time-averaging did not illustrate the uniqueness of large Atwood number turbulence, conditional statistics highlight differences in the mixing layer resulting from the developing asymmetry. In particular,

a larger turbulent mass flux, $\overline{\rho' v'}$, and larger vertical velocity fluctuations are observed for the downward moving spikes.

- Conditional statistics based on the sign of the vertical velocity fluctuations effectively separated the dynamics of the mixing layer into the bubble and spike dynamics. Using density-weighted averages of the bubble and spike distributions may provide a basis for describing the non-Boussinesq turbulent flow.
- Conditional statistics based on the sign of the density fluctuations can be used as framework to compare experimental measurements of the miscible helium/air mixing layer with immiscible, two-fluid, variable density turbulence models for comparison and validation. In addition, the two-fluid framework has led to the introduction of a new turbulent mixing parameter, κ, based on the vertical turbulent mass flux, $\overline{\rho' v'}$. Here κ represents a measure of the "degree of segregation" of the bubble and spike turbulent mass flux.

With the new S3WCA diagnostic, simultaneous and instantaneous measurements of the velocity and density fluctuations were obtained inside a Rayleigh-Taylor mixing layer. This has led to the first reported experimental, instantaneous measurements of $\rho' v'$ at any Atwood number. In addition, the gas channel facility was modified and successfully used to perform experiments up to A_t = 0.6, the largest A_t achieved in the Texas A&M facilities. The S3WCA diagnostic was successfully used in A_t = 0.6 experiments to obtain the first statistical, experimental measurements of velocity and density fluctuations at large Atwood number. Although conventional time-averages of velocity and density fluctuations demonstrated

similarity with lower A_t ($A_t \leq 0.04$) observations, conditional statistics separating the bubble and spike dynamics demonstrated the uniqueness of the spikes at $A_t = 0.6$; particularly through the larger negative vertical turbulent mass flux and larger *rms* velocity fluctuations associated with the faster growing spikes. This work has identified several limitations of the current diagnostic and facility. The experimental facility and diagnostic will require modification and improvements to further expand on this work and obtain late-time, high *Re* (~ 15000) measurements of large Atwood number turbulence; specifically, an improved set of probes for the diagnostic and an increase in the length and available channel velocities for the facility. However, this work has produced new data and results even with these limitations. This was shown through the unique statistical capabilities, and the first conditional turbulence measurements for RT mixing, that were used in this study to describe the RT bubble and spike dynamics. These unique and one of a kind experimental measurements in RT turbulence allow for numerical simulation and turbulence modeling validation in support of ICF initiatives.

REFERENCES

Andreopoulos J. 1983 Statistical errors associated with probe geometry and turbulence intensity in triple hot-wire anemometry. *J. Phys. E: Sci. Instrum.* **16**, 1264-1271.

Andrews M. J. & Spalding D. B. 1990 A simple experiment to investigate two-dimensional mixing by Rayleigh-Taylor instability. *Phys. Fluids A* **2**, 922-927.

Andrews M. J. 2008 Private communications on conditional statistics for two-fluid approximations.

Antonia R. A. 1981 Conditional sampling in turbulence measurement. *Ann. Rev. Fluid Mech.* **13**, 131-156.

Banerjee A. 2006 Statistically steady measurements of Rayleigh-Taylor mixing in a gas channel. PhD Dissertation, Texas A&M University, College Station.

Banerjee A. & Andrews M. J. 2006 Statistically steady measurements of Rayleigh-Taylor mixing in a gas channel. *Phys. Fluids* **18**, 035107.

Banerjee A. & Andrews M. J. 2007 Convective heat transfer correlation for a binary air-helium mixture at low Reynolds number. *J. Heat Transfer* **129**, 1-12.

Banerjee A., Kraft W. & Andrews M. J. 2008 Detailed measurements of a Rayleigh-Taylor mixing layer from small to intermediate Atwood numbers. *J. Fluid Mech.* (in preparation).

Beale J. C. & Reitz R. D. 1999 Modeling spray atomization with Kelvin- Helmholtz/Rayleigh-Taylor hybrid model. *Atomization and Sprays* **9**, 623-650.

Benedict L. H. & Gould R. D. 1996 Towards better uncertainty estimates in turbulent statistics. *Exps. Fluids* **22**, 129-136.

Besnard D. C., Harlow F. H., Rauenzahn R. M. & Zemach, C. 1992 Turbulence transport equations for variable-density turbulence and their relationship to two-field models. *Los Alamos National Laboratory Report,* LAUR-12303.

Bruun H. H. 1995 *Hot-Wire Anemometry: Principles and Signal Analysis.* New York: Oxford University Press.

Chandrakeshar S. 1961 *Hydrodynamic and Hydromagnetic Stability.* New York: Dover.

Chassaing P., Antonia F., Anselmet L., Joly L., & Sarkar S. 2002 *Variable Density Fluid Turbulence*. Dordrecht, Netherelands: Kluwer Academic.

Chew Y. T. & Ha S. M. 1988 The directional sensitivities of crossed and triple hot-wire probes. *J. Phys. E: Sci. Instrum.* **21**, 613-620.

Cook A. W. & Dimotakis P. E. 2001 Transition stages of Rayleigh-Taylor instability between miscible fluids. *J. Fluid Mech.* **443**, 69-99.

Cook A. W., Cabot W. & Miller P. L. 2004 The mixing transition in Rayleigh-Taylor instability. *J. Fluid Mech.* **511**, 333-362

Danckwerts P. V. 1952 The definition and measurement of some characteristics of mixtures. *Appl. Sci. Res. A* **3**, 279-296.

Dimonte G. & Schneider M. 1996 Turbulent Rayleigh-Taylor instability experiments with variable acceleration. *Phys. Rev. E* **54**, 3740-3743.

Dimonte G. & Schneider M. 2000 Density ratio dependence of Rayleigh-Taylor mixing on sustained and impulsive acceleration histories. *Phys. Fluids* **12**, 304-321.

Dimonte G., Youngs D. L., Dimits A., Weber S., Marinak M., Wunsch S., Garasi C., Robinson A., Andrews M. J., Ramaprabhu P., Calder A. C., Fryxell B., Biello J., Dursi L., MacNeice P., Olson K., Ricker P., Rosner R., Timmes F., Tufo H., Young Y. N. and Zingale M. 2004 A comparative study of the turbulent Rayleigh-Taylor instability using high-resolution three-dimensional numerical simulations: The Alpha-Group collaboration. *Phys. Fluids* **16**, 1668-1693.

Fabris G. 1979 Conditional sampling study of the turbulent wake of a cylinder. Part 1. *J Fluid Mech.* **94**, 673-709.

Fabris G. 1983a Third-order conditional transport correlations in the two-dimensional turbulent wake. *Phys. Fluids* **26**, 423-427.

Fabris G. 1983b Higher-order statistics of turbulent fluctuations in the plane wake. *Phys. Fluids* **26**, 1437-1445.

Frota M. N. & Moffat R. J. 1983 Effect of combined roll and pitch angles on triple hot-wire measurements of mean and turbulence structure. *DISA Info* **28**, 15-23.

Gallier C. 1977 Measurements of air velocity by means of a triple hot-wire probe. *DISA Info* **21**, 16-20.

Gull S. F. 1975 The X-ray, optical and radio properties of young supernova remnants. *Mon. Not. Roy. Astron. Soc.* **171**, 263-278.

Harion J. L., Marinot M. F. & Camano B. 1996 An improved method for measuring velocity and concentration by thermo-anemometry in turbulent helium-air mixtures. *Exp. Fluids* **22**, 174-182.

Hishida M. & Nagano Y. 1978 Simultaneous measurements of velocity and temperature in nonisothermal flows. *Trans. ASME J. Heat Transfer* **100**, 340-345.

Jacobs J. W. & Catton I. 1988 3-Dimensional Rayleigh-Taylor instability. 2. Experiment. *J Fluid Mech.* **187**, 353-371.

Jorgensen F. E. 1971 Directional sensitivity of wire and fibre-film probes. *DISA Info* **11**, 31-37.

Kavence G. & Oka S. 1973 Correcting hot-wire readings for influence of fluid temperature variations. *DISA Info* **15**, 21-24.

King L. V. 1914 On the convection of heat from small cylinders in a stream of fluid: determination of the convection constants of small platinum wires with applications to hot-wire anemometry. *Phil. Trans. Royal Soc. A* **214**, 373-432.

Kline S. J. & McClintock F. A. 1953 Describing uncertainties in single-sample measurements. *Mech. Eng.* **75**, 3-8.

Koop G. K. 1976 Instability and turbulence in a stratified shear layer. PhD Dissertation, University of Southern California.

Kraft W., Andrews M. J., Ramaprabhu P. & Snider D. 2005 Visualization of the Rayleigh-Taylor instability. *J. Flow Vis. & Image Proc.* **12**, 1-13.

Kraft W. & Andrews M. J. 2006 Experimental investigation of unstably stratified buoyant wakes. *Trans. ASME J. Fluids Eng.* **128**, 488-493.

LaRue J. C. & Libby P. A. 1977 Measurements in the turbulent boundary layer with slot injection of helium. *Phys. Fluids* **20**, 192-202.

LaRue J. C. & Libby P. A. 1980 Further results related to the turbulent boundary layer with slot injection of helium. *Phys. Fluids* **23**, 1111-1118.

Lindl J.D. 1998 *Inertial Confinement Fusion: The Quest for Ignition and Energy Gain Using Indirect Drive.* New York: AIP Press.

Livescu D. & Ristorcelli J. D. 2007 Buoyancy-driven variable density turbulence. *J. Fluid Mech.* **591**, 43-71.

McQuaid J. & Wright W. 1973 The response of a hot-wire anemometer in flows of gas mixtures. *Int. J. Heat Mass Transfer* **16**, 819-828.

Moffat R. J. 1988 Describing the uncertainties in experimental results. *Exp. Thermal and Fluid Sci.* **1**, 3-17.

Mueschke N. J., Andrews M. J. & Schilling O. 2006 Experimental characterization of initial conditions and spatio-temporal evolution of a small-Atwood-number Rayleigh-Taylor mixing layer. *J. Fluid Mech.* **567**, 27-63.

Mueschke N. J., Schilling O., Youngs D. L. & Andrews M. J. 2008 Measurements of molecular mixing in a high Schmidt number Rayleigh-Taylor mixing layer. *J. Fluid Mech.* (submitted).

Mydlarski L. 2003 Mixed velocity-passive scalar statistics in high-Reynolds-number turbulence. *J. Fluid Mech.* **475**, 173-203.

Panchapakasen N. R. & Lumley J. L. 1993 Turbulence measurements in axisymmetric jets of air and helium. Part 2 Helium Jet. *J. Fluid Mech.* **246**, 225-247.

Ramaprabhu P. & Andrews M..J. 2004 Experimental investigation of Rayleigh-Taylor mixing at small Atwood numbers. *J. Fluid Mech*. **502**, 233-271.

Ristorcelli J. R. & Clark T. T. 2004 Rayleigh-Taylor turbulence: self-similar analysis and direct numerical simulations. *J. Fluid Mech.* **507**, 213-253.

Pope S. B. 2000 *Turbulent Flow.* Cambridge, UK: Cambridge University Press.

Read K. I. 1984 Experimental investigation of turbulent mixing by Rayleigh-Taylor instability. *Physica D* **12**, 45-58.

Rose W. C. 1973 The behavior of a compressible turbulent boundary layer in a shock-wave-induced adverse pressure gradient. PhD Dissertation, University of Washington.

Snider, D. M. & Andrews M. J. 1994 Rayleigh-Taylor and shear driven mixing with an unstable thermal stratification. *Phys. Fluids* **6**, 3324-3334.

Steinkamp M. J. 1995 Spectral analysis of the turbulent mixing of two fluids. PhD Dissertation, University of Illinois.

Steinkamp M. J., Clark T. T., & Harlow F. H. 1999 Two-point description of two-fluid mixing – I. model formulation. *Int. J. Multiphase Flow* **25**, 599-637.

Vukoslavcevic P. V., Radulovic I. M. & Wallace J. M. 2005 Testing of a hot- and cold-wire probe to measure simultaneously the speed and temperature in supercritical CO_2 flow. *Exp. Fluids* **3**, 703-711.

Wilson P. N. & Andrews M. J. 2002 Spectral measurements of Rayleigh-Taylor mixing at low-Atwood number. *Phys. Fluids A* **14**, 938–945.

Wygnanski I. & Fiedler H. E. 1970 The two-dimensional mixing region. *J. Fluid Mech.* **41**, 327-361.

Youngs D. L. 1984 Numerical simulation of turbulent mixing by Rayleigh-Taylor instability. *Physica D* **12**, 32-44.

Youngs D. L. 1989 Modelling turbulent mixing by Rayleigh-Taylor instability. *Physica D* **37**, 270-287.

Youngs D. L. 1991 Three-dimensional numerical simulation of turbulent mixing by Rayleigh-Taylor instability. *Phys. Fluids A* **3**, 1312-1320.

APPENDIX A

HELIUM AND AIR HOT-WIRE CALIBRATION

To accurately determine velocity measurements inside the mixing layer (varying gas species) a calibration must be performed over the expected velocity and concentration range of helium and air. Therefore, if the mixture of helium and air passing the three-wire probe can be identified, the appropriate velocity response can be utilized. The method for calibrating the three-wire probe is similar to that of the single-wire probes used by Banerjee (2006).

Instead of using the channel itself to calibrate the probes, which can be tedious and expensive (helium costs for the large channel), a section of pipe connected to a proportioner meter (Model # P21A1-BA2, *Aalborg Corp.*), which controls gas flow rates up to 70 L/min through both the air and helium rotameters, is used for hot-wire calibration. In addition to calibration of the hot-wire probes, this configuration allows the calibration of the proportioner meter to be verified. A schematic of the calibration setup is shown in Figure A.1 (a). The inner diameter of the pipe is 1.25 in and the distance between the two clear acrylic sections is 36 in. This length allows for timing injected fog with adequate accuracy to independently determine volumetric flow rates through the pipe setup. The pipe is used as a small wind tunnel, consisting of plastic PVC tubing and restrictive wire meshes to keep the velocity profile uniform and reduce boundary layers. Fog is injected through a hole near the inlet of the pipe into the stream, where it can be viewed through two clear acrylic sections for determining volumetric flow rates. The end of the pipe calibration setup, far downstream of the measurement section, is angled down to prevent the heavier ambient air from flowing back into the end of the pipe when proportioning relatively lighter mixtures of helium and air. Once the calibration of the

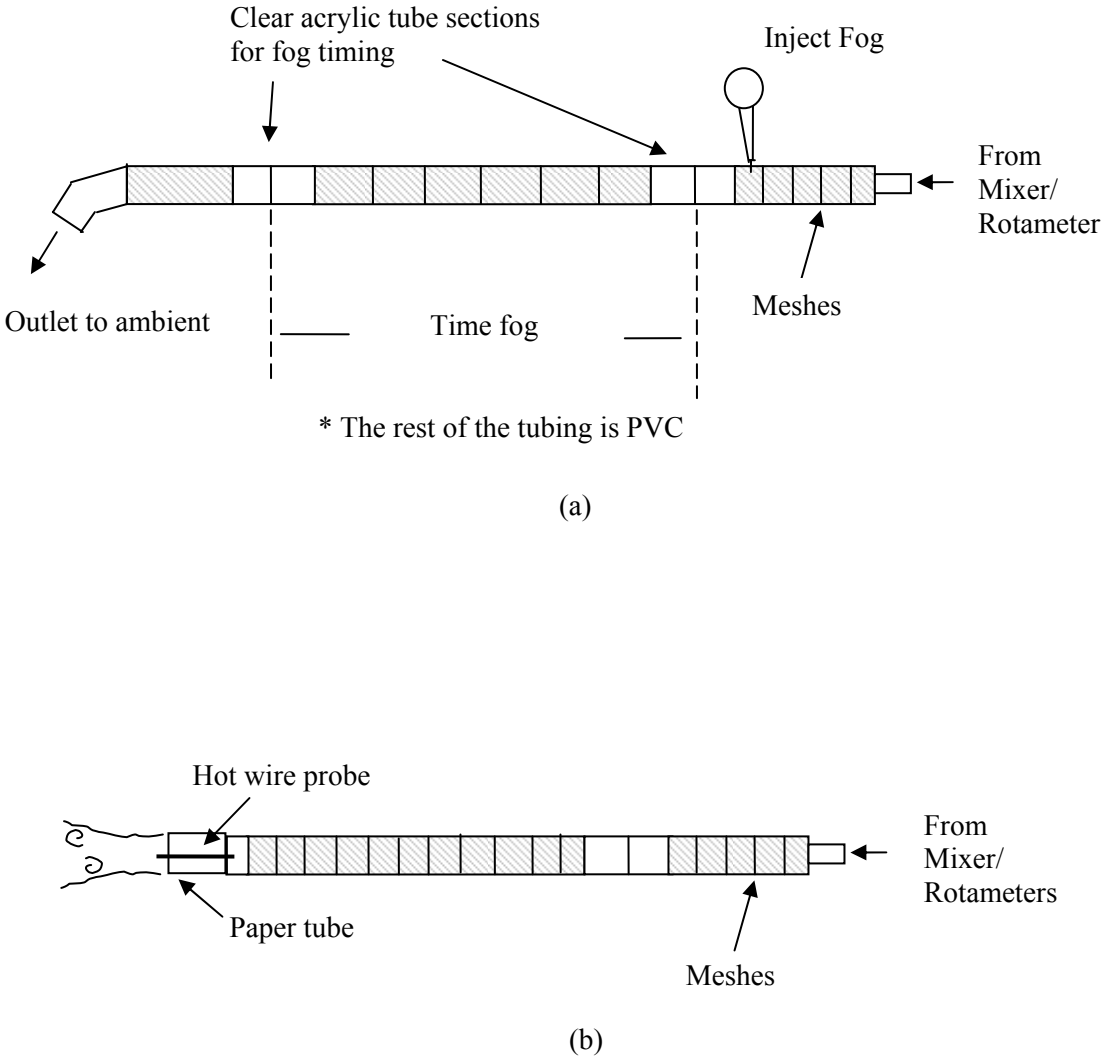

Figure A.1. (a) Helium / air calibration setup for verifying the use of the helium and air proportioner. (b) Calibration setup modified to insert hot-wire probes for calibration for helium and air over the desired velocity ranges.

proportioner meter has been determined, the hot-wire probes can be calibrated through a simple modification of this setup. During calibration of the proportioner the actual air and helium volumetric flow rates were found to be 20% greater and 15% less than the manufacturer's published calibration curves, respectively. A schematic of the calibration of the hot-wire probes in this setup is shown in Figure A.1 (b). The hot-wire probe is placed inside the center of the pipe after the final wire mesh. To safely place the hot-wire probes inside the pipe the angled end of the pipe is removed, but a mechanism is needed to prevent a gravity backflow from altering the flow inside the pipe. The solution implemented here is to extend the length of the pipe, encapsulating the hot-wire probe inside the setup by wrapping a paper tube around the pipe and probe body once it is placed inside. To prevent the heavy ambient air from retreating back into the pipe where the measurement is to take place, the bottom of the paper tube is cut away. In this way the helium/air mixture can flow out (protected by the paper tube); however, there is no bottom surface to support the heavier air traveling back into the calibration pipe. Using a calibration setup of this configuration allows calibration of the probes over a range of downstream velocities of approximately 0.3 – 2.3 m/s in concentrations from pure air to pure helium.

The scaling of King's law has been utilized to linearize the calibration data. It is advantageous to represent the calibration data as a three-dimensional surface fit, which will allow the analytical expression to be solved algebraically for the hot-wire effective velocity. This procedure is similar to the fitting methods of Banerjee (2006), *TABLE CURVE 3-D* is used to fit the calibration data for each hot-wire sensor. The surface fit for the calibration data of wire 1 is shown in Figure A.2. The analytical expression for the surface fit is

$$E^2 = \frac{a + bU_{eff}^{1/2} + cf_{he} + df_{he}^{2} + ef_{he}^{3}}{1 + gU_{eff}^{1/2} + hf_{he} + if_{he}^{2} + jf_{he}^{3}} \quad . \tag{A.1}$$

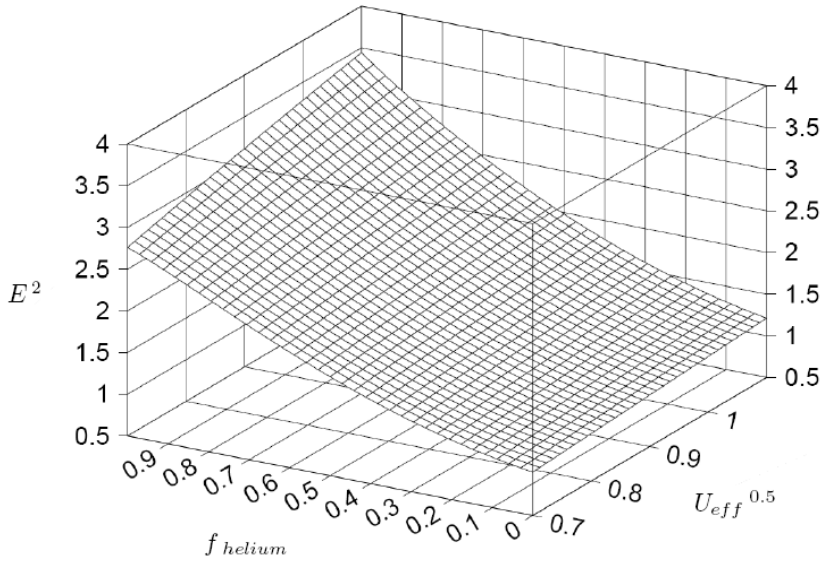

Figure A.2. A three-dimensional surface fit of the helium and air calibration for the hot-wire probe.

When solved for the sensor effective velocity, the expression becomes

$$U_{eff} = \left[\frac{a + c f_{he} + d f_{he}^2 + e f_{he}^3 - E^2 \left(1 + h f_{he} + i f_{he}^2 + j f_{he}^3\right)}{g E^2 - b} \right]^2 . \tag{A.2}$$

In this manner, the sensor effective velocity, U_{eff}, can be found directly given the square of the hot-wire voltage and the volume fraction of helium passing the probe at any given instant. Using a fit for each wire sensor allows for all three velocity components to be determined instantaneously inside the gas mixture. This method proved successful in most instances. However, there were cases where three-dimensional surface fits were not determined within desirable accuracy. In these situations it is preferable to use a linear interpolation with the linearized calibration data. Linear interpolation of the data using King's law scaling is found to be a more robust method for determining U_{eff} from the anemometer voltages and temperature marker. However the three-dimensional surface fits are useful in examining the hot-wire sensitivities when evaluating uncertainties for the technique.

APPENDIX B

COLD-WIRE ANEMOMETRY

Temperature measurements in the gas channel facility are obtained using a cold-wire anemometer. As stated before, the CTA is used to sense the fluid velocity. However, the CCA anemometer (in contrast with the CTA anemometer) neglects the resistive heating of the wire by using only small currents. Therefore, the wire resistance, R_w, can be related linearly to the wire temperature through

$$R_w(t) = R_{ref}\left[1 + \alpha\left(T_{wire}(t) - T_{ref}\right)\right], \tag{B.1}$$

where R_{ref} is the reference resistance, T_{ref} is the reference temperature, α is temperature coefficient of resistivity, and T_{wire} is the wire temperature (LaRue 1975). Output voltage, E, from the CCA circuit is subsequently related to the changes in wire resistance and fluid temperature by,

$$E(t) = R_{ref} I\left[T_{wire}(t) - T_{ref}\right], \tag{B.2}$$

where I is the current through the wire. The CCA anemometer is from *AA Lab Systems*. The wire probes used with the CCA anemometer are standard single-wire probes from *Dantec Dynamics* with a 5 micron diameter Pt-T wire. Calibration of the single-wire probe for temperature is straightforward. The response of the probe and anemometer is measured in the channel while heating the air flow to various temperatures. The air temperature is independently measured with a handheld thermocouple device. A linear fit can then be found for the calibration data, where the fit coefficients describe the wire response to temperature. An example of a calibration performed in this way is shown in Figure B.1.

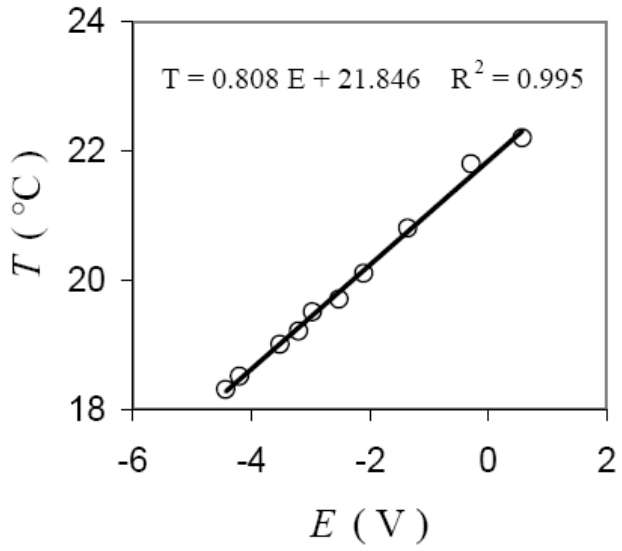

Figure B.1. Calibration fit for determining the relationship between voltage and temperature for the cold-wire anemometer.

APPENDIX C

FLUID MARKING BY TEMPERATURE

C.1 Conversion of temperature to volume fraction and density

This appendix provides a more complete description of the relationship between fluid marking by temperature and the measurement of fluid volume fraction (concentration). The following notation and subscripts will be used:

f_m mass fraction

f_v volume fraction

1 subscript for top stream

2 subscript for bottom stream

mix subscript for mixing layer measurement

The procedure for determining fluid volume fraction from temperature proceeds through the following steps:

1) Determine stream 1 and 2 specific heats

For stream 1,

$$c_{p,1} = c_{p,air} \tag{C.1}$$

For stream 2,

$$f_{m-air,2} = \frac{\dot{m}_{air,2}}{\dot{m}_{air,2} + \dot{m}_{he,2}} \tag{C.2}$$

where

$$f_{m-he,2} = 1 - f_{m-air,2} \tag{C.3}$$

The specific heat of stream 2 is determined on a mass fraction basis of its constituent fluids of air and helium, such that

$$c_{p,2} = (f_{m-air,2})c_{p,air} + (f_{m-he,2})c_{p,he} \tag{C.4}$$

2) Now determine instantaneous mass fractions of streams 1 or 2

From an energy balance of the two streams,

$$\dot{Q}_{mix} = \dot{Q}_1 + \dot{Q}_2 \tag{C.5}$$

$$\dot{m}_{mix} c_{p,mix} T_{mix} = \dot{m}_1 c_{p,1} T_1 + \dot{m}_2 c_{p,2} T_2 \ , \tag{C.6}$$

where

$$c_{p,mix} = f_{m,1} c_{p,1} + f_{m,2} c_{p,2} \text{ and } f_{m,1} + f_{m,2} = 1 \ . \tag{C.7}$$

Solving for $f_{m,2,}$

$$f_{m,2}(t) = \left[1 + \frac{c_{p,2}}{c_{p,1}} \frac{T_2(t) - T_{mix}(t)}{T_{mix}(t) - T_1(t)} \right]^{-1} \tag{C.8}$$

T_1, T_2, and T_{mix} (cold wire) are the instantaneously measured temperatures. This yields a time trace of mass fraction, $f_{m,2}$. The pure fluid specific heats are assumed to be constant (effect of temperature variation is negligible on specific heat).

3) Determine instantaneous volume fractions and densities

$$f_{v,2}(t) = \frac{\rho_1}{\rho_1 - \rho_2 + \dfrac{\rho_2}{f_{m,2}(t)}} \ . \tag{C.9}$$

The inlet stream fluid densities are evaluated at their respective average inlet temperatures. The thermocouple traces are used to accurately determine $f_{m,2}$ as the inlet temperatures (T_1,T_2) vary. The volume fraction of fluid 1 is then determined as

$$f_{v,1}(t) = 1 - f_{v,2}(t) \tag{C.10}$$

Finally, the fluid density is determined using the measured fluid volume fractions and known inlet stream densities such that

$$\rho_{mix}(t) = f_{v,1}(t)\,\rho_1 + f_{v,2}(t)\,\rho_2 \quad . \tag{C.11}$$

C.2 Determining the temperature difference between inlet streams

The use of temperature as a fluid marker has been verified, and the ability to measure temperature inside the gas channel has been demonstrated using a cold-wire anemometer. However, the required temperature difference between the two inlet streams must be selected. The required temperature difference, ΔT, between inlet streams to accurately use temperature as a marker is dependent on the cold-wire temperature resolution, the ratio of fluid specific heats, desired volume fraction uncertainty, and effects on hot-wire performance. Similar to the thermocouple, the cold-wire diagnostic measures temperature to the nearest 0.01°C. However, temperature uncertainty can propagate into the volume fraction measurement. It is logical to assume that as ΔT is increased between the two inlet streams (the temperature scale is stretched), the resulting volume fraction uncertainty will decrease.

There are limitations to selecting an arbitrarily large temperature difference, as increasing ΔT between the two inlet streams is detrimental to the hot-wire diagnostic, and alternatively fluid densities can be changed by a large ΔT. With a large ΔT, the effect of temperature on the fluid density may be too large to neglect, creating an additional complexity for the experiment. An $A_t = 0.5$ case will be used as an example. At $A_t = 0.5$ a temperature difference of 5 ^{o}C would be acceptable. This allows for adequate temperature separation of

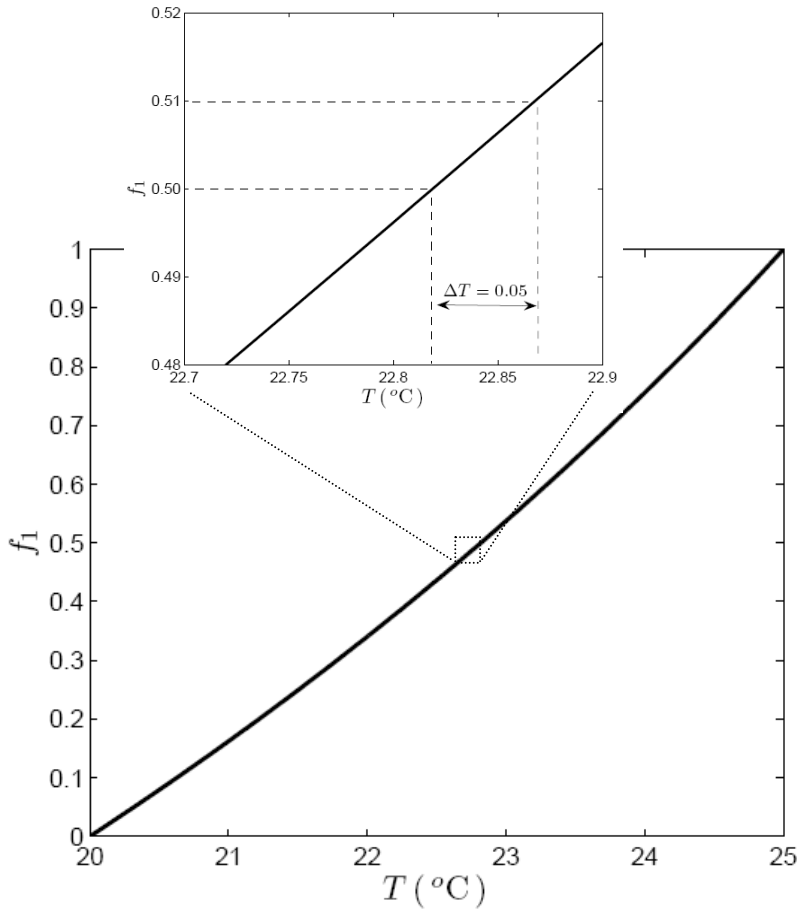

Figure C.1. Volume fraction of the bottom stream as a function of temperature for $A_t = 0.5$ with $\Delta T = 5$ °C, where $T_1 = 20$ °C and $T_2 = 25$ °C. (Graphical representation of the two equations presented earlier in this section.)

volume fractions to achieve high resolution volume fraction measurements, and the variation of ρ_1 and ρ_2 due to temperature change in the center of the mixing layer, $f_{v,1} = 0.5$ (only 2.5 °C change from their respective inlet temperatures) is ~ 3.5%. A demonstration of the dependency of the volume fraction measurement on the resolution of the temperature measurement is shown in Figure C.1 for $A_t = 0.5$.

C.3 Temperature correction of the hot-wire anemometer

By varying fluid temperature, the hot-wire response will deviate from the calibrated response as the temperature conditions for convective heat transfer between the wires and fluid have changed. A temperature correction will be applied to the raw hot-wire voltages. The temperature correction used is described by Kanevce and Oka (1973) as

$$E_{corr}^2\left(T_{ref}\right) = E^2(T)\left(\frac{T_{wire} - T_{ref}}{T_{wire} - T}\right), \tag{C.12}$$

where the fluid temperature, T, exposed to the hot-wires is supplied via the cold-wire, and the calibration reference temperature is T_{ref}. This has proven effective in current measurements to account for variation in temperature between calibration and experiments. More sophisticated approaches to temperature correction of the hot-wire voltages have been described by Benjamin (2002) and Dijk (2004), but it is not necessary for the small temperature fluctuations in these experiments.

A simple demonstration of the temperature correction is shown in Figure C.2. The air stream in the gas channel is heated above room temperature by approximately 10 °C using the kerosene heater. The heater is then removed. As air moves through the gas channel it begins to cool. During this time the air velocity is held constant. While the air stream cools, both the hot-wire anemometer (velocity measurement) and the cold-wire anemometer (temperature

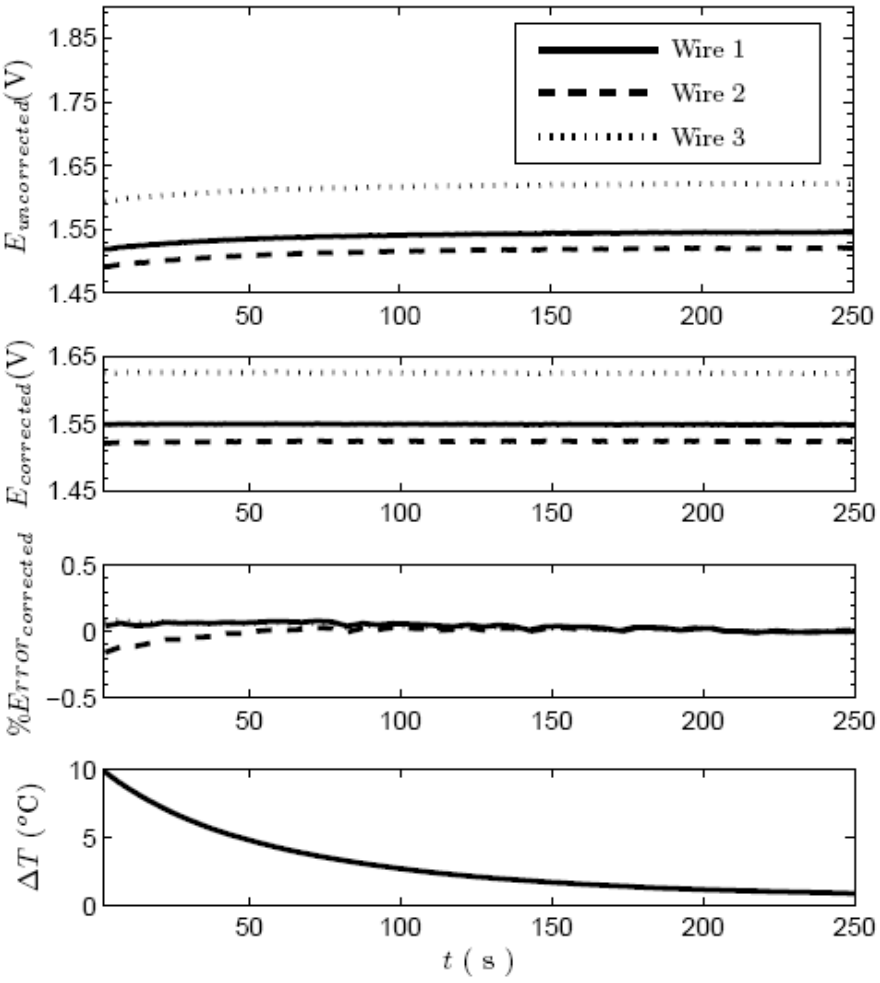

Figure C.2. Demonstration of the use of a temperature correction applied to the three-wire hot-wire probe output voltages while recording a constant velocity in a non-isothermal flow.

measurement) are placed in close proximity and simultaneously sampled. If this was an isothermal environment, the hot-wire voltages would remain constant during this demonstration, since the air velocity is held constant. Since the air temperature is allowed to change, the hot-wire response is not constant. The effect on the hot-wire voltages and response is apparent in the uncorrected hot-wire voltages of Figure C.2 (should be constant). Using the correction procedure described allows accurate measurements to be obtained, even in the non-isothermal environment.

C.4 Measuring temperature inside the mixing layer

Before simultaneous measurements are made with the hot-wire and cold-wire anemometer, it is advantageous to verify initial measurements with the cold-wire anemometer alone. Temperature is used as a fluid marker in the helium-air flow ($Pr \sim 1$, $Sc \sim 1$). A kerosene heater creates the necessary temperature difference for the inlet streams. For the described mixing layer measurement, an $A_t = 0.036$ with a mean velocity of $U_m = 0.50$ m/s and a $\Delta T = 3$ °C will be used. Measurement of temperature within the mixing layer is then performed using a CCA circuit (cold-wire) to identify the composition of passing fluid. In addition, it is necessary to know the inlet stream temperatures to correctly identify the composition inside the mixing layer. To independently determine the pure stream temperatures (i.e. accurately account for free stream temperature variation due to both the heater and helium) thermocouples are placed upstream. The cold-wire and thermocouples are sampled simultaneously to measure mixing layer and free stream temperatures. In the free stream, the fast time response of the cold wire (~ 1 kHz for $A_t = 0.5$) is not necessary (i.e. laminar flow); therefore, the limited time response of thermocouples is adequate.

(a)

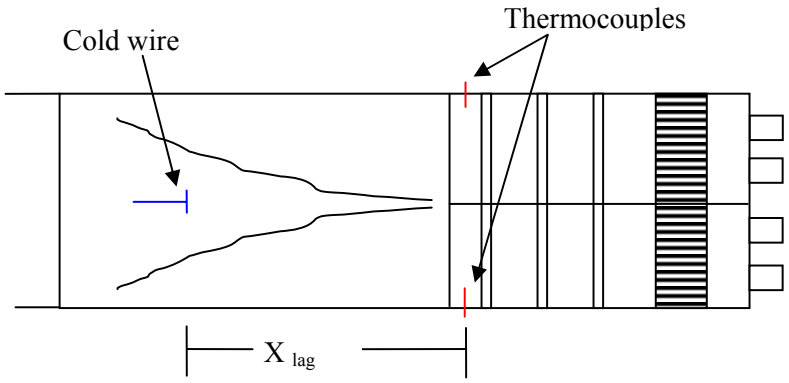

(b)

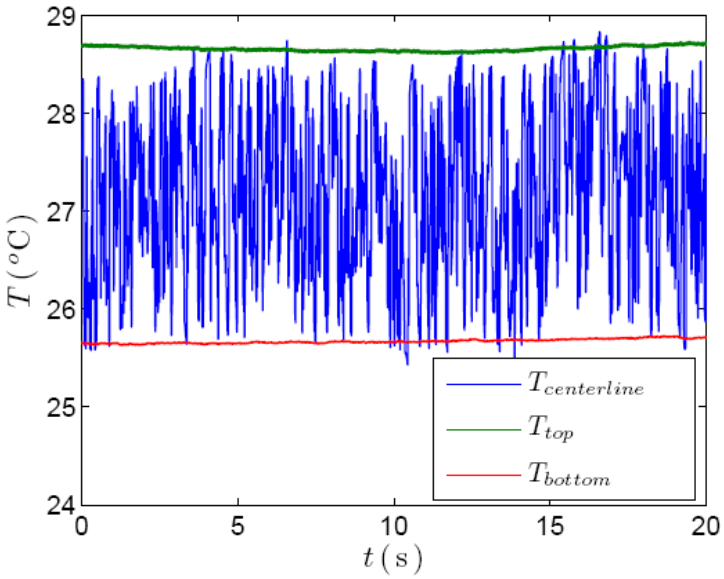

Figure C.3. (a) Placement of thermocouples and cold-wire in the channel and mixing layer. (b) Selection of the cold-wire temperature trace at the centerline of the mixing layer with simultaneous inlet stream measurements via thermocouples for a low Atwood number experiment.

A_t	0.036
U_m	0.50
x	1.5
ΔT	3
$f_{v,1}$	0.50
θ	0.70

Table C.1. Summary of results from temperature marker validation

The arrangement of the temperature diagnostic is shown in Figure C.3 (a). Thermocouples are placed in a fixed location for connectivity considerations, 10 cm upstream of the end mesh. The cold-wire is placed at the desired downstream location inside the mixing layer, in this case 1.5 m downstream. To account for the time lag between temperature measurement at the two locations the lag is computed, $t_{lag} = X_{lag} / U$. This time lag is then used to reconcile the cold-wire and thermocouple traces. Shown in Figure C.3 (b) are simultaneous measurements of the cold-wire and thermocouples for a low Atwood experiment run after the lag has been used to reconcile the three traces. Experimental results using the above analysis are shown in the Table C.1. These results are determined from the temperature trace shown previously. The described technique is consistent with previous water channel (Ramaprabhu & Andrews 2004) and gas channel (Banerjee 2006) results.

C.5 Simultaneous sampling

Care must be taken when performing simultaneous sampling of the CTA, CCA, and thermocouples. Although each diagnostic is "held" simultaneously in the CA-1000 junction box, each of the six channels is sampled serially by the data acquisition card. If subsequent signals are not of the same order of magnitude, the sample circuit may not settle between measurement of each channel by the data acquisition card. The result is "cross talk" between two channels. Due to the larger voltage magnitudes of the CCA, it was found that when the CCA was sampled before a hot-wire, the hot-wire signal would be incorrectly measured. This is illustrated in Figure C.4, where the hot-wire voltage traces are sampled in a constant velocity stream with increasing fluid temperature. As can be seen in Figure C.4, wire 1 is influenced by the behavior of the CCA. During this procedure it was discovered that the sampling order was not determined

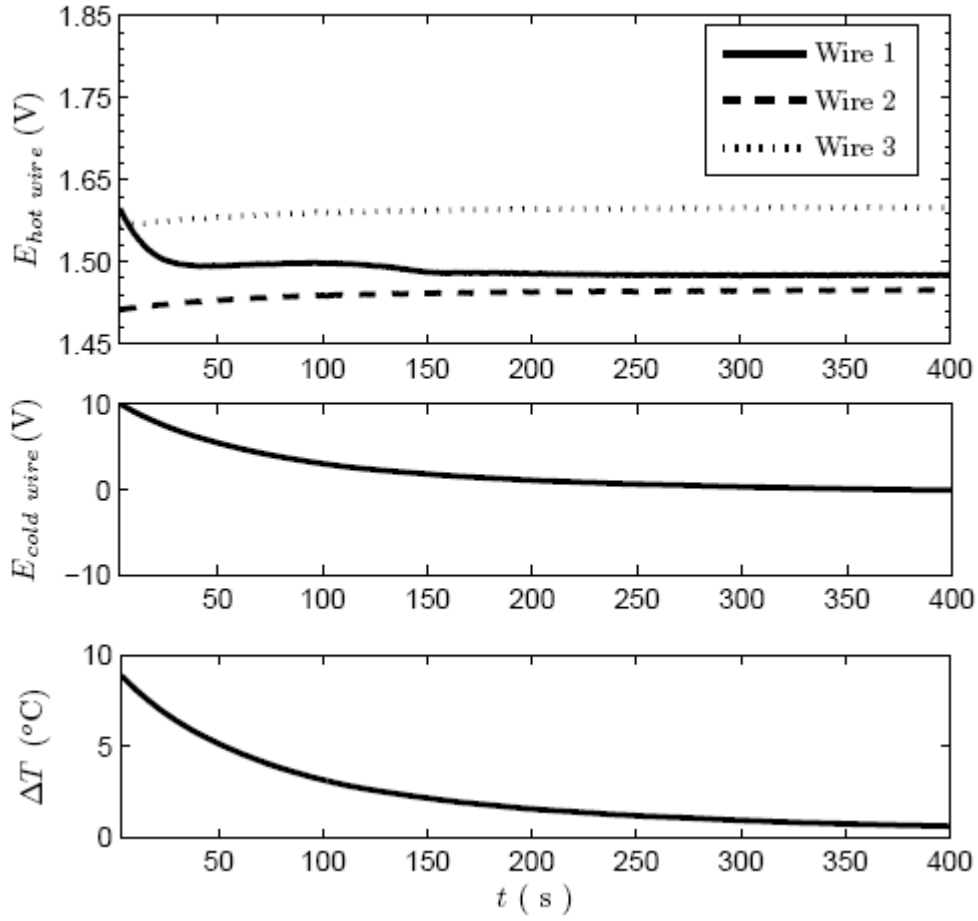

Figure C.4. Demonstration of the difficulty of simultaneous sampling all six data channels. The hot-wires and CCA are placed in a uniform, constant velocity with varying fluid temperature. The CCA causes a "cross talk" with hot-wire 1.

by the channel number on the CA-1000 junction box, but instead by the order the channels are setup in the data acquisition software. To resolve "cross talk" caused by the different orders of magnitude of the voltage signals, the CCA was sampled last of the six channels. Additional "cross talk" issues can occur with the E-type thermocouples due to the small voltage magnitude of the signal. Therefore, a hardware amplification of 800 is applied on the CA-1000 junction box. The amplified signal is then corrected to its original magnitude for conversion to temperature in a *Labview* utility.

APPENDIX D

HOT-WIRE ANALYSIS AND DATA REDUCTION

The first relationship utilized in the reduction of hot-wire voltages (E_1, E_2, E_3) is found by equating the previously mentioned King's law to the Jorgensen equation for each wire sensor

$$\left(\frac{E_1^2 - A_1}{B_1}\right)^{2/n_1} = U_{eff,1}^2 = k_1^2 U_w^2 + V_w^2 + h_1^2 W_w^2 \tag{D.1}$$

$$\left(\frac{E_2^2 - A_2}{B_2}\right)^{2/n_2} = U_{eff,2}^2 = h_2^2 U_w^2 + k_2^2 V_w^2 + W_w^2 \tag{D.2}$$

$$\left(\frac{E_3^2 - A_3}{B_3}\right)^{2/n_3} = U_{eff,3}^2 = U_w^2 + h_3^2 V_w^2 + k_3^2 W_w^2 \,. \tag{D.3}$$

The Jorgensen equation relates the wire-coordinate system velocities to the wire effective velocity, normal to each probe. This is accomplished using pitch and yaw coefficients (*h, k*) based on the probe geometry. These are provided by *Dantec Dynamics* and are based on their design of the probe. Chew and Ha (1988) directly measured the pitch and yaw coefficients for a 55P91 probe and suggest values h = 1.01 and k = 0.20 for optimum performance. If a single-species gas was being used for this experiment, the above analysis described by Bruun (1995) could be used directly. The left hand sides of (D.1)-(D.3), for application in the mixing layer, are replaced with the helium/air hot-wire calibration. The measured voltage, E, and the concentration of helium, $f_{v,he}$, are used to linearly interpolate the effective velocity, U_{eff}, from the calibration data for each wire. The right hand side of the equations in matrix form is

$$\begin{bmatrix} U^2_{eff,1} \\ U^2_{eff,2} \\ U^2_{eff,3} \end{bmatrix} = \begin{bmatrix} k_1^2 & 1 & h_1^2 \\ h_2^2 & k_2^2 & 1 \\ 1 & h_3^2 & k_3^2 \end{bmatrix} \begin{bmatrix} U_w^2 \\ V_w^2 \\ W_w^2 \end{bmatrix}. \tag{D.4}$$

Solving for the wire-coordinate system velocities,

$$\begin{bmatrix} U_w^2 \\ V_w^2 \\ W_w^2 \end{bmatrix} = \begin{bmatrix} k_1^2 & 1 & h_1^2 \\ h_2^2 & k_2^2 & 1 \\ 1 & h_3^2 & k_3^2 \end{bmatrix}^{-1} \begin{bmatrix} U^2_{eff,1} \\ U^2_{eff,2} \\ U^2_{eff,3} \end{bmatrix}. \tag{D.5}$$

If the instantaneous velocity vector is in the positive quadrant of the wire-coordinate system, all the wire-coordinate system velocity components are positive and the direction is therefore known (i.e. there is an acceptance cone for the instantaneous velocity vector in order to know the correct, unique solution for the velocity components). Generally, for velocity components to lie in the acceptance cone, the global *U*-velocity must be much larger than both *V* and *W*.

Now that the direction of the velocity vector in the wire-coordinate system is assumed to be in the positive quadrant, it is no longer ambiguous and U_w^2, V_w^2, W_w^2 can simply be reduced to $(+)U_w$, $(+)V_w$, and $(+)W_w$. This reduces a non-linear system of equations in terms of the square of velocities into a linear system of equations which can be solved through matrix multiplication. At this point, the instantaneous wire-coordinate system velocity components are known. Using direction cosines, these components can be transformed into the global, lab-coordinate system. The *Dantec* 55P91 probe uses the following direction cosine matrix,

$$[N] = \begin{bmatrix} \cos(45)\cos(35.3) & \cos(45)\cos(35.3) & \cos(54.7) \\ -\cos(45) & -\cos(45) & 0 \\ -\cos(45)\sin(35.3) & -\cos(45)\sin(35.3) & \cos(35.3) \end{bmatrix}. \tag{D.6}$$

The global velocities can now be solved using matrix multiplication,

$$\begin{bmatrix} U \\ V \\ W \end{bmatrix} = [N] \begin{bmatrix} U_w \\ V_w \\ W_w \end{bmatrix}. \tag{D.7}$$

An instantaneous velocity vector has now been determined and the process can be repeated for as many measurements as necessary.

The acceptance cone assumption has been checked for the limited measurements attempted so far using the three-wire probe, by solving the non-linear system of equations,

$$\begin{bmatrix} U_w^2 \\ V_w^2 \\ W_w^2 \end{bmatrix} = \left\{ [N]^{-1} \begin{bmatrix} U \\ V \\ W \end{bmatrix} \right\}^2, \tag{D.8}$$

where positive values of U_w, V_w, W_w are not assumed. Instead a non-linear, Newton-Raphson technique is used to iteratively solve the equations using only the initial guesses $U=U_{avg}$, $V=0$, and $W=0$, where U_w^2, V_w^2, W_w^2 have already been determined as described earlier. The same velocity traces have been calculated as with the simpler Bruun method, however consuming significantly greater computer resources. Therefore, the Bruun method will be used as the primary solution method.

A Newton-Raphson solver has been incorporated into the analysis as a regular check of the Bruun method results. The output velocities from the Bruun method are input as initial guesses into the Newton-Raphson algorithm and checked for convergence. At low Atwood numbers (where the influences of helium on the hot-wire voltages is manageable) there are few, if any, discrepancies between the simplified Bruun method and the Newton-Raphson solutions.

However, at large Atwood numbers where large concentrations of helium are present, the Newton-Raphson solver is useful to identify solutions of the Bruun method that may be erroneous, occuring when the cold-wire and hot-wire probes sense different concentrations of helium. The Newton-Raphson solver allows these instances to be identified and removed from the calculated statistics. Additional considerations must be made when making measurements at large Atwood numbers due to the large concentrations of helium (associated large voltage sensitivites to helium) and the limited resolution of the combined cold-wire and three-wire probes. To increase the likelihood that both probes measure the same fluid, the raw data is filtered spectrally and through a window average to four times the probe spatial resolution. This is necessary to reduce the large errors introduced by helium at large Atwood numbers when the cold-wire and hot-wire do not sense the same fluid. Unfortunately, effects of helium on the hot-wire voltage, precludes measurements in the lower half of the mixing layer at $A_t = 0.6$, where the concentrations of helium sensed by the hot-wire probe are larger than at the centerline. The hot-wire voltage sensitivity to helium approximately doubles in this region, which would result in significant measurement errors with the current set of probes. A customized probe with an integrated three-wire hot-wire and cold-wire and smaller spatial resolution would alleviate this limitation.

APPENDIX E

AIR ONLY MEASUREMENTS USING A THREE-WIRE PROBE

To gain experience with the three-wire diagnostic and to verify the data reduction technique, shear layer experiments in air were performed. Two velocity profiles were measured across a shear layer following the experiments of Bell and Mehta (1990). The conditions for the two velocity profiles measured are shown in the Table E.1. The amount of shear between the top and bottom streams of the shear layer is defined as

$$U_s = U_h - U_l \tag{E.1}$$

and the mean velocity at the centerline of the shear layer is

$$U_c = \frac{(U_h + U_l)}{2}. \tag{E.2}$$

A Reynolds number for the shear layer is defined as

$$Re_w = \frac{U_s w}{\nu}, \tag{E.3}$$

where w is the shear layer width defined by the 10% and 90% velocity differences. A non-dimensional width is defined as

$$\zeta = \frac{(y - \bar{y})}{w}. \tag{E.4}$$

The conditions were to provide a comparison to the data of Bell and Mehta (1990), while attempting to achieve large Re_w. The mean velocity profiles of Figure E.1 collapse well and show the expected linear behavior within the shear layer. This is expected as the mean velocity profiles of Bell and Mehta begin to collapse in advance of the self-similar flow. As shown by Bell and Mehta, the asymmetry of the velocity fluctuation profiles is dependent on the initial

X (m)	1.6	1.9
U_s (m/s)	0.64	0.65
U_c (m/s)	1.01	1.03
Re_w	7500	9300

Table E.1. Shear layer parameters.

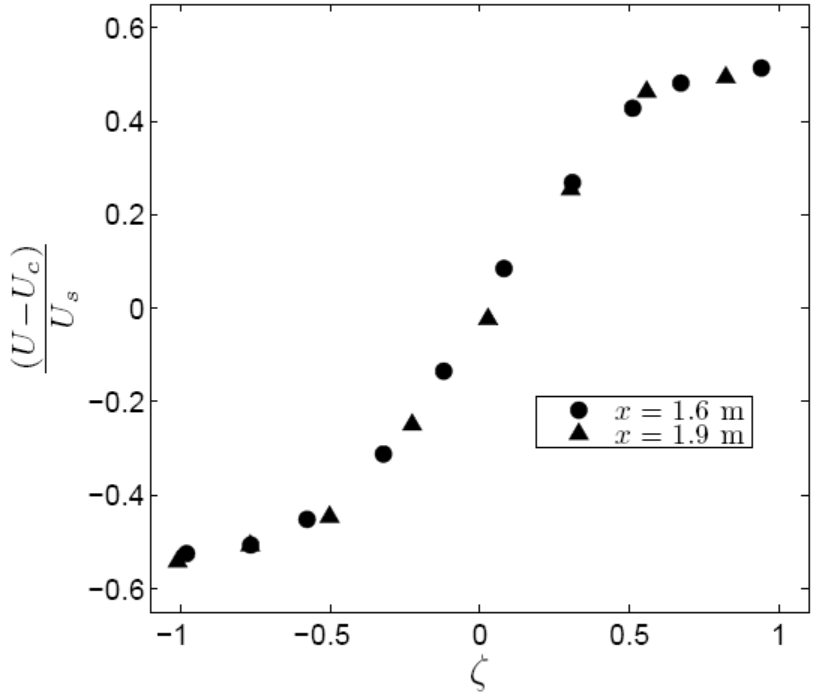

Figure E.1. Non-dimensional mean stream-wise velocity profile across a shear layer.

boundary layers of the two air streams. In many shear layer experiments, care is taken to manipulate these boundary layers to achieve the desired behavior.

The measured velocity fluctuation profiles are shown in Figure E.2. Similar asymmetry between the low-speed and high-speed sides of the shear layer are seen in Bell and Mehta (1990). As self-similarity is approached, the velocity fluctuation profiles should become symmetric. Although the downstream data (x = 1.9 m) is not yet symmetric, it approaches symmetry when compared with the upstream data (x = 1.6 m). Self-similarity should be found at $Re >> 10^4$. Therefore, similarity is not expected nor found for the two cases. Most shear layer experiments are performed at velocities an order of magnitude larger than can be achieved in the low-speed wind tunnel, thus allowing shear layer researchers to easily achieve $Re >> 10^4$. The peak magnitudes of the velocity fluctuations are reported in Table E.2; even though not yet self-similar, the peak magnitudes appear to be approaching the self-similar values reported by Bell and Mehta (1990). Overall good agreement is found between the measured shear layer velocity statistics and those obtained by Bell and Mehta.

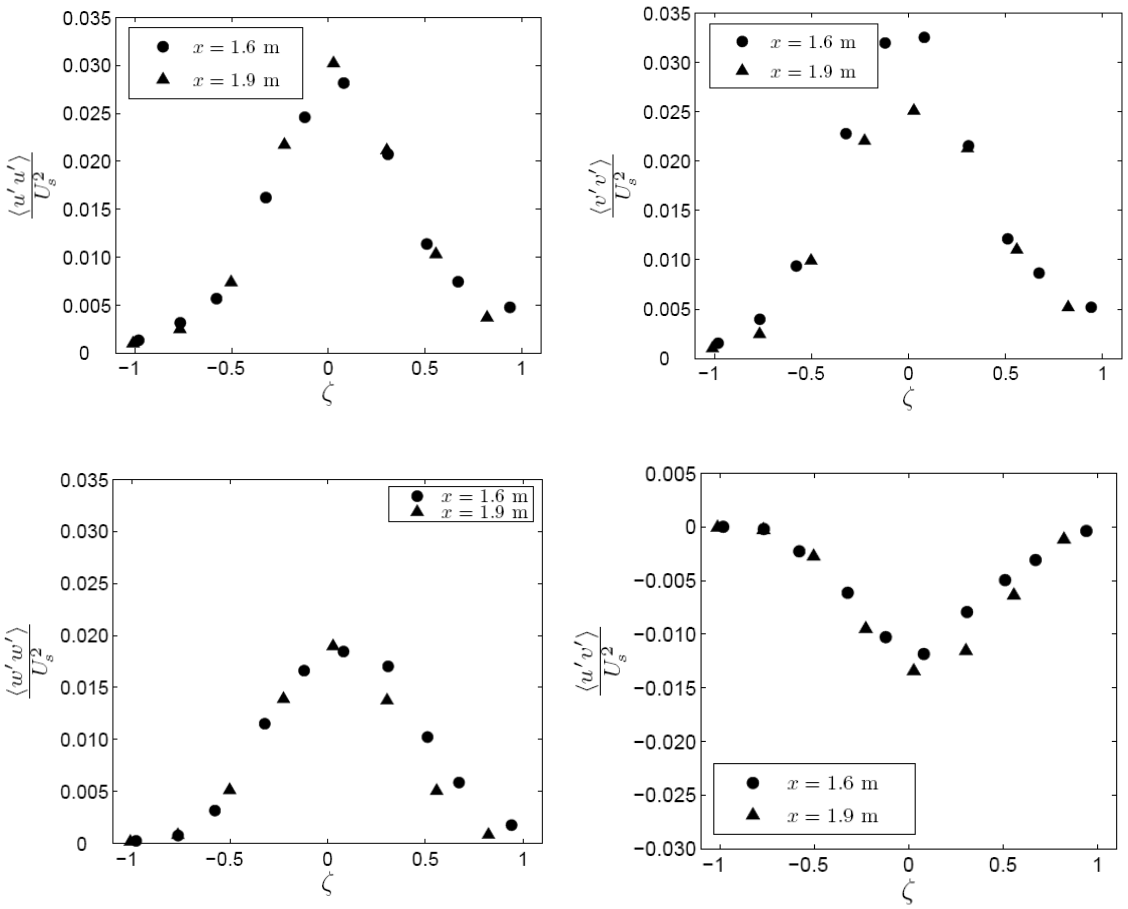

Figure E.2. Measured velocity fluctuations across the shear layer using the three-wire hot-wire anemometer.

Re_w	7500	9300	>> 10^4
$(u')^2/U_s^2$	0.028	0.030	0.032
$(v')^2/U_s^2$	0.033	0.025	0.019
$(w')^2/U_s^2$	0.019	0.020	0.022
$(u'v')/U_s^2$	-0.011	-0.012	-0.012

Table E.2. Measured peak velocity fluctuations inside the shear layer compared with the self-similar measurements of Bell and Mehta (1990) in the far right column.

APPENDIX F

UNCERTAINTY ANALYSIS

An uncertainty analysis illustrating the propagation of error through the data reduction calculations from hot-wire and cold-voltages to measurements of velocity and density has been performed. An overview of this analysis and the methodology for calculating uncertainty will be subsequently described. The analysis for determining uncertainties from data reduction will follow the methods described by Kline and McClintock (1953) and Moffat (1988). Additional uncertainties in the statistical turbulence measurements are determined from the methodology for uncertainty estimates in the sampling of random processes described by Benedict and Gould (1996).

F.1 Uncertainty of top (stream 1) and bottom (stream 2) stream fluid densities

The uncertainty of the fluid densities are dependent on the fluid temperatures of each stream and in the case of the bottom stream, additionally the helium metering system. The effect of temperature on the fluid densities from the introduced temperature difference between the fluid streams can be seen through fits of the equation of states for both helium and air. The uncertainties of the fluid temperatures (as the two fluids mix inside the mixing layer) are $w_{T_1} = w_{T_2} = (T_1 - T_2)/2$, where $(T_1 - T_2)/2$ is the maximum change in temperature in each stream fluid properties as it is molecularly mixed. Using these relationships, the uncertainties in the fluid densities following Kline and McKlintock (1953) are

$$w_{\rho_1} = w_{\rho_{air}} = \left[\left(\frac{\partial \rho_1}{\partial T_1} w_{T_1}\right)^2\right]^{1/2} = \left[(-8E-9)T_1^3 + (1.2E-6)T_1^2 - (4E-5)T_1 - 3.7E-3\right]\left(w_{T_1}\right) \quad \text{(F.1)}$$

$$w_{\rho_{he}} = \left[\left(\frac{\partial \rho_{he}}{\partial T_2} w_{T_2}\right)^2\right]^{1/2} = [(3.6E-6)\,T_2 - (6.4E-4)]\left(w_{T_2}\right) . \quad \text{(F.2)}$$

The density of the bottom stream (stream 2) is determined through the relationship

$$\rho_2 = \rho_{air} + \frac{\dot{m}_{he}}{U_m A_c}\left[1 - \frac{\rho_{air}}{\rho_{he}}\right] . \quad \text{(F.3)}$$

Therefore, the uncertainty of ρ_2 can then be determined as

$$w_{\rho_2} = \left[\left(\frac{\partial \rho_2}{\partial \rho_1} w_{\rho_1}\right)^2 + \left(\frac{\partial \rho_2}{\partial \dot{m}_{he}} w_{\dot{m}_{he}}\right)^2 + \left(\frac{\partial \rho_2}{\partial U_m} w_{U_m}\right)^2 + \left(\frac{\partial \rho_2}{\partial A_c} w_{A_c}\right)^2 + \left(\frac{\partial \rho_2}{\partial \rho_{he}} w_{\rho_{he}}\right)^2\right]^{1/2} \quad \text{(F.4)}$$

$$= \left[\begin{array}{l} \left\{\left(1 - \frac{\dot{m}_{he}}{U_m A_c \rho_{he}}\right) w_{\rho_{he}}\right\}^2 + \left\{\frac{1}{U_m A_c}\left(1 - \frac{\rho_{air}}{\rho_{he}}\right) w_{\dot{m}_{he}}\right\}^2 + \\ \left\{\frac{-\dot{m}_{he}}{U_m^2 A_c}\left(1 - \frac{\rho_{air}}{\rho_{he}}\right) w_{U_m}\right\}^2 + \left\{\frac{-\dot{m}_{he}}{U_m A_c^2}\left(1 - \frac{\rho_{air}}{\rho_{he}}\right) w_{A_c}\right\}^2 + \left\{\left(\frac{\dot{m}_{he}\rho_{air}}{U_m A_c \rho_{he}^2}\right) w_{\rho_{he}}\right\}^2 \end{array}\right]^{1/2} . \quad \text{(F.5)}$$

The additional uncertainties of w_{A_c}, w_{U_m}, and $w_{\dot{m}_{he}}$ were evaluated previously in the uncertainty analysis of the helium metering system by Banerjee (2006). The uncertainty of the fluid densities can now be extended to the uncertainty in the Atwood number

$$w_{A_t} = \left[\left(\frac{\partial A_t}{\partial \rho_1} w_{\rho_1}\right)^2 + \left(\frac{\partial A_t}{\partial \rho_2} w_{\rho_2}\right)^2\right]^{1/2} = \left[\left(\frac{2\rho_2}{(\rho_1 + \rho_2)^2} w_{\rho_1}\right)^2 + \left(\frac{-2\rho_1}{(\rho_1 + \rho_2)^2} w_{\rho_2}\right)^2\right]^{1/2} . \quad \text{(F.6)}$$

F.2 Uncertainty of measuring density using the cold-wire anemometer and temperature as a fluid marker

An uncertainty analysis for error propagation through the cold-wire measurement of fluid density can also be performed. Data reduction of the cold-wire voltage proceeds from the measured voltage (E) to fluid temperature (T_{mix}), fluid mass fraction ($f_{m,2}$), fluid volume fraction

($f_{v,2}$), and finally, fluid density (ρ). The progression of uncertainty through the data reduction will be described in the same order.

The cold-wire anemometer allows temperature to be measured via the anemometer voltage through a linear calibration of temperature versus voltage,

$$T_{mix} = A_{cw}(E) + B_{cw} \ . \tag{F.7}$$

Uncertainty in the measured temperature, $w_{T_{mixc}}$, by the cold-wire anemometer is determined through the uncertainty of the measured voltage and the uncertainty in the calibration of the cold-wire probe. According to Moffat (1988), these uncertainties can be combined in the same manner as which uncertainties have been combined in the standard Kline and McKlintock method,

$$w_{T_{mix}} = \left[\left(\frac{\partial T_{mix}}{\partial E} w_E \right)^2 + \left(w_{T_{calib}} \right)^2 \right]^{1/2} . \tag{F.8}$$

The measured temperature inside the mixing layer via the cold-wire, T_{mix}, combined with the measured free-stream temperatures, T_1 and T_2, are then used to determine the mass fraction of fluid 2,

$$f_{m,2} = \left[1 + \frac{c_{p,2}}{c_{p,1}} \frac{T_2 - T_{mix}}{T_{mix} - T_1} \right]^{-1} . \tag{F.9}$$

The uncertainty in the mass fraction due to the measurement of the fluid temperatures is then found as

$$w_{f_{m,2}} = \left[\left(\frac{\partial f_{m,2}}{\partial T_1} w_{T_1} \right)^2 + \left(\frac{\partial f_{m,2}}{\partial T_2} w_{T_2} \right)^2 + \left(\frac{\partial f_{m,2}}{\partial T_{mix}} w_{T_{mix}} \right)^2 \right]^{1/2} . \tag{F.10}$$

Using the fluid densities of streams 1 and 2, the mass fraction is converted to a volume fraction of fluid 2,

$$f_{v,2} = \frac{\rho_1}{(\rho_1 - \rho_2) + \frac{\rho_2}{f_{m,2}}} . \tag{F.11}$$

The uncertainty in the volume fraction can similarly be determined as

$$w_{f_{v,2}} = \left[\left(\frac{\partial f_{v,2}}{\partial \rho_1} w_{\rho_1} \right)^2 + \left(\frac{\partial f_{v,2}}{\partial \rho_2} w_{\rho_2} \right)^2 + \left(\frac{\partial f_{v,2}}{\partial f_{m,2}} w_{f_{m,2}} \right)^2 \right]^{1/2} . \tag{F.12}$$

Finally, the fluid density measured by the cold-wire is determined from the densities of stream 1 and 2 and the calculated fluid volume fractions such that,

$$\rho = f_{v,1}\ \rho_1 + f_{v,2}\ \rho_2 . \tag{F.13}$$

The uncertainty in the measured fluid density inside the mixing layer is then determined by

$$w_\rho = \left[\left(\frac{\partial \rho}{\partial \rho_1} w_{\rho_1} \right)^2 + \left(\frac{\partial \rho}{\partial \rho_2} w_{\rho_2} \right)^2 + \left(\frac{\partial \rho}{\partial f_{v,2}} w_{f_{v,2}} \right)^2 \right]^{1/2} , \tag{F.14}$$

yielding the uncertainty in the measurement of density by the cold-wire anemometer and the temperature marker.

F.3 Uncertainty of measuring velocity

A similar uncertainty analysis can be performed to estimate the uncertainty in measuring velocity through the S3WCA technique. Through this technique, hot-wire voltages are accurately converted to measurements of velocity by accounting for varying temperature and density within the mixing layer. The uncertainty analysis will show the propagation of the uncertainties in the measured fluid temperature and density through the data reduction for determining velocity.

Voltages measured by the hot-wire system, E_B, are initially corrected for temperature variations in the passing fluid through

$$E_{corr}^2(T_{ref}) = E_B^2(T)\left(\frac{T_{wire} - T_{ref}}{T_{wire} - T_{mix}}\right). \tag{F.15}$$

Therefore, the uncertainty in the corrected voltage due to the measured reference temperature for the hot-wire, T_{ref}, and the measured fluid temperature, T_{mix}, is

$$w_{E_{corr}} = \left[\left(\frac{\partial E_{corr}}{\partial T_{ref}} w_{T_{ref}}\right)^2 + \left(\frac{\partial E_{corr}}{\partial T_{mix}} w_{T_{mix}}\right)^2\right]^{1/2}. \tag{F.16}$$

Once the hot-wire voltages are corrected for variations in the fluid temperature, voltages are converted to effective velocities measured by the wire sensor. This is accomplished through the calibrated wire response due to velocity and concentrations of helium (fluid density). A series of simplifications and assumptions will be used to simplify the uncertainty analysis. For the purpose of this analysis, the mean velocity vector for the buoyancy-driven flow will be considered, $\langle U, V, W\rangle = \langle U_m, 0, 0\rangle$. Considering the statistical velocity vector for the flow under consideration allows for further simplification in the effective velocities of each wire sensor. In the situation of a one-dimensional velocity vector, the effective velocities of each sensor are approximately equal, $U_{eff,1} \cong U_{eff,2} \cong U_{eff,3}$. In addition, the response of each of the three wires are very similar such that the response from wire 1 will be used to approximate the behavior of all the hot-wires to both helium and velocity.

To account for the effects of helium and velocity on the hot-wire voltage response, the calibration data points are curve fit using a three-dimensional surface fit using *Table Curve 3D.* This allows the sensitivities of voltage to velocity and concentrations of helium to be directly evaluated. As previously mentioned, the fit which is utilized is of the form

$$U_{eff} = \left(\frac{a + c(f_{v,he}) + d(f_{v,he})^2 + e(f_{v,he})^3 - E_{corr}^2 - g(f_{v,he})E_{corr}^2 - h(f_{v,he})^2 E_{corr}^2 - i(f_{v,he})^3 E_{corr}^2}{fE_{corr}^2 - b} \right)^2 . \quad \text{(F.17)}$$

This allows the uncertainty in determining the effective velocities of the wire sensors to be calculated according to

$$w_{U_{eff}} = \left[\left(\frac{\partial U_{eff}}{\partial f_{v,he}} w_{f_{v,he}} \right)^2 + \left(\frac{\partial U_{eff}}{\partial E_{corr}^2} w_{E_{corr}^2} \right)^2 + (w_{U,calib})^2 \right]^{1/2} . \quad \text{(F.18)}$$

The final steps in the data reduction of hot-wire voltages to measurements of velocity converts the wire effective velocities, U_{eff}, to a global velocity component through the coordinate transformations described in Section 3. Therefore, the uncertainty in measuring the velocity in the global coordinate system is a function of the uncertainty of the wire effective velocity. The general documented uncertainty in measuring velocity via a three-wire probe due to its design and geometry can also be included in the uncertainty analysis as an additional uncertainty

$$w_U = \left[\left(\frac{\partial U}{\partial U_{eff}} w_{U_{eff}} \right)^2 + (w_{U_{error}})^2 \right]^{1/2} . \quad \text{(F.19)}$$

The uncertainty in measuring velocity due to the geometry of the probe is ~ 3% (Frota & Moffat 1983). Combining this uncertainty in the general three-wire hot-wire probe performance with the additional uncertainties associated with the introduced temperature and density variations leads to a final estimate of uncertainty of ~ 7% for $A_t = 0.03$ and ~ 13% for $A_t = 0.6$.

F.4 Uncertainty in turbulent statistics

The method of Kline and McClintock (1953) is ideal for determining the uncertainty in a single sample measurement from a variety of sources such as instrumentation and human error.

Statistic	Estimated Variance
$\sqrt{\overline{u^2}}$	$\dfrac{\left(\overline{u^4} - \left(\overline{u^2}\right)^2\right) / 4\overline{u^2}}{N}$
$\overline{u^2}$	$\dfrac{\overline{u^4} - \left(\overline{u^2}\right)^2}{N}$
$\overline{uv}$	$\dfrac{\overline{u^2 v^2} - \left(\overline{uv}\right)^2}{N}$

Table F.1. Example estimates of variance.

However, the method is not intended to be applied to multiple sample measurements of random processes, where higher order statistics are desired such as in fluid turbulence (Benedict & Gould 1996). Fortunately, the analysis of Benedict and Gould (1996) addresses this necessity for the measurement of uncertainty in higher order statistics as found in turbulence measurements. Benedict and Gould use general relationships for the sample variance of central moments obtained from the literature for a univariate (auto-correlation) or bivariate (cross-correlation) central moment. These relationships are derived for any distribution, without assuming a normal distribution. Not restricting the estimates of uncertainties to assumptions of normal distributions is important, since many aspects of turbulence are non-Gaussian. The general relationships for a sample variance of any central moment utilizes the measured sample to estimate the variance in a desired turbulent statistic. Examples of estimates in the variance of some common turbulent statistics are shown in Table F.1 where N is the number of independent samples. The calculated variance in the desired turbulent statistic is then used to determine the measurement uncertainty by defining the 5-95% confidence interval. Benedict and Gould applied these concepts to commonly measured turbulent statistics and confirmed uncertainty estimates with their own experimental turbulence measurements. Their methodology and statistical analysis will be used to estimate the uncertainty in all turbulent statistics presented in this dissertation.

F.5 Uncertainty in the growth parameter, α

Uncertainty in the measured growth parameter, α, is determined using the Kline and McKlintock method with individual parameter uncertainties estimated from previous estimates

through the Kline and McClintock and Benedict and Gould procedures. The growth parameter is found from the self-similar relationship of the growth of the mixing layer half width such that,

$$\alpha = \frac{v'_{rms}}{2A_t g \frac{x}{U}} \quad . \tag{F.20}$$

Therefore, the uncertainty is found through the sensitivities of the parameters used to calculate the growth parameter

$$w_\alpha = \left[\left(\frac{\partial \alpha}{\partial v'_{rms}} w_{v'_{rms}} \right)^2 + \left(\frac{\partial \alpha}{\partial A_t} w_{A_t} \right)^2 + \left(\frac{\partial \alpha}{\partial x} w_x \right)^2 + \left(\frac{\partial \alpha}{\partial U} w_U \right)^2 \right]^{1/2} . \tag{F.21}$$

F.6 Uncertainty in the molecular mixing parameter, θ

The uncertainty in determining the degree of molecular mixing, θ, is determined in a similar manner to the uncertainty of the measured growth parameter. The definition for molecular mixing is used to determine the uncertainty of the measurement,

$$\theta = 1 - \frac{\rho'^2}{(\rho_1 - \rho_2)^2 f_{v,1} f_{v,2}} \quad . \tag{F.22}$$

By combining the sensitivities of the parameters used to calculate molecular mixing, the uncertainty is

$$w_\theta = \left[\left(\frac{\partial \theta}{\partial \overline{\rho'^2}} w_{\overline{\rho'^2}} \right)^2 + \left(\frac{\partial \theta}{\partial f_{v,1}} w_{f_{v,1}} \right)^2 + \left(\frac{\partial \theta}{\partial f_{v,2}} w_{f_{v,2}} \right)^2 + \left(\frac{\partial \theta}{\partial \rho_1} w_{\rho_1} \right)^2 + \left(\frac{\partial \theta}{\partial \rho_2} w_{\rho_2} \right)^2 \right]^{1/2} . \tag{F.23}$$

F.7 Summary

Using the combined methodology of Kline and McClintock (1958) and Benedict and Gould (1996), the procedure for estimates of uncertainties in statistical measurements using the SW3CA technique has been described. A summary of the individual uncertainties using the outlined analysis is shown in Table F.2 and Table F.3. Uncertainties in the measured velocities and their variances are larger than those reported for the MPMO technique (~5%) used previously in the gas channel by Banerjee (2006). However, this is expected as the MPMO technique does not attempt to determine instantaneous measurements, but determines time-average statistics directly from time-averages of the hot-wire voltage fluctuations. The complexity and instantaneous nature of the S3WCA diagnostic results in larger measurement uncertainties, however, it is a more powerful measurement tool. The uncertainties of ~ 16% for the variance of measured velocity fluctuations however is reasonable for a hot-wire diagnostic (Bruun 1995), although not as accurate as the MPMO diagnostic. The primary sources of error in the measurements are in the determination of the sensed fluid density, large hot-wire sensitivities to helium, uncertainty in the inlet stream properties from the helium metering system, and the applied inlet stream temperature difference. Uncertainties in the measured statistics can be improved by using large sample sizes to include more independent measurements of the large-scale structures.

Parameter	% Uncertainty
A_t	9
U, V, W	7
T_{mix}	0.1
ρ_{mix}	5
$f_{v,1}$	2
$f_{v,he}$	4
$\overline{\rho'^2}$	12
θ	8
u'_{rms}	8
v'_{rms}	6
w'_{rms}	8
$\overline{u'^2}$	16
$\overline{v'^2}$	13
$\overline{w'^2}$	17
α	16
$\overline{\rho' u'}$	34
$\overline{\rho' v'}$	3
$\overline{\rho' w'}$	20

Table F.2. Estimated uncertainties for $A_t = 0.03$ measurements.

Parameter	% Uncertainty
A_t	2
U,V,W	13
T_{mix}	0.1
ρ_{mix}	2
$f_{v,1}$	2
$f_{v,\,he}$	3
$\overline{\rho'^2}$	21
θ	13
v'_{rms}	12
w'_{rms}	16
$\overline{v'^2}$	24
$\overline{w'^2}$	30
α	11
$\overline{\rho' v'}$	7
$\overline{\rho' w'}$	80

Table F.3. Estimated uncertainties for $A_t = 0.6$ measurement.

APPENDIX G

OPERATING PROCEDURES

Hot-wire anemometer calibration:

1) Connect the air-hose from the wall source, with the regulator at 80 psi, to the air calibration rotameter. Open the air ball valve at the wall.

2) Connect two helium bottles to the helium supply line which has an additional ball valve to isolate the two bottles from the remainder of the line (allows calibration to be performed with only 2 bottles present, rather than 7). Close the ball valve next to the connections for the 2 bottles.

3) Close the ball valve at the exit of the helium supply line to initially prevent pressurization of the helium rotameter.

4) Connect the helium-hose, with regulator set at 80 psi, from the helium supply line to the helium rotameter.

5) Re-check that all helium bottles are properly tightened and the exit valve is closed. Then slightly open one bottle of helium.

6) Open the exit valve (~ ¼ turn to keep the pressurized line from equilibrating). Reset the helium supply line pressure regulators to a final pressure of ~ 200 psi. Once pressures are set, fully open both bottles and the exit ball valve for the helium supply line.

7) Using the hot-wire traverse, raise the hot-wire probe to the center of the pipe for the calibration facility. Align the pitch, raw, roll (black mark on top of probe facing top center) of the probe with the downstream axis of the calibration facility. Once aligned gently slide the hot-wire probe and traverse approximately 2 cm inside the opening of the facility. Using a piece of cardboard rolled to fit around the end of the pipe, cover the top and sides of the pipe opening to protect the end conditions for the calibration facility. The bottom should remain uncovered to prevent gravity flows.

8) Turn on the data acquisition computer and start the *NI* software.

9) Place a handheld thermocouple in the exit flow of the calibration facility. Take a temperature reading from the handheld thermocouple and use the *Dantec MiniCTA* software to determine the appropriate hot-wire circuit board settings. Do not power the hot-wire anemometers yet. Adjust the hot-wire anemometer settings as needed by adjusting the pin settings in each hot-wire circuit.

10) Open the rotameters to a desired air measurement point. Power the hot-wire anemometers.

11) Check the anemometer voltage in the *NI* software and confirm successful connection and operation of the anemometers.

12) Begin taking data points. Use the rotameters to set calibration points and record the hot-wire voltages via the *NI* software for 15-20 seconds. While acquiring the voltage signals record by hand the fluid temperature with the handheld thermocouple. Export the acquired data to an ASCII file.

13) Repeat this process for all desired calibration points. For large Atwood number runs this is performed at concentration increments of 10% over a velocity range of ~ 0.6 m/s to 2.3 m/s. For low Atwood number runs it may be desirable to decrease the concentration increments to 5% or less and include fluid velocities as low as 0.3 m/s. A set of sample calibration points (mixture/velocity combinations) is found in a calibration spreadsheet.-

14) After calibration data has been collected, follow the instructions in the *Dantec MiniCTA* manual (examples contained text) to convert the calibration points to average voltages corrected for temperature variations. Also use the *Dantec* manual to convert the pipe velocities to the effective velocity sensed by each hot-wire sensor (this has already been done in the spreadsheet but you may use the Dantec manual or Bruun (1995) as a reference). The curves of E^2 vs. U_{eff} for each measured concentration and hot-wire sensor are the final product which will used in the analysis of hot-wire data.

Cold-wire anemometer operation (Also refer to AN-1005 operation manual – CD):

1. Set both toggles to “Test Mode” and “Adjust Mode”
2. Null the cable resistance.
    a. Connect the 4 m cable to the probe input and attach the shorting element to the end of the cable.
    b. Select the decade range for the resistance (probably 1x).
    c. Connect the anemometer output (from test output set) to the cold junction box.
    d. Dial the shorting resistance into the bridge resistance.
    e. Adjust the null screw to zero the voltage output from the anemometer by observing the output in the *NI* data acquisition software.
3. Disconnect the shorting element and connect the probe to the cable.
4. Dial the bridge resistance to balance the bridge. (Both arrows are dim)
5. Switch front toggle to “Normal”
6. Adjust damping to read 0 (or ~ +5 V for large Atwood number experiments)
7. To operate and calibrate:
    a. When in Test/Adjust mode switch the cold junction cable from the anemometer test output to the front output port.
    b. Switch both toggles to operate mode.
    c. Adjust the DC offset to the desired value (screw adjustment).

8. To calibrate:
    a. Record voltages from different temperature fluids.

b. Repeatedly check the bridge balance as this may change as the anemometer circuit heats up.
c. If necessary, direct a fan across the circuit to allow the circuit to reach an equilibrium temperature.
d. If the bridge resistance needs re-balancing change the balance and take a new set of data. The intercept for the calibration will change but the slope (resistance) of the probe's calibration should be constant as long as the bridge is balanced.

Setup for the gas channel:

1) Determine the necessary helium lines for the desired experiment based on the Atwood number and channel velocity (*MATLAB* file GC_Param.m). For estimating the quantity of useful helium in each bottle, using 1.75 lb/bottle is an adequate estimate.

2) Place the selected orifices in each helium line in the fitting located between the exit ball valve and the PVC pipe.

3) Close the exit ball valve.

4) Connect all bottles to the appropriate helium line connection. Be sure to tighten appropriately.

5) Once all bottles are connected and tightened, slightly open 1 bottle to pressurize the helium supply line and check for any leaks in the connections. If a leak is found, close the opened bottle and vent the helium from the line to depressurize it before tightening any loose connections.

6) While the helium line is pressurized, slightly open the exit ball valve to prevent the helium supply line from equalizing in pressure. During this time check the pressures of each pressure regulator. The first upstream regulator should be set to 1050 psi and the second regulator should be set to 550 psi.

7) Now that the helium supply line has been checked for leaks and the pressure regulators have been set, close all helium bottles and slowly vent the helium line.

8) Set the channel velocities for the top and bottom streams for the desired experiment: Using the fog generator, fill a baster with fog and inject it into the top or bottom stream. Time the movement of the fog between marked locations in the channel using digital video. Use the frames of the recorded video to obtain accurate velocities for the top and bottom streams. (Remember the bottom stream should be set to a smaller velocity than the top, representing only the air-component of that helium/air stream)

9) Use the video to check the air velocities, and adjust the blower dampers as needed to correctly set the desired velocities.

10) Place the hot-wire traverse (probes not attached) inside the channel at the desired measurement location. If possible, maintain all anemometer cable connections from the

calibration to placement inside the channel. Align the probe body inside the channel as done previously for calibration. The probe body should be aligned with the downstream axis of the channel.

11) Carefully place the three-wire hot-wire probe on the probe body and also attach the cold-wire to the three-wire probe body. This is done by creating an adequate separation between the two probe bodies using electrical tape. The two probe bodies must not come in direct contact as they are both connected to their respective grounds. Once the separation is set, use a clothes pin to secure the cold-wire probe to the hot-wire probe body. Gently slide the cold-wire into place beside the three-wire probe, until they are located in approximately the same measurement location.

Running a large Atwood number experiment:

1) Turn on the data acquisition computer and cold-wire anemometer 20-30 minutes before the experiment.

2) Take reference voltages with the hot-wire anemometer, cold-wire anemometer , and the thermocouples with the *NI* software in the air streams using the air blowers to circulate the air (can be done in top and bottom stream with the traverse).

3) Turn off the hot-wire anemometers and the air blowers.

4) Lower the exit flap inside the gas channel exit to full closed.

5) Place covers over the top and bottom exit of the channel to approximately seal the exit flows.

6) Place a flexible duct hose inside the channel from the damper for the exit exhaust fan to a position further upstream inside the test section.

7) Mark the damper setting for the bottom stream blower. Once the position is marked, fully close the damper on the bottom stream blower.

8) Open 1 helium bottle on the helium line containing 8 bottles. Slowly vent the bottle into the channel filling it over several minutes.

9) At the same time, turn the exit exhaust fan on low to slowly draw out the heavy air inside the channel while helium is allowed into the channel.

10) Once the bottle has mostly vented into the channel, close the helium bottle, remove the flexible duct inside the channel, and turn off the exit exhaust fan.

11) Re-open the bottom air stream damper to full open to initially thin the helium/air mixture as the experiment starts. Reset the exit flap inside the channel to the desired position (generally this is 1/3 closed for most experiments).

12) Turn on the hot-wire anemometers. Check that the resistance of the cold-wire anemometer is balanced (Refer to *AA Labs* documentation). Update the macro provided by *NI* for using hardware gains with the thermocouples (the selected gain should be 800 for both thermocouple channels).

13) Check that all exit ball valves for the 3 helium lines are closed.

14) Open all helium bottles and pressurize the helium supply lines.

15) The experiment is now ready to be started. Two persons are necessary to run the experiment past this point.

16) One person remains at the front of the channel. The second person waits with a stop watch at the helium supply lines.

17) Partially open each helium supply line, start the stop watch, and turn on the exit exhaust fan on high.

18) Simultaneously the person at the front of the channel should remove the cover from the bottom exit and then plug-in the bottom air stream blower. The person in front should then immediately uncover the top stream exit and start the top stream blower.

19) By this time ~ 20 seconds should have gone by and all exits should be full open and both air blowers should be turned on. While watching the stop watch, the person at the helium supply lines should incrementally open the helium supply line valves every 10 seconds.

20) The helium supply lines should be full open at ~ 50-60 s. The person in the front of the channel should now slowly reduce the bottom stream air blower by closing the damper to its marked position. The fog generator can be used to monitor the initial start of the experiment to ensure the experiment is started properly and there is no large shear between the two streams. However, once data acquisition begins the fog generator should be turned off.

21) At this point the pressure regulators should be monitored by one person until the end of the experiment. Once the final pressure regulators begin to drop, pressure is no longer constant at the orifice and the experiment is over.

22) Data acquisition should follow ~ 10-15 seconds after the bottom stream velocity is set. This should occur at the 1 min 15 – 1 min 30 point in the experiment. The kerosene heater may also be turned on, heating the bottom air stream to counteract the cooling effects of the expanding helium. It is better to obtain the trace as early as possible while the temperature difference between the two streams is manageable.

23) Once the pressure regulators are no longer maintaining a constant pressure, close the helium supply lines and close all helium bottles.

24) Additional reference points for the anemometers and thermocouples may be taken in air.

25) Export the captured data from the *NI* software and turn off all electronics.

26) Vent the helium supply lines of their remaining pressure.

27) Once the helium supply lines have been vented and all bottles are tightly closed, disconnect each bottle from the flexible hose connections and re-cap.

APPENDIX H

TABLES OF EXPERIMENTAL DATA

Contained here are additional tables summarizing many of the experimental results from this investigation. Specifically included are tables summarizing data obtained using the S3WCA diagnostic in the gas channel, which supplement tables already included in the main text. Table H.1 and H.2 contain turbulent statistics determined at $A_t = 0.03$ and $A_t = 0.6$ at the centerline of the mixing layer. In addition, Table H.3 includes details of conditional statistics for a two-fluid approximation, which were not included in Section 6. A listing of the data files which contain the data points for figures contained in the results sections of the dissertation is shown in Table H.4.

A_t	0.03	0.03	0.03	0.03
X	1.0	1.25	1.5	1.75
τ	0.76	0.95	1.14	1.33
U_m	0.65	0.65	0.65	0.65
$f_{v,1}$	0.50	0.49	0.47	0.51
$\Delta\rho$	0.075	0.075	0.074	0.074
ρ'_{rms}	0.023	0.022	0.021	0.020
θ	0.62	0.66	0.68	0.70
u'_{rms}	0.057	0.059	0.064	0.070
v'_{rms}	0.073	0.078	0.089	0.102
w'_{rms}	0.041	0.048	0.055	0.059
$\overline{u'v'}$	0.0013	0.0006	0.0013	0.0015
$\overline{u'w'}$	0.0005	-0.00002	0.0010	0.0011
$\overline{v'w'}$	-0.0008	-0.0011	-0.0008	-0.0005
R^2_{uv}	0.10	0.02	0.05	0.04
R^2_{uw}	0.04	0.0001	0.08	0.06
R^2_{vw}	0.08	0.08	0.03	0.01
α	0.080	0.069	0.066	0.064
$\overline{\rho'u'}$	-0.0002	-0.00004	-0.0002	-0.0002
$\overline{\rho'v'}$	-0.0013	-0.0014	-0.0014	-0.0016
$\overline{\rho'w'}$	0.0004	0.0003	0.0003	0.0002
$\overline{\rho'u'}/(\Delta\rho A_t gx/U)$	-0.0048	-0.0009	-0.0031	-0.0031
$\overline{\rho'v'}/(\Delta\rho A_t gx/U)$	-0.037	-0.033	-0.028	-0.026
$\overline{\rho'w'}/(\Delta\rho A_t gx/U)$	0.0105	0.0075	0.0069	0.0042
$R_{\rho'v'}$	-0.76	-0.81	-0.74	-0.75
$R_{\rho'u'}$	-0.12	-0.03	-0.12	-0.14
$R_{\rho'w'}$	0.38	0.31	0.30	0.21
K_u	2.98	3.02	3.34	2.92
K_v	2.27	2.16	2.34	2.17
K_w	2.82	2.96	3.20	2.97
v'_{rms}/w'_{rms}	1.8	1.6	1.6	1.7
v'_{rms}/u'_{rms}	1.3	1.3	1.4	1.5
u'_{rms}/w'_{rms}	1.4	1.2	1.2	1.2

Table H.1. A_t = 0.03 centerline S3WCA measurements (units in kg, m, and s).

A_t	0.6	0.6	0.6
X	0.40	0.60	0.70
τ	0.44	0.66	0.78
U_m	2.0	2.0	2.0
$f_{v,1}$	0.54	0.46	0.50
$\Delta\rho$	0.880	0.870	0.870
ρ'_{rms}	0.270	0.250	0.240
$\overline{\rho}$	0.800	0.680	0.770
ρ_1	1.190	1.180	1.200
ρ_2	0.320	0.310	0.320
θ	0.54	0.46	0.60
v'_{rms}	0.36	0.39	0.44
w'_{rms}	0.25	0.26	0.30
$\overline{v'w'}$	-0.0130	-0.0260	0.0030
R^2_{vw}	-0.14	-0.25	0.02
$v'/2A_t g(x/U)$	0.15	0.11	0.10
$\overline{\rho'v'}$	-0.0540	-0.0710	-0.0600
$\overline{\rho'w'}$	-0.0030	0.0100	-0.0090
$\overline{\rho'v'}/(\Delta\rho A_t gx/U)$	-0.052	-0.046	-0.033
$\overline{\rho'w'}/(\Delta\rho A_t gx/U)$	-0.003	0.007	-0.006
$R_{\rho'v'}$	-0.58	-0.68	-0.54
$R_{\rho'w'}$	-0.04	0.13	-0.18
K_v	3.24	3.14	3.62
K_w	5.02	4.39	5.17
v'_{rms}/U	0.18	0.20	0.22
v'_{rms}/w'_{rms}	1.4	1.5	1.5

Table H.2. A_t = 0.6 centerline S3WCA measurements (units in kg, m, and s).

A_t	0.03	0.03	0.03	0.03
X	1.0	1.25	1.5	1.75
τ	0.76	0.95	1.14	1.33
U_m	0.65	0.65	0.65	0.65
$f_{v,1}$	0.50	0.48	0.47	0.49
$\overline{\rho}$	1.14	1.14	1.13	1.14
ρ_1	1.17	1.17	1.17	1.17
ρ_2	1.10	1.10	1.10	1.10
v_1	-0.048	-0.056	-0.059	-0.065
v_2	0.049	0.053	0.053	0.063
a_0	-0.0011	-0.0012	-0.0012	-0.0014
a_2	-0.0015	-0.0017	-0.0017	-0.0021
κ	0.27	0.29	0.29	0.33

Table H.3. A_t = 0.03 conditional statistics for a two-fluid approximation (units in kg, m, and s).

FIGURE	DATA FILE
4.1	Figure_4_1_MP.txt, Figure_4_1_MPMO.txt, Figure 4_1_PIV, Figure_4_1_S3WCA.txt
4.2	Figure_4_2.txt
4.3	Figure_4_3.txt
4.4	Figure_4_4_TCRamaprabhu.txt, Figure_4_4_TCMueschke.txt, Figure_4_4_MPMO.txt, Figure_4_4_S3WCA.txt
4.5	Figure_4_5.txt
4.6	Figure_4_6a_MPMO.txt, Figure_4_6a_S3WCA.txt, Figure_4_6b_MPMO.txt, Figure_4_6b_S3WCA.txt
4.7	Figure_4_7.txt
4.8	Figure_4_8.txt
4.9	Figure_4_9.txt
4.10	Figure_4_10.txt
4.11	Figure_4_11_density.txt, Figure_4_11_rhov.txt, Figure_4_11_verticalvel.txt
5.2 (a)	Figure_5_2.txt
5.3 (b)	Figure_5_3_GC.txt, Figure_5_3_LEM.txt
5.4	Figure_5_4_MP.txt, Figure_5_4_MPMO.txt, Figure_5_4_PIV.txt, Figure_5_4_S3WCA_smallA.txt, Figure_5_4_S3WCA_largeA.txt
5.5	Figure_5_5_MPMO.txt, Figure_5_5_S3WCA_smallA.txt, Figure_5_5_S3WCA_largeA.txt
5.6	Figure_5_6_MPMO.txt, Figure_5_6_S3WCA_largeA.txt, Figure_5_6_S3WCA_smallA.txt, Figure_5_6_TCMueschke.txt, Figure_5_6_TCRamaprabhu.txt
5.7	Figure_5_7_density_pdf.txt, Figure_5_7_velocity_pdf.txt
5.8	Figure_5_8.txt
5.9	Figure_5_9.txt
6.1	Figure_6_1_f1.txt, Figure_6_1_f2.txt
6.2	Figure_6_2_f1.txt, Figure_6_1_f2.txt
6.3	Figure_6_3_f1.txt, Figure_6_3_f2.txt
6.4	Figure_6_4_f1.txt, Figure_6_4_f2.txt
6.5	Figure_6_5_Re.txt, Figure_6_5_tau.txt

Table H.4. Index of data files for each figure.

VITA

Name:	Wayne Neal Kraft
Address:	c/o Professor Malcolm Andrews Department of Mechanical Engineering Texas A&M University College Station, TX 77843-3123
Education:	B.S., Mechanical Engineering, Texas A&M University, 2001 M.S., Mechanical Engineering, Texas A&M University, 2004 Ph.D., Mechanical Engineering, Texas A&M University, 2008